Strongly interacting photons via Rydberg-Rydberg interactions

by

Qiyu Liang

Submitted to the Department of Physics
in partial fulfillment of the requirements for the degree of

Doctor of Philosophy

at the

MASSACHUSETTS INSTITUTE OF TECHNOLOGY

September 2017

Signature redacted

Author .....

Department of Physics
June 22, 2017

Signature redacted

Certified by .....

Vladan Vuletić
Lester Wolfe Professor of Physics
Thesis Supervisor

Signature redacted

Accepted by .....

Nergis Mavalvala
Associate Department Head of Physics

Strongly interacting photons via Rydberg-Rydberg interactions

by

Qiyu Liang

Submitted to the Department of Physics
on June 22, 2017, in partial fulfillment of the
requirements for the degree of
Doctor of Philosophy

Abstract

A quantum nonlinear optical medium, i.e. a medium where the light propagation depends on photon number, has been a long-standing goal due to its applications in quantum information, communication and metrology. When the medium is nonlinear at single photon level, it can be viewed as strong interactions between individual photons mediated by the medium. Here, we achieve such strong interactions by coupling the photons to highly polarizable Rydberg states with a phenomena called electromagnetically induced transparency (EIT). The strong van der Waals or dipole-dipole interactions between Rydberg excitations map to the photons under EIT conditions.

The photons are incident on a cigar-shaped laser-cooled rubidium cloud in free space. After the photons emerge out of the cloud, we measure the photon correlations from time-resolved single photon detections, which reveal crucial information about the quantum states of strongly interacting two or three photons.

In this thesis, I will present four experiments. The first two experiments demonstrate quantum nonlinearities with a propagating continuous wave (cw) light field via Rydberg-Rydberg interactions in the dissipative and dispersive regimes, respectively. In the dissipative regime, strong photon anti-bunching is observed. In the dispersive regime, we achieve a conditional phase shift $\sim \pi/4$, together with photon-bunching driven by attractive force. Moreover, the photons acquire a finite mass and we see evidence for a diphoton molecule. In the third experiment, by measuring higher-order correlation functions, we observe a three-photon bound state evidenced by tighter binding in addition to a larger conditional phase shift than the two-photon states. By comparing with an effective field theory, our results suggest that there might be a three-photon force on top of the pairwise interactions owing to the saturation of the interaction. Namely, only one Rydberg excitation can be created within a characteristic length scale called blockade radius. Finally, we explore the exchange interaction instead of the widely studied blockade shifts. Under the exchange interactions, a propagating photon and a stored one experience coherent collisions protected by a symmetry of the Hamiltonian and pick up a robust $\pi/2$ phase shift.

Thesis Supervisor: Vladan Vuletić
Title: Lester Wolfe Professor of Physics

Acknowledgments

My first thanks go to my parents, Yuekun Liang and Yufeng Chen, who have always been an inspiration to me. Despite not working in academia, the wild ideas and the scientific approaches for discovery have merged into their life. I have been so used to walking around scattered electronic components, soldering irons, half-finished circuits, etc. They set a role model for me to seek out what I really want to do and be passionate about life.

In spirit of hunting for true fascinations, I came to know atomic molecular and optical (AMO) physics after I was enrolled in Department of Nuclear Science & Engineering (NSE) at MIT. I knocked on the door of Vladan Vuletić's office. Vladan surprised me by giving a chance to an unprepared outsider when his labs were loaded with brilliant students. Throughout my graduate study, he always believes in me and always sees the positive side. He gives us all the freedom to try our stupid ideas and to work with whatever schedule we feel comfortable. On the other hand, he helps us a great deal in technical details as well as scientific issues. We collaborate with Mikhail Lukin closely. By connecting us to theorists, he always pushes forward projects when they seem to be stuck. Miraculously, he remembers data we showed him and ideas discussed years ago, and brings them up in key moments, when no one else can recall anything.

I was extremely fortunate to work closely with Cheng Chin for a summer. I learned so much from his hands-on approach that I can never thank him enough. Additionally, he helps me tremendously in person, showing me how to be a better scientist, advising me for my career in academia and telling me where to find better food.

Thibault Peyronel and Sebastian Hofferberth (first postdoc I work with) are my tutors from day one. Thibault sets an example for me as a leader in the lab. I will never forget his patience, dedication and "get-everything-done" efficiency. I got invaluable advice, and borrowed countless parts and equipment, from Marko Cetina, Haruka Tanji-Suzuki and Wenlan Chen while building the transfer cavity system. Ofer

Firstenberg (second postdoc) introduced me to the center stage of the experiments, from data analysis to the related theories. He is such a fun person to work with. His "Pinky and the Brain" poster is still outside our lab, receiving a great amount of attention and praise from people passing by. Jeff Thompson (third postdoc) is a remarkable person, being so smart, so diligent and so kind. He inspired me in many different aspects. For example, he came up with his own project and defended it at the time when it did not look like a good idea. The new generation in the lab are Sergio Cantu, Aditya Venkatramani and Travis Nicholson. Sergio has never stopped being enthusiastic, Aditya is our in-house theorist, and Travis is a technologically gifted and knowledgeable postdoc. Led by Travis, the team is upgrading the lab, and I am looking forward to their upcoming productive years.

I'd like to acknowledge two visiting students I tutored as well, Elie Gouzien and Elena Yakshina. I learned and enjoyed a lot from working with them. I also owe special thanks to Boris Braverman, Molu Shi, Dorian Gangloff, Alexei Bylinskii and Akio Kawasaki, with whom I prepared my qualifying exam, and/or went through my conference and interview talks. Besides, Center for Ultracold Atoms (CUA) is a very supportive, dynamical community. I am grateful for all the principle investigators, students, postdoctoral scholars, visiting scientists and administrative staff.

I'd like to thank the post-collegiate track and field community around New England area. During the last half of my doctoral studies, I gradually became aware of the opportunities, to get back to my hobby, dating back to high school. I sacrificed it for physics, but now they live together, due to the help from friends and even strangers. It all started with Betty Lou McClanahan, who told me there are clubs I could join. Then, I found Greater Boston Track Club, where I was coached by Dave Callum for a year, during which I slowly got back to competition. Later, a personal trainer, David Bond, introduced me to the sprint coach at MIT, Peter McNaughton, who have been coaching me ever since. Under his guidance, I have been steadily improving, picking up new events and having so much fun.

Last, many thanks go to my long-time friend Liangfang Zhao, who has always been around for the past fifteen years.

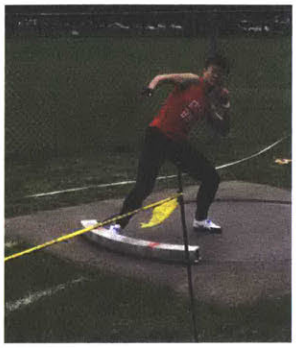

(a)

(b)

(c)

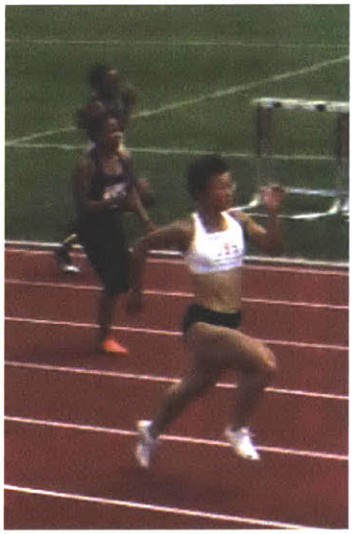

(d)

(e)

(f)

(g)

Figure 0-1: Competition photos

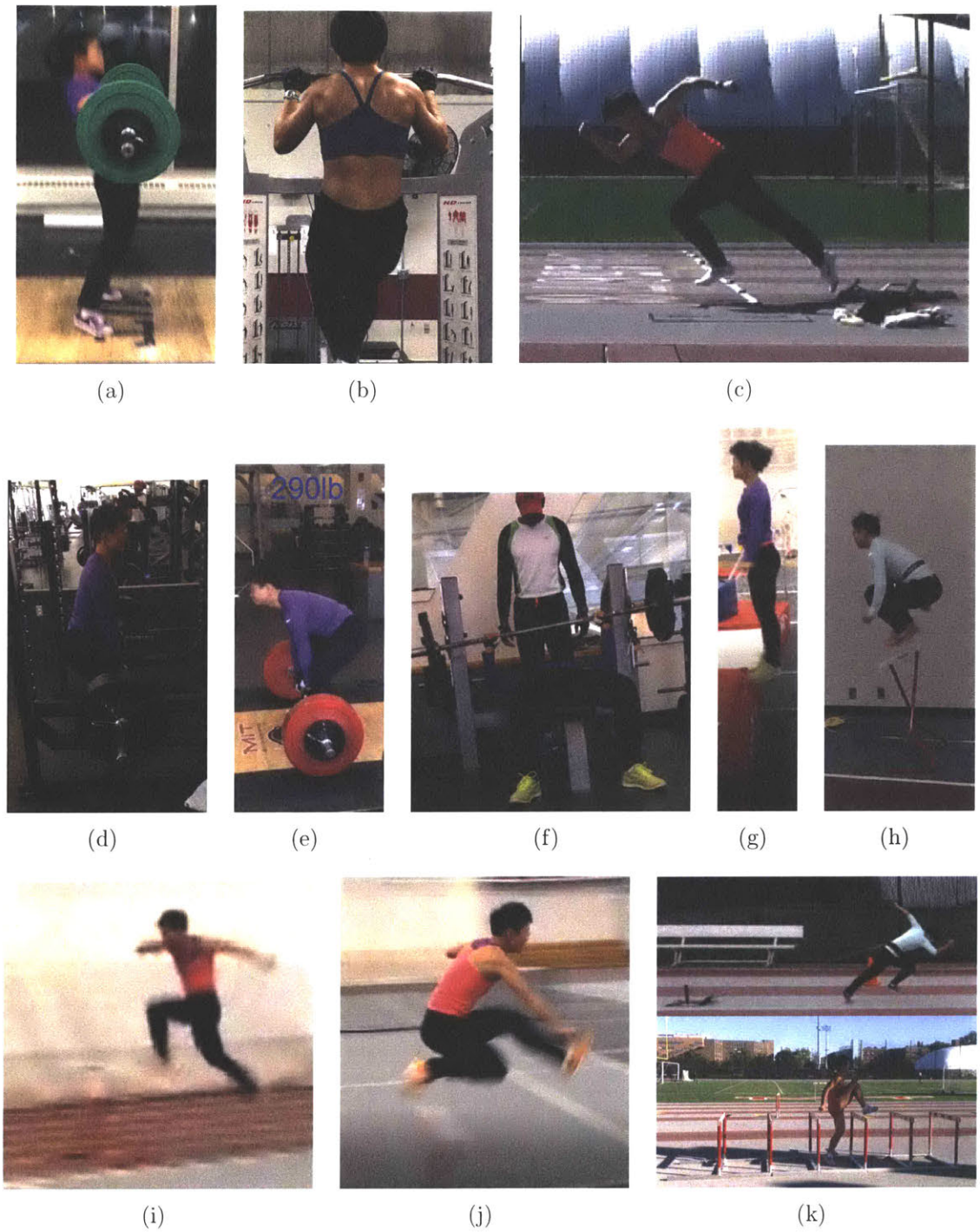

(a) (b) (c)

(d) (e) (f) (g) (h)

(i) (j) (k)

Figure 0-2: Training photos

Citations to Previously Published Work

The work in Chapter 6 is documented in the following three publications:

> "Quantum nonlinear optics with single photons enabled by strongly interacting atoms", T. Peyronel, O. Firstenberg, Q.-Y. Liang, S. Hofferberth, A. V. Gorshkov, T. Pohl, M. D. Lukin & V. Vuletić, *Nature* **488**, 57 (2012)
>
> "Attractive photons in a quantum nonlinear medium", O. Firstenberg, T. Peyronel, Q.-Y. Liang, A. V. Gorshkov, M. D. Lukin & V. Vuletić, *Nature* **502**, 71 (2013)
>
> "Quantum nonlinear optics using cold atomic ensembles", Thibault Peyronel, PhD diss., Massachusetts Institute of Technology, 2013.

The work in Chapter 8 is documented in the following publication:

> "Symmetry-protected collisions between strongly interacting photons", J. D. Thompson, T. L. Nicholson, Q.-Y. Liang, S. H. Cantu, A. V. Venkatramani, S. Choi, I. A. Fedorov, D. Viscor, T, Pohl, M. D. Lukin & V. Vuletić, *Nature* **542**, 206 (2017)

The effective field theory in Chapter 7 is based on the following publication:

> "Effective field theory for Rydberg polaritons", M.J. Gullans, J.D. Thompson, Y. Wang, Q.-Y. Liang, V. Vuletić, M.D. Lukin & A.V. Gorshkov, *Phys. Rev. Lett.* **117**, 113601 (2016)

Contents

List of Figures

List of Tables

Chapter 1

From classical nonlinearities to strongly interacting photons

In free space, Gauss's law is

$$\nabla \cdot (\epsilon \vec{E}) = \rho_f \tag{1.1}$$

where $\vec{E}$ and ρ_f are the electric field and free charge density, respectively.

In a medium, the role of electric field is replaced by the displacement field $\vec{D}$ to account for the response of the medium while keeping the free charge the only source term.

$$\nabla \cdot \vec{D} = \rho_f \tag{1.2}$$

where $\vec{D} = \epsilon_0(1+\chi)\vec{E}$, with χ being the susceptibility. If the medium is nonlinear, then χ depends on the electric field. We can expand χ as follows:

$$\chi = \chi^{(1)} + \chi^{(2)}E + \chi^{(3)}E^2 + \cdots \tag{1.3}$$

From Eq. 1.3, we can see that the propagation of a electromagnetic wave in a nonlinear medium depends on itself and other waves that travel in the medium simultaneously. Allowing χ to be complex will account for both the phase shift ($Re[\chi]$) and the absorption ($Im[\chi]$). We can then interpret the nonlinear phase shift or absorption as interactions between the photons mediated by the medium.

In conventional nonlinear mediums, such interactions are so weak that a classical description involving the fields and intensities are sufficient. Such conventional nonlinear mediums have been studied for decades, particularly in the context of nonlinear optical fibers [1].

The quest of stronger nonlinearities are driven by quantum information and communication [2, 3], as well as other applications of non-classical states of light such as quantum metrology [4]. How strong is strong? The interactions from individual photons are significant–one has to count the photons one by one.

Realizing such quantum nonlinearities is challenging. The challenge can be qualitatively understood as follows: Imagine a light beam is incident on a single atom. For simplicity, let's model the atom as a two-level system with a stable ground state g and an excited state e. The $g \rightarrow e$ transition has a wavelength λ. Suppose the atom is initially in its ground state g. The medium (or the atom) is absorptive to the first incident photon, because the photon will be absorbed, and consequently, the atom will go to the excited state e. At that moment, the medium is transparent to the second photon, since the atom cannot absorb another photon before it decays back to g. We therefore say the two photons have strong dissipative interactions, due to the strong modification of the attenuation of the second photon caused by the first photon. Next, let's estimate how likely such interaction will take place. The size (cross section) of the atom is $\sigma_a \leq \frac{3\lambda^2}{2\pi}$, while the size of a diffraction-limited Gaussian beam is $\sigma_{ph} = \pi w^2 \geq \lambda^2$, where w denotes the $\frac{1}{e^2}$ beam waist. Therefore, the probability of a single photon in the beam interacting with the atom $P_{int} = \sigma_a/\sigma_{ph}$, smaller than unity, even under the optimum conditions. Such interaction between a single atom and a single photon has been observed [5, 6], with probabilities of a few percent.

One way to boost this probability is to put the photons in a box (optical cavity), and thus the probability is increased by the number of times the photon passes the atom (or rather, the number of round trips inside the cavity). Massive progress has been made in recent years [7–10], especially with nanofabrication. Proposals have been put forward to study Mott-superfluid transition [11] and fractional quantum hall states [12] using coupled cavity arrays.

However, in order for two photons to interact by saturating a single atom, they have to see the atom more or less at the same time. Moreover, Shapiro's no-go theorem [13] precludes the interactions caused by Kerr nonlinearity from a high-fidelity phase modulation. In order to get around these limitations, one can take advantage of a phenomena called electromagnetically induced transparency (EIT) with an ensemble of atoms [14, 15]. Under EIT conditions, the light can be slowed or even stopped–stored as a spin wave. The no-go theorem does not apply to the scenario of a propagating photon interacting with a stored one.

An alternative approach to realize quantum nonlinearities is to couple the photons to strongly interacting Rydberg atoms. Due to the large separation of the ionic core and the outermost electron, the (induced) dipole moments are very large. Consequently, the van der Waals or dipole-dipole interactions are huge. Those interactions can be mapped to photonic interactions with EIT. This is a rapidly developing field, with strong interactions between individual photons realized within the past five years [16–23]. Despite both being successful approaches, there are several distinct differences between coupling to a cavity and to a strongly interacting atomic state to enhance the photon-photon interaction. First, the Rydberg interactions are long-range in nature, in contrast to the zero range Kerr nonlinearity. Second, a (finite) effective mass emerges with Rydberg EIT. This quadratic term in the dispersion relation escapes the no-go theorem naturally. Third, the propagation of a wavepacket inside a medium with Rydberg EIT inevitably involves continuous spatial modes, while the simplest description of cavity QED only considers a single mode. These distinctions open up exciting possibilities. For example, the quantum version of solitons–shape-preseving pulses owing to the cancellation of the group-velocity dispersion and the nonlinear interaction–arise in our Rydberg EIT system. Such quantum solitons have been predicted decades ago [24–26], but have never been observed.

The put our discussion into a broader perspective, the emitter (atom) can be replaced by molecules [27] and artificial atoms in solid-state systems such as colored centers in diamond [28] and quantum dots [29]. Furthermore, instead of optical photons, quantum nonlinearity with microwave photons [30] is another fascinating field,

usually involving different experimental techniques, opportunities and challenges.

This thesis is structured as follows: First, I will explain in more detail about Rydberg atoms and EIT, which are the two key ingredients in our realization of quantum nonlinearities. Next, I will introduce the experimental setup used in all four experiments. Then, I will present the experiments, starting from the first demonstrations of nonlinear interactions mediated by highly polarizable Rydberg atoms in both the dissipative and dispersive regimes. We are among the first three groups [16–18] realizing quantum nonliearities with this new approach. In the dispersive regime, we achieve a conditional phase shift $\sim \pi/4$–a then free space record to my best knowledge. Meanwhile, we observe photon-bunching as an indication of a diphoton molecule. The initial observation of the two-photon bound state inspires us to seek for trimers by measuring higher-order correlation functions. These correlation measurements reveal evidence of the three-photon bound state through tighter binding and an additional phase shift. Finally, we explore the exchange interaction instead of the widely studied blockade shifts. Under such exchange interactions, when a propagating photon collides with a stored photon, they pick up a robust $\pi/2$ phase shift insensitive to the detailed experimental parameters, thanks to a symmetry of the interaction Hamiltonian.

Chapter 2

The intensity correlation function

The second-order coherence, or the intensity correlation function, $g^{(2)}$, has proven to be an incredibly powerful tool for characterizing the quantum states of light. In this chapter, I will give an overview of its application in both single- and multi-mode quantum optics, as well as the generalization to the third-order. Most contents in this chapter can be found in [31].

2.1 General formalism

The electric field operator can be generally written as

$$\hat{\vec{E}}_T(\vec{r},t) = \hat{\vec{E}}_T^+(\vec{r},t) + \hat{\vec{E}}_T^-(\vec{r},t) \tag{2.1}$$

where

$$\begin{aligned}\hat{\vec{E}}_T^+(\vec{r},t) &= \sum_{\vec{k}}\sum_{\lambda} \vec{e}_{\vec{k}\lambda}(\hbar\omega_k/2\epsilon_0 V)^{1/2}\hat{a}_{\vec{k}\lambda}\exp[-i\chi_{\vec{k}}(\vec{r},t)] \\ \hat{\vec{E}}_T^-(\vec{r},t) &= \sum_{\vec{k}}\sum_{\lambda} \vec{e}_{\vec{k}\lambda}(\hbar\omega_k/2\epsilon_0 V)^{1/2}\hat{a}^\dagger_{\vec{k}\lambda}\exp[i\chi_{\vec{k}}(\vec{r},t)]\end{aligned} \tag{2.2}$$

The subscripts $\vec{k}$ and λ denote the wavevector and the polarization of each mode, respectively. The subscript T refers to transverse–the field that is transverse to the

light propagation direction. The phase angle $\chi_{\vec{k}}(\vec{r},t) = \omega_k t - \vec{k}\cdot\vec{r} - \pi/2$. ω_k is the angular frequency of the mode. V is the volume of the region where the electromagnetic field is quantized. $\vec{e}_{\vec{k}\lambda}$ is a unit vector denoting the polarization of the mode $\vec{k}\lambda$.

The photon number operator is

$$\hat{n}_{\vec{k}\lambda} = \hat{a}^{\dagger}_{\vec{k}\lambda}\hat{a}_{\vec{k}\lambda} \tag{2.3}$$

The intensity correlation function $g^{(2)}$ measures the correlation of the light field at two space-time points.

$$g^{(2)}(\vec{r}_1,t_1;\vec{r}_2,t_2) = \frac{\langle \hat{E}_T^-(\vec{r}_1,t_1)\hat{E}_T^-(\vec{r}_2,t_2)\hat{E}_T^+(\vec{r}_2,t_2)\hat{E}_T^+(\vec{r}_1,t_1)\rangle}{\langle \hat{E}_T^+(\vec{r}_1,t_1)\hat{E}_T^-(\vec{r}_1,t_1)\rangle\langle \hat{E}_T^-(\vec{r}_2,t_2)\hat{E}_T^+(\vec{r}_2,t_2)\rangle} \tag{2.4}$$

2.2 Classical limits

For simplicity, we can reduce the problem to one-dimensional, replacing $\vec{r}_i$, $i = 1,2$ to z_i. Then $g^{(2)}(\vec{r}_1,t_1;\vec{r}_2,t_2) = g^{(2)}(z_1,t_1;z_2,t_2) = g^{(2)}(\tau)$, where $\tau = t_2 - t_1 - \frac{z_2-z_1}{c}$.

For classical light fields, the operators in the numerator can be exchanged and the fields can be expressed as intensities

$$g^{(2)}(\tau) = \frac{\langle I(t_1)I(t_1+\tau)\rangle}{\langle I(t_1)\rangle\langle I(t_1+\tau)\rangle} \tag{2.5}$$

Applying

$$2I(t_1)I(t_2) \le I(t_1)^2 + I(t_2)^2 \tag{2.6}$$

to the cross terms, it is obvious that

$$[\frac{I(t_1)+I(t_2)+\cdots+I(t_N)}{N}]^2 \le \frac{I(t_1)^2+I(t_2)^2+\cdots I(t_N)^2}{N} \tag{2.7}$$

Imagine $I(t_i)$, $i = 1, 2, \cdots, N$ is the result of the ith measurement of the intensity.

Then

$$g^{(2)}(\tau = 0) = \frac{\langle I^2 \rangle}{\langle I \rangle \langle I \rangle} \geq 1 \tag{2.8}$$

This is the lower limit of $g^{(2)}(0)$ of classical fields. This result cannot be extended to $\tau \neq 0$.

There is another important inequality derived from Eq. 2.6

$$[I(t_1)I(t_1+\tau)+\cdots+I(t_N)I(t_N+\tau)]^2 \leq [I(t_1)^2+\cdots+I(t_N)^2][I(t_1+\tau)^2+\cdots+I(t_N+\tau)^2] \tag{2.9}$$

The two summations on the right are equal for a sufficiently long and numerous series of measurements, and the square root of Eq. 2.9 produces

$$\langle I(t)I(t+\tau) \rangle \leq \langle I(t)^2 \rangle \tag{2.10}$$

or

$$g^{(2)}(\tau) \leq g^{(2)}(0) \tag{2.11}$$

2.3 Single-mode quantum optics

For a single-mode light field, $g^{(2)}$ is simplified to

$$g^{(2)}(\tau) = \frac{\langle \hat{a}^\dagger \hat{a}^\dagger \hat{a} \hat{a} \rangle}{(\langle \hat{a}^\dagger \hat{a} \rangle)^2} \tag{2.12}$$

Expressing $g^{(2)}$ with the photon number operator

$$g^{(2)}(\tau) = \frac{\langle n(n-1) \rangle}{(\langle n \rangle)^2} = 1 + \frac{(\Delta n)^2 - \langle n \rangle}{(\langle n \rangle)^2} \tag{2.13}$$

where the photon-number variance $(\Delta n)^2 \equiv \langle n^2 \rangle - \langle n \rangle^2 \geq 0$. For number states, or Fock states, where $(\Delta n)^2 = 0$, $g^{(2)}(\tau) = 1 - \frac{1}{n}$. It obvious goes beyond the classical limit set by Eq. 2.8.

Another important state of light is the coherent state. It follows the Poisson

distribution

$$|\alpha\rangle = \exp(-\frac{1}{2}|\alpha|^2)\sum_{n=0}^{\infty}\frac{\alpha^n}{\sqrt{n!}}|n\rangle \tag{2.14}$$

Poisson distribution has an rth factorial moment of the simple form

$$\langle n(n-1)(n-2)\cdots(n-r+1)\rangle = \langle n\rangle^r \tag{2.15}$$

Therefore,

$$g^{(2)}(\tau) = 1 \tag{2.16}$$

2.4 Hanbury Brown-Twiss intensity interferometry

Hanbury Brown-Twiss intensity interferometry was originally developed by Hanbury-Brown and Twiss in the 1950s [32,33], for studying the light from distant stars. Now it is a routine technique to measure the intensity correlations. The setup is illustrated in Fig. 2-1. We would like to measure the second-order intensity correlation function $g^{(2)}$ of the light source, whose state is represented as $|\psi\rangle$. The light source is passed through a 50/50 beamsplitter, and two single-photon detectors are placed at the two output ports of the beamsplitter. $g^{(2)}$ is then given by the coincidence counts with proper normalization. $\hat{a}$, $\hat{b}$, $\hat{c}$ and $\hat{d}$ denote the annihilation operator of the four input and output modes of the beamsplitter, as labeled in Fig. 2-1.

The unitary transformation by the beamsplitter is defined by

$$\begin{aligned}\hat{c} &= \frac{\hat{a}+\hat{b}}{\sqrt{2}}\\ \hat{d} &= \frac{\hat{a}-\hat{b}}{\sqrt{2}}\end{aligned} \tag{2.17}$$

The coincidence signal can expressed by

$$\langle\psi, 0|\hat{c}^\dagger\hat{c}\hat{d}^\dagger\hat{d}|\psi, 0\rangle \tag{2.18}$$

Applying Eq. 2.17 to Eq. 2.18, it is easy to show that Eq. 2.18 is proportional to $\langle \psi, 0 | \hat{a}^\dagger \hat{a}^\dagger \hat{a} \hat{a} | \psi, 0 \rangle$. With proper normalization, this gives $g^{(2)}$ as in Eq. 2.12. This is a remarkable result, because without splitting the light source into two modes, as seen from Eq. 2.13, due to the commutation relation of the creation and annihilation operator, $g^{(2)}$ cannot be extracted from a simple coincidence measurement.

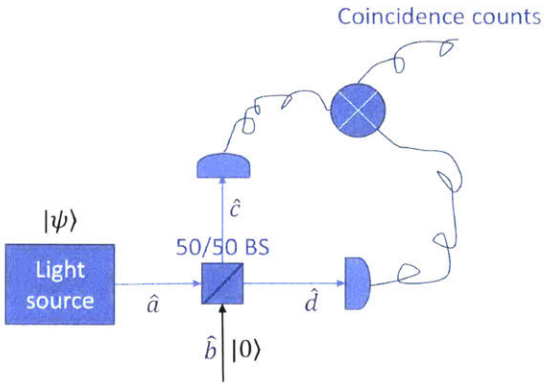

Figure 2-1: **The setup of the Hanbury Brown-Twiss intensity interferometry.**

2.5 Multi-mode quantum optics

We now consider continuous modes. First, let us look at the Fock state of photon number 2.

$$|\Psi\rangle = \frac{1}{\sqrt{2}} \int dt_1 dt_2 \psi_2(t_1, t_2) \hat{a}^\dagger(t_1)) \hat{a}^\dagger(t_2) |0\rangle \tag{2.19}$$

$\hat{a}^\dagger(t)$ is the creation operator at time t, which satisfies the commutation relations $[\hat{a}(t), \hat{a}(t')] = \delta(t - t')$. The normalization of the wavefunction Ψ

$$\langle \Psi | \Psi \rangle = 1 \tag{2.20}$$

requires the probability amplitude ψ_2

$$\int dt_1 \int dt_2 |\psi_2(t_1, t_2)|^2 = 1 \tag{2.21}$$

$$g^{(2)}(\tau) = \frac{\langle\Psi|\hat{a}^\dagger(T_1)\hat{a}^\dagger(T_1+\tau)\hat{a}(T_1+\tau)\hat{a}(T_1)|\Psi\rangle}{\langle\Psi|\hat{a}^\dagger(T_1)\hat{a}(T_1)|\Psi\rangle\langle\Psi|\hat{a}^\dagger(T_1+\tau)\hat{a}(T_1+\tau)|\Psi\rangle} = \frac{2|\psi_2(T_1,T_1+\tau)|^2}{(2\int dt_1|\psi_2(T_1,t_1)|^2)(2\int dt_1|\psi_2(t_1,T_1+\tau)|^2)} \tag{2.22}$$

If there is no correlation dictated by ψ_2–the probability of finding one photon at T_1, $P_1 = \int dt_1|\psi_2(T_1,t_1)|^2$, and the probability of finding one photon at $T_1+\tau$, $P_2 = \int dt_1|\psi_2(t_1,T_1+\tau)|^2$, are independent, then according to the product rule, the probability of finding two photons at T_1 and $T_1+\tau$, $|\psi_2(T_1,T_1+\tau)|^2$, equals the product of P_1 and P_2. In this case, we recover the single-mode $n=2$ Fock state result $g^{(2)}(\tau) = \frac{1}{2}$.

However, ψ_2 can incorporate photon correlations such as bunching (antibunching)–increased (reduced) probability to have two photon in vicinity, as well as τ dependence. This shows the richness of multi-mode quantum optics, and is explored extensively in our experiments.

As can be seen from $g^{(2)}$ of Fock states, quantum states of light have access to a larger range of $g^{(2)}$ compared to their classical counterparts. To summarize, the two limits of $g^{(2)}$ (Eqs. 2.8 and 2.11) do not apply to quantum states of light. In particular,

$$g^{(2)}(\tau) > g^{(2)}(0) \tag{2.23}$$

is called antibunched, and

$$g^{(2)}(0) < 1 \tag{2.24}$$

is called sub-Poissonian.

2.6 The third-order intensity correlation function

The definition and measurement of $g^{(2)}$ can be readily extended to the nth order correlation $g^{(n)}$. In particular, the third-order correlation function

$$g^{(3)}(\tau_1,\tau_2) = \frac{\langle\Psi|\hat{a}^\dagger(T_1)\hat{a}^\dagger(T_1+\tau_1)\hat{a}^\dagger(T_1+\tau_2)\hat{a}(T_1+\tau_2)\hat{a}(T_1+\tau_1)\hat{a}(T_1)|\Psi\rangle}{\langle\Psi|\hat{a}^\dagger(T_1)\hat{a}(T_1)|\Psi\rangle\langle\Psi|\hat{a}^\dagger(T_1+\tau_1)\hat{a}(T_1+\tau_1)|\Psi\rangle\langle\Psi|\hat{a}^\dagger(T_1+\tau_2)\hat{a}(T_1+\tau_2)|\Psi\rangle} \tag{2.25}$$

It characterizes the probability of finding three photons separated by τ_1 and τ_2, normalized by three independent photons (Poisson distribution).

Chapter 3

Properties of Rydberg atoms and their interactions

There are several review papers readily available owing to the rapid development of Rydberg quantum optics and Rydberg-coupled atomic systems. For the properties of the Rydberg atoms and their application in quantum information, see Ref. [42]. For quantum nonlinear optics, see Ref. [43].

3.1 Decoherence and decay of a Rydberg atom in a dense cloud

Counterintuitively, the 0K radiative lifetimes of Rydberg states are very long due to the small overlap of the wavefunction of the highly-excited electron with that of the ground state. The dependence of the principal quantum number n can be approximated by

$$\tau_{nl}^{(0)} = \tau_{l}^{(0)}(n - \delta_l)^{\alpha_l}, \qquad (3.1)$$

where δ_l is a quantum defect of an nl Rydberg state and $\alpha_l \simeq 3$ for all the alkalis. The scaling coefficients $\tau_l^{(0)}$ and α_l can be found in Ref. [44].

At room temperature (300K), the lifetime is limited by the black-body radiation

for large n, which is given by (including blackbody induced photoionization)

$$\tau_{nl}^{(bb)} = \frac{3\hbar(n-\delta_l)^2}{4\alpha^3 k_B T}, \tag{3.2}$$

where α is the fine-structure constant [45]. Taking $100S_{1/2}$ in ^{87}Rb for example, $\tau_{nl}^{(0)} = 1.3ms$ and $\tau_{nl}^{(bb)} = 0.5ms$ at 300K.

Combining both effects, the lifetime can be calculated as

$$\frac{1}{\tau_{nl}} = \frac{1}{\tau_{nl}^{(0)}} + \frac{1}{\tau_{nl}^{(bb)}} \tag{3.3}$$

It is worth noting that the black-body radiation couples mainly to a nearby Rydberg state, in contrast to the 0K radiative decay, which couples predominantly to the ground state. This can lead to complicated dynamics in an experiment with an ensemble of atoms [46], since the contaminant Rydberg atoms can interact with the desired Rydberg atoms, and such interaction may be even stronger than the interaction between the desired Rydberg atoms.

	to a ground state	to a nearby Rydberg state
BB	$\propto \omega^2\langle r\rangle^2 \propto n^0(n^{-\frac{3}{2}})^2 \propto n^{-3}$	$\propto \omega^2\langle r\rangle^2 \propto (n^{-3})^2(n^2)^2 \propto n^{-2}$
0K	$\propto \omega^3\langle r\rangle^2 \propto n^0(n^{-\frac{3}{2}})^2 \propto n^{-3}$	$\propto \omega^3\langle r\rangle^2 \propto (n^{-3})^3(n^2)^2 \propto n^{-5}$

Table 3.1: **The scalings of transition probabilities coupled by black-body radiation and spontaneous emission.** The transition frequency from a ground state to a Rydberg state is roughly the same as the ground state (ionization) energy, independent of n. The transition frequency between nearby Rydberg states is proportional to n^{-3} because the (ionization) energy of Rydberg states scales as n^{-2}. The scaling of the radial matrix elements can be found in Ref. [42]. As can be easily seen, the black-body radiation predominantly couples to a nearby Rydberg state (n^{-2}), while the 0K radiative decay prefers to couple to a ground state (n^{-3}).

Besides, due to the large size of the Rydberg atoms, there can be many ground-state atoms within the orbit of the Rydberg electron. When the principal number n or the atomic density is not too high, this leads to the formation of Rydberg molecules [47–50]–an intriguing field that has been explored extensively. As n or the atomic density increases, the Rydberg electron can catch more and more ground-state atoms, and the molecular lines can no longer be resolved resulting in a shift and

broadening of the Rydberg state [51]. Reduced coherence time [52] and lifetime [53] caused by this mechanism have been reported.

3.2 Rydberg interactions

3.2.1 Interactions between the same Rydberg states

At interatomic distances $R \gg n^2 a_0$ separating two Rydberg atoms A and B, the leading electrostatic interaction is the dipole-dipole interaction

$$V_{dd} = \frac{e^2}{R^3}(\vec{a}\cdot\vec{b} - 3\vec{a}\cdot\hat{\vec{R}}\hat{\vec{R}}\cdot\vec{b}) \tag{3.4}$$

where a and b are the positions of the two Rydberg electrons measured from their respective nuclei. At such large distances, overlap between the atoms can be neglected.

For two identical Rydberg atoms, we consider the long-range interaction between Rydberg atoms as arising predominantly from two coupled channels $nlj + nlj$ and $n_a l_a j_a + n_b l_b j_b$ with an energy difference $\delta = E(n_a l_a j_a) + E(n_b l_b j_b) - 2E(nlj)$. Representing the $nlj + nlj$ components of the wavefunction as φ and the $n_a l_a j_a + n_b l_b j_b$ components as $|\chi\rangle$, the time-independent Schrödinger equation describing the dipole-dipole interaction is

$$\begin{pmatrix} \delta\cdot I_\chi & V_{dd} \\ V_{dd}^\dagger & 0\cdot I_\varphi \end{pmatrix} \begin{pmatrix} |\chi\rangle \\ |\varphi\rangle \end{pmatrix} = \Delta \begin{pmatrix} |\chi\rangle \\ |\varphi\rangle \end{pmatrix}$$

Here, I_χ and I_φ are indentity matrices on the $2(2j_a+1)(2j_b+1)$ (or $(2j_a+1)^2$ if $(n_a, l_a, j_a) = (n_b, l_b, j_b)$) and $(2j+1)^2$ dimensional Hilbert subspaces of the $|\chi\rangle$ and $|\varphi\rangle$ wavefunction components, respectively.

There exists a crossover distance R_c: At large distances $R \gg R_c$, the energy shift is of the van der Waals form C_6/R^6; at small distances, $R \ll R_c$, the two channels takes the resonant dipole-dipole form C_3/R^3. Although on most occasions we are interested in the energy shift, it is worth noting that the dipole-dipole interaction

is an exchange interaction in nature. Namely, if the system is initially prepared in $nlj+nlj$, it will oscillates between $nlj+nlj$ and $n_al_aj_a+n_bl_bj_b$ due to the interaction. Such oscillations have been observed by S. Ravets et al. [54].

It is extremely rare to have the resonant R^{-3} interaction at relevant length scales without external fields. It has been demonstrated that by applying a dc [22, 54] or microwave [55] electric field, the two dipole-coupled pair states can be tuned into resonance.

3.2.2 Interactions between two different Rydberg states

The interaction between two atoms in distinct levels Rydberg levels R and R' has the general form

$$V = \begin{pmatrix} V_b(r) & V_{ex}(r) \\ V_{ex}(r) & V_b(r) \end{pmatrix}$$

in the two-atom product basis $\{|RR'\rangle, |R'R\rangle\}$. Here, r is the distance between the atoms. For levels R, R' with $\Delta L = \pm 1$, the dominant interaction will likely to be the direct dipolar interaction $V_{ex}(r) = C_3/r^3$. Because this interaction is not diagonal in the product basis, its action is to exchange the states $|RR'\rangle$ and $|R'R\rangle$. This case describes, for example, the interaction between the $|100S_{1/2}, m_J = 1/2\rangle$ and $|99P_{3/2}, m_J = 3/2\rangle$ states. For these states, V_b is negligible at the relevant length scales (less than 5% of V_{ex} at $r = 20\mu m$).

In contrast, for same-parity levels, the direct dipolar interaction is not allowed, so the dominant interaction is second-order, such that $V_b(r) = C_6/r^6$ and $V_{ex}(r) = \chi_6/r^6$. For states with widely separated principal quantum numbers, $|C_6| \gg |\chi_6|$. However, if the principal quantum numbers of the R, R' states are similar, χ_6 can be comparable to C_6. When $|C_6| \gg |\chi_6|$, the interaction does not lead to exchange of Rydberg excitations, but only shifts the combined energy, as is typically assumed for Rydberg blockade (and must be true when $R = R'$). In contrast, when $|C_6| \approx |\chi_6|$ state exchange is also possible.

Chapter 4

EIT

In this chapter, I will briefly review electromagnetically induced transparency (EIT) with the emphasis on the key ingredients in our experiments. Numerous papers are available for a fuller description. Ref. [56] provides a comprehensive review. Ref. [57] and the Supplemental Material of Ref. [58] beautifully describe the polariton picture.

4.1 Transmission through a medium with EIT

First, consider the probe is coupled to $|g\rangle \rightarrow |e\rangle$ transition, as illustrated in Fig. 4-1. On resonance, the probe would be strongly scattered, and off resonance, acquire a phase shift. Then, consider adding the control field and the third level $|r\rangle$. Due to the cancellation of the linear response by destructive interference in the laser-dressed medium, the probe sees a transparent medium on two-photon resonance $\delta = 0$.

We now turn to quantative analysis. Consider the evolution of the slowly varying operators $\hat{\mathcal{E}}^\dagger(z)$, $\hat{\mathcal{P}}^\dagger(z)$ and $\hat{\mathcal{S}}^\dagger(z)$ corresponding to the creation of a photon, an intermediate-state excitation ($|e\rangle$) and a Rydberg excitation ($|r\rangle$), respectively, at position z. These operators satisfy the same-time commutation relations $[\hat{\mathcal{E}}(z), \hat{\mathcal{E}}^\dagger(z')] = [\hat{\mathcal{P}}(z), \hat{\mathcal{P}}^\dagger(z')] = [\hat{\mathcal{S}}(z), \hat{\mathcal{S}}^\dagger(z')] = \delta(z - z')$. The Heisenberg equations of motion are

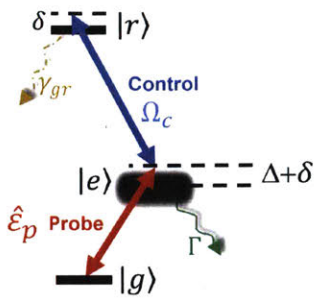

Figure 4-1: **Generic system for EIT:** probe field of frequency ω_p and control field of frequency ω_c. In an ideal EIT, $|e\rangle$ is assumed to be the only decaying state with decay rate Γ. Realistically, $|r\rangle$ has a small decay rate γ_{gr}.

given by

$$\begin{aligned}
\partial_t\hat{\mathcal{E}}(z,t) &= -c\partial_z\hat{\mathcal{E}}(z,t) + i\frac{g_p}{2}\sqrt{\rho(z)}\hat{\mathcal{P}}(z,t) \\
\partial_t\hat{\mathcal{P}}(z,t) &= -(\frac{\Gamma}{2} - i(\Delta+\delta))\hat{\mathcal{P}}(z,t) + i\frac{g_p}{2}\sqrt{\rho(z)}\hat{\mathcal{E}}(z,t) + i\frac{\Omega_c}{2}\hat{\mathcal{S}}(z,t) \\
\partial_t\hat{\mathcal{S}}(z,t) &= -(\frac{\gamma_{gr}}{2} - i\delta)\hat{\mathcal{S}}(z,t) + i\frac{\Omega_c}{2}\hat{\mathcal{P}}(z,t)
\end{aligned} \tag{4.1}$$

where the peak atom-photon coupling constant g_p is defined as $\frac{g_p^2}{\Gamma c} = \frac{OD}{\sqrt{2\pi}\sigma_a}$, the Gaussian atomic density $\rho(z) = e^{-\frac{z^2}{2\sigma_a^2}}$, normalized by the peak density ρ_0, and σ_a is the axial rms length of the atomic cloud. The one-photon detuning $\Delta = \omega_{re} - \omega_{control}$ and two-photon detuning $\delta = \omega_{probe} + \omega_{control} - \omega_{rg}$. Here ω_{probe} and $\omega_{control}$ are the probe and control frequencies, and ω_{re} and ω_{rg} are the $|e\rangle \rightarrow |r\rangle$ and $|g\rangle \rightarrow |r\rangle$ transition frequencies, respectively. The Langevin noise is omitted since it does not affect our calculations.

Assume a weak coherent state input of the probe

$$\exp[\alpha \int dz\, (\hat{\mathcal{E}}^\dagger(z) - \hat{\mathcal{E}}(z))]|0\rangle \tag{4.2}$$

α is assumed to be real for simplicity. The single-photon probability amplitude is defined as $E(z) = \langle 0|\hat{\mathcal{E}}(z)|\Psi\rangle$, where $|\Psi\rangle$ is the state of the system.

The steady-state solution of Eq. 4.1 gives

$$
\begin{aligned}
E(z) &= \alpha \exp[-\frac{\frac{\Gamma}{2}(\frac{\gamma_{gr}}{2}-i\delta)\frac{OD}{2}}{(\frac{\Omega_c}{2})^2+(\frac{\Gamma}{2}-i(\Delta+\delta))(\frac{\gamma_{gr}}{2}-i\delta)}\int_{-z/2}^{z/2}\rho(z')\frac{dz'}{\sqrt{2\pi}\sigma_a}] \\
P(z) &= \frac{c}{ig_p\sqrt{\rho(z)}/2}\partial_z E(z) = \frac{i\frac{g_p\sqrt{\rho(z)}}{2}(\frac{\gamma_{gr}}{2}-i\delta)}{(\frac{\Omega_c}{2})^2+(\frac{\Gamma}{2}-i(\Delta+\delta))(\frac{\gamma_{gr}}{2}-i\delta)}E(z) \\
S(z) &= \frac{\Omega_c}{g_p\sqrt{\rho(z)}}\frac{c}{\gamma_{gr}/2-i\delta}\partial_z E(z) \\
&= -\frac{g_p\sqrt{\rho(z)}}{\Omega_c}\frac{1}{[1+(\frac{\Gamma}{2}-i(\Delta+\delta))(\frac{\gamma_{gr}}{2}-i\delta)/(\Omega_c/2)^2]}E(z)
\end{aligned}
\tag{4.3}
$$

Note that these boundary conditions satisfy the ideal dark-polariton relationship Eq. 4.20 when $\gamma_{gr} = \delta = 0$.

At the exit of the medium

$$
E(z \gg \sigma_a) = \alpha \exp[-\frac{\frac{\Gamma}{2}(\frac{\gamma_{gr}}{2}-i\delta)\frac{OD}{2}}{(\frac{\Omega_c}{2})^2+(\frac{\Gamma}{2}-i(\Delta+\delta))(\frac{\gamma_{gr}}{2}-i\delta)}] \tag{4.4}
$$

This formula (divided by α) is used to obtain the blue and gray dashed curves in Fig. 6-13.

The amplitude transfer function, according to Eq. 4.4, can be written as

$$
e^{ikL\chi^{(1)}/2} \tag{4.5}
$$

with the real and imaginary part of the linear susceptibility $\chi^{(1)}$

$$
Re[\chi^{(1)}] = -\frac{OD\Gamma}{2kL}\frac{((\frac{\gamma_{gr}}{2})^2+\delta^2)(\delta+\Delta)-\delta(\frac{\Omega_c}{2})^2}{(\frac{\Gamma}{2}\delta+\frac{\gamma_{gr}}{2}(\delta+\Delta))^2+(\frac{\Gamma}{2}\frac{\gamma_{gr}}{2}-\delta(\delta+\Delta)+(\frac{\Omega_c}{2})^2)^2} \tag{4.6}
$$

$$
Im[\chi^{(1)}] = \frac{OD\Gamma}{2kL}\frac{\frac{\Gamma}{2}(\frac{\gamma_{gr}}{2})^2+\frac{\Gamma}{2}\delta^2+\frac{\gamma_{gr}}{2}(\frac{\Omega_c}{2})^2}{(\frac{\Gamma}{2}\delta+\frac{\gamma_{gr}}{2}(\delta+\Delta))^2+(\frac{\Gamma}{2}\frac{\gamma_{gr}}{2}-\delta(\delta+\Delta)+(\frac{\Omega_c}{2})^2)^2} \tag{4.7}
$$

where Ω_c is the control Rabi frequency and OD is the optical depth. With an ideal EIT ($\gamma_{gr} = 0$), on resonance $\delta = 0$, both the real and imaginary part of $\chi^{(1)}$ vanish. Namely, there is no phase shift ($Re[\chi^{(1)}]$) or absorption ($Im[\chi^{(1)}]$). With finite decoherence γ_{gr}, Eq. 4.6 shows that $Re[\chi^{(1)}] = 0$ when $\delta = \frac{\gamma_{gr}^2\Delta}{\Omega_c^2} + \mathcal{O}(\gamma_{gr}^4)$. Eq. 4.7 shows

that the peak linear transmission is at $\delta = -\frac{\Delta\gamma_{gr}}{\Gamma} + \mathcal{O}(\gamma_{gr}^2)$. When $|\Delta| \gg \Gamma$, the peak (Raman) absorption is at $\delta = \frac{\Omega_c^2}{4\Delta}(1 - \frac{\gamma_{gr}^2}{\Omega_c^2})(1 + \frac{\Gamma\gamma_{gr}}{\Omega_c^2}) + \mathcal{O}(\Delta^{-3})$.

In the experiments, we use $\delta = 0$ as our nominal EIT resonance. When $\Delta = 0$, it coincides with the peak transmission, which is located at the center of the absorption feature. When $\Delta \neq 0$, we move the probe and control laser frequencies by the nominal amount after we determine the resonance at $\Delta = 0$.

When $\Delta = 0$, the transmission (intensity transfer function)

$$\exp[-\frac{OD}{1 + \frac{\Omega_c^2}{\Gamma\gamma_{gr}}}] \tag{4.8}$$

Hence, the condition to see the EIT features is $\frac{\Omega_c^2}{\Gamma\gamma_{gr}} \gtrsim OD(\gtrsim 1)$.

We now look at the widths of the EIT features. For simplicity, set $\gamma_{gr} = 0$. Taking the leading order in δ, the transmission $e^{-kLIm[\chi^{(1)}]}$ is a Gaussian with rms

$$\frac{\Omega_c^2}{2\sqrt{2OD}\Gamma} \tag{4.9}$$

This is the EIT transparency width. Note, however, when $|\Delta| \gg \Gamma$, the transmission peak is highly asymmetric, with one side falling down sharply to the Raman absorption at $\delta = \frac{\Omega_c^2}{4\Delta}$ (Fig. 4-2(a)).

When $\Delta = 0$, Eq. 4.7 have two maximums (minimum transmission) located at $\delta = \pm\frac{\Omega_c}{2}$. When $OD \lesssim 1$ and $\Omega_c > \Gamma$, the absorption peaks are sharp and can be easily located. Fig. 4-2(b) shows a spectrum in such regime, which can be compared with Fig. 4-2(d), where $\Omega_c < \Gamma$ and thus the spectrum looks more like a transmission peak sitting on top of an absorption feature with width Γ. The regime shown in Fig. 4-2(b), where the two absorption peaks are split, is called Autler-Townes (AT) splitting. The splitting provides a good measurement of Ω_c experimentally.

We can define an EIT linewidth as the FWHM of $-Im[\chi^{(1)}]$, whose maximum at $\delta = 0$ and two minimums at $\delta = \pm\frac{\Omega_c}{2}$, resulting in $\gamma_{EIT} = \frac{\Omega_c^2}{\Gamma}$. Compared with Eq. 4.9, the EIT linewidth is much broader than the EIT transparency window, when $OD \gg 1$. The optically thick medium filters the probe in frequency space and

broadens the pulse in real space, which dictates the width of the anti-bunching feature in $g^{(2)}$ (Figs. 6-3 and 6-20). When $|\Delta| \gg \Gamma$, $\gamma_{EIT} = \frac{\Omega_c^2}{2|\Delta|}$, defined by the detuning of the Raman absorption resonance.

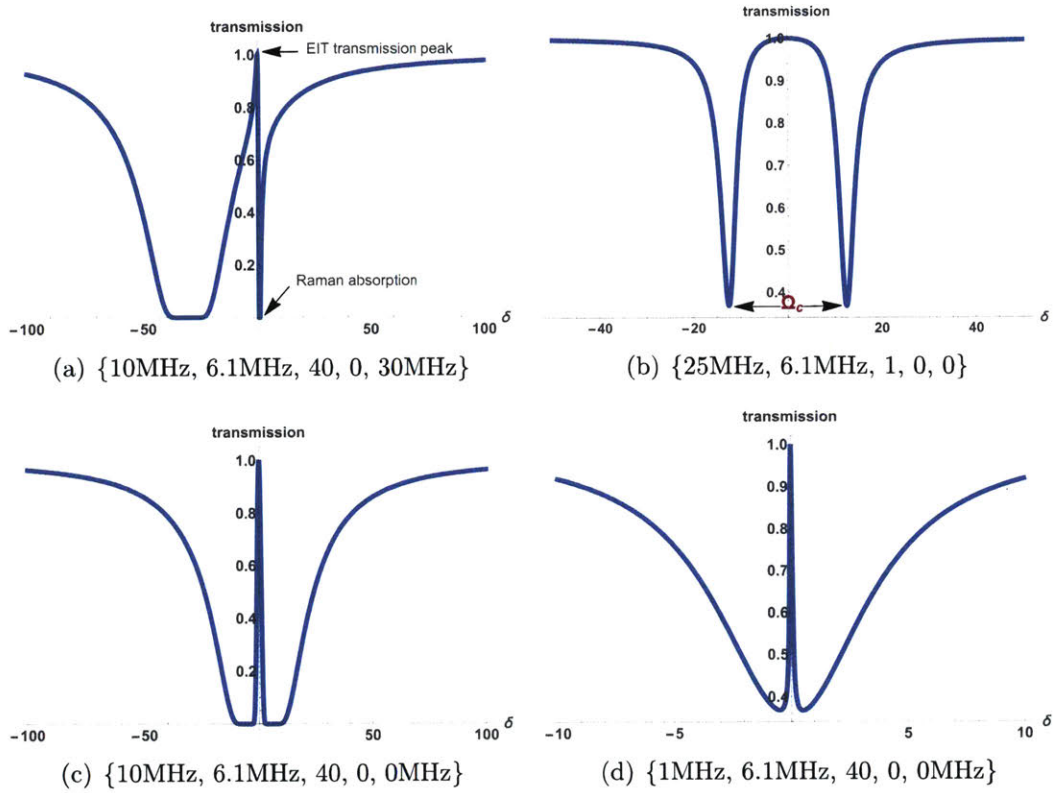

(a) {10MHz, 6.1MHz, 40, 0, 30MHz}

(b) {25MHz, 6.1MHz, 1, 0, 0}

(c) {10MHz, 6.1MHz, 40, 0, 0MHz}

(d) {1MHz, 6.1MHz, 40, 0, 0MHz}

Figure 4-2: **Examples of EIT transmission vs the two-photon detuning δ with various parameter sets $\{\Omega_c, \Gamma, OD, \gamma_{gr}, \Delta\}$.**

4.2 Slow light

Consider a monochromatic plane wave $Ee^{i(kz-\omega t)}$ of angular frequency ω propagating through a medium of refractive index n, where $k = n\omega/c$. We define the phase velocity v_p to be the velocity at which points of constant phase move through the medium. The phase of this wave is given by $\phi = kz - \omega t$. Points of constant phase move a distance Δz in a time Δt, which are related by $k\Delta z = \omega \Delta t$. Thus, $v_p = \frac{\Delta z}{\Delta t} = \frac{\omega}{k} = \frac{c}{n}$.

Next, we look at the propagation of a pulse through a medium. A pulse is necessarily composed of a spread of optical frequencies. At the peak of the pulse, the

various Fourier components will tend to add up in phase. If this pulse is to propagate without distortion, these components must add in phase for all values of the propagation distance z. That is,

$$\frac{d\phi}{d\omega} = 0 \Rightarrow \frac{dn}{d\omega}\frac{\omega z}{c} + \frac{nz}{c} - t = 0 \tag{4.10}$$

The group velocity

$$v_g \equiv \frac{z}{t} = \frac{c}{n + \omega\frac{dn}{d\omega}} = \frac{d\omega}{dk} \tag{4.11}$$

The last equality results from $k = n\omega/c$. This description assumes that the pulse does not undergo significant distortion.

Slow light refers to the situation $v_g \ll c$. Fast light refers to $v_g > c$ or $v_g < 0$. A negative v_g corresponds to the case when the peak of the pulse transmitted through a medium emerges before it enters the medium. Slow and fast light invariably make use of the rapid variation of refractive index (the $\frac{dn}{d\omega}$ term in v_g).

Close to EIT resonance $\delta \simeq 0$ and assuming $\gamma_{gr} = 0$,

$$n = \sqrt{1 + Re[\chi^{(1)}]} \approx 1 + \frac{OD\Gamma\delta}{kL\Omega_c^2} \tag{4.12}$$

Therefore,

$$v_g = \frac{c}{n + \omega_p\frac{dn}{d\omega_p}} \approx \frac{L}{\frac{OD\Gamma}{\Omega_c^2}} \tag{4.13}$$

The group delay τ_d measures how much longer it takes the pulse to propagate through the medium than travelling the same distance in vacuum.

$$\tau_d = \frac{L}{v_g} - \frac{L}{c} = \frac{OD\Gamma}{\Omega_c^2} \tag{4.14}$$

Both slow and fast light have been measured. L. V. Hau et al. [51] observe group velocities smaller than $17m/s$ enabled by EIT. L. J. Wang, A. Kuzmich and A. Dogariu [52] engineer a negative group velocity $-c/310$ by using two control beams detuned from each other by 2Δ, leading to two EIT resonances separated by 2Δ, between which $\frac{dn}{d\omega} < 0$.

4.3 Polaritons

The interaction of probe and control fields with the three-level atoms can be described by the atom-light coupling Hamiltonian in a rotating frame

$$\hat{H} = \int d^3\mathbf{r} \{-\Delta\hat{\Sigma}_{ee}(\mathbf{r}) - \delta\hat{\Sigma}_{rr}(\mathbf{r}) + \Omega\hat{\Sigma}_{re}e^{i\mathbf{q}_c\cdot\mathbf{r}} + g\sqrt{n}\hat{\mathcal{E}}(\mathbf{r})\hat{\Sigma}_{eg}e^{i\mathbf{q}_p\cdot\mathbf{r}} + H.a.\} \quad (4.15)$$

where n is the atomic density, $g = \mathcal{D}\sqrt{\frac{\omega_p}{2\hbar\epsilon_0}}$ with the $|g\rangle - |e\rangle$ dipole moment $\mathcal{D}$, Ω is the control Rabi frequency (half width), and $\mathbf{q}_p$ and $\mathbf{q}_c$ are the wave vector corresponding the carrier frequency ω_p and ω_c, respectively. $\hat{\Sigma}_{\mu\nu}(\mathbf{r}) \equiv \frac{1}{\sqrt{\Delta N}}\Sigma_{j\in\Delta V}|\mu\rangle_{jj}\langle\nu|$ are continuous atomic flip operators defined on a small volume $\Delta V(\mathbf{r})$ centered around position $\mathbf{r}$ containing $\Delta N \gg 1$ atoms. $\Delta = \omega_p - \omega_{eg}$ is the one-photon detuning and $\delta = \omega_p + \omega_c - \omega_{rg}$ is the two-photon detuning. Here ω_p and ω_c are the probe and control frequencies, and ω_{eg} and ω_{rg} are the $|g\rangle \to |e\rangle$ and $|g\rangle \to |r\rangle$ transition frequencies, respectively.

Assuming that all atoms are initially prepared in the ground state $|g\rangle$ and the photon density is much less than the atom density, we can treat the light-atom coupling perturbatively. In the lowest order of the atom-field coupling g, the Heisenberg equations can be written

$$\frac{\partial}{\partial t}\hat{\Sigma}_{ge} = -(-i\Delta + \gamma)\hat{\Sigma}_{ge} + ig\sqrt{n}\hat{\mathcal{E}}e^{i\mathbf{q}_p\cdot\mathbf{r}} + i\Omega\hat{\Sigma}_{gr}e^{-i\mathbf{q}_c\cdot\mathbf{r}} \quad (4.16)$$

$$\frac{\partial}{\partial t}\hat{\Sigma}_{gr} = i\delta\hat{\Sigma}_{gr} + i\Omega\hat{\Sigma}_{ge}e^{i\mathbf{q}_c\cdot\mathbf{r}} \quad (4.17)$$

where γ is the natural linewidth of $|e\rangle$ (half width). The Langevin noise is omitted.

The slowly varying probe-field envelope $\hat{\mathcal{E}}(\mathbf{r}, t)$ in a one-dimensional problem with paraxial approximation satisfies the wave equation

$$[\frac{\partial}{\partial t} + c\frac{\partial}{\partial z}]\hat{\mathcal{E}}(z,t) = ig\sqrt{n}\hat{\Sigma}_{ge}(z,t)e^{i\mathbf{q}_p\cdot\mathbf{r}} \quad (4.18)$$

eqs. (4.16) to (4.18) yield the following matrix equations

$$\frac{\partial}{\partial t}\mathbf{X} = -iH\mathbf{X} \tag{4.19}$$

where $\mathbf{X}^T = \{\hat{\mathcal{E}}, \hat{\Sigma}_{gr}e^{i(\mathbf{q}_p+\mathbf{q}_c)\cdot\mathbf{r}}, \hat{\Sigma}_{ge}e^{i\mathbf{q}_p\cdot\mathbf{r}}\}$, and the Hamiltonian

$$H = \begin{pmatrix} -ic\partial z & 0 & -g\sqrt{n} \\ 0 & -\delta & -\Omega \\ -g\sqrt{n} & -\Omega & -\Delta - i\gamma \end{pmatrix}$$

Changing the basis to a description in terms of dark- and bright-polaritons $\mathbf{Y}^T = \{\hat{\Psi}, \hat{\Phi}, \hat{\Sigma}_{ge}e^{i\mathbf{q}_p\cdot\mathbf{r}}\}$, where the *dark-polariton*

$$\hat{\Psi} = \cos\theta\hat{\mathcal{E}} - \sin\theta\hat{\Sigma}_{gr}e^{i(\mathbf{q}_p+\mathbf{q}_c)\cdot\mathbf{r}} \tag{4.20}$$

the *bright-polariton*

$$\hat{\Phi} = \sin\theta\hat{\mathcal{E}} + \cos\theta\hat{\Sigma}_{gr}e^{i(\mathbf{q}_p+\mathbf{q}_c)\cdot\mathbf{r}} \tag{4.21}$$

and $\tan\theta = g\sqrt{n}/\Omega$, yields the equation of motion $\frac{\partial}{\partial t}\mathbf{Y} = -iH'\mathbf{Y}$ with

$$H' = \begin{pmatrix} -\delta\sin^2\theta + ic\cos^2\theta\partial z & \sin\theta\cos\theta(\delta + ic\partial z) & 0 \\ \sin\theta\cos\theta(\delta + ic\partial z) & -\delta\cos^2\theta + ic\sin^2\theta\partial z & -\Omega_e \\ 0 & -\Omega_e & -\Delta - i\gamma \end{pmatrix}$$

where $\Omega_e = \sqrt{g^2n + \Omega^2}$.

Assuming that the time evolution is slow compared to $|-\Delta - i\gamma|$, we can adiabatically eliminate the optical polarization $\hat{\Sigma}_{ge}$ which yields the coupled equations for dark- and bright-polaritons

$$\frac{\partial}{\partial t}\begin{pmatrix} \hat{\Psi} \\ \hat{\Phi} \end{pmatrix} = -iH''\begin{pmatrix} \hat{\Psi} \\ \hat{\Phi} \end{pmatrix}$$

with

$$H'' = \begin{pmatrix} -\delta \sin^2\theta + ic\cos^2\theta\partial z & \sin\theta\cos\theta(\delta + ic\partial z) \\ \sin\theta\cos\theta(\delta + ic\partial z) & -\delta\cos^2\theta + ic\sin^2\theta\partial z + \frac{\Omega_e^2}{\Delta + i\gamma} \end{pmatrix}$$

In the off-resonant regime $|\Delta| \gg \gamma$, if $|\delta + ic\partial z| \ll \frac{\Omega_e^2}{|\Delta|}$ for all relevant momentum, one recognizes that the off-diagonal coupling terms are small compared to the difference of the diagonal elements. Under this condition, the dynamics of dark- and bright-polaritons approximately separates and one can treat their cross coupling perturbatively. Within this perturbative treatment, the effective equation of motion of the dark-polariton $\hat{\Psi}$ up to second order of the off-diagonal coupling is given by

$$\frac{\partial}{\partial t}\hat{\Psi} = i(\delta\sin^2\theta + ic\cos^2\theta\partial z)\hat{\Psi} + i\frac{\sin^2\theta\cos^2\theta(\delta - ic\partial z)^2}{(\delta - ic\partial z)(\sin^2\theta - \cos^2\theta) + \frac{\Omega_e^2}{\Delta + i\gamma}}\hat{\Psi} \tag{4.22}$$

Taking the leading term of the denominator of the second term on the right-hand side

$$\frac{\partial}{\partial t}\hat{\Psi} = i\delta\sin^2\theta(1 + \frac{\delta\Delta\cos^2\theta}{\Omega_e^2})\hat{\Psi} - ikv_g(1 - 2\frac{\delta\Delta\sin^2\theta}{\Omega_e^2})\hat{\Psi} + i\frac{v_g c\Delta\sin^2\theta}{\Omega_e^2}k^2\hat{\Psi} \tag{4.23}$$

where $k \equiv -i\partial z$ and $v_g = c\cos^2\theta$. The first term on the right-hand side describes an energy offset due to a finite two-photon detuning. The second term accounts for the propagation with the group velocity v_g. The third term describes the quadratic dispersion with effective mass

$$m = -\frac{\Omega_e^2}{2cv_g\Delta\sin^2\theta} = -\frac{\Omega^2}{2v_g^2\Delta}\frac{g^2n + \Omega^2}{g^2n} \xrightarrow{\sin^2\theta\to 1} -\frac{\Omega^2}{2v_g^2\Delta} \tag{4.24}$$

With the effective mass m, Eq. 4.23 can be written as

$$[\frac{\partial}{\partial t} + ikv_g + i\frac{k^2}{2m}]\hat{\Psi} = 0 \tag{4.25}$$

when $\delta = 0$.

From Eq. 4.25, we deduce the dispersion relation

$$\omega(k) = v_g k + \frac{k^2}{2m} \tag{4.26}$$

Thus, the group velocity and mass can be be extracted from the first ($v_g = \frac{d\omega}{dk}$) and second derivative ($\frac{1}{m} = \frac{d^2\omega}{dk^2}$) of the dispersion relation, respectively. It is rather convenient to look at the spectrum of the real part of the susceptibility $Re[\chi^{(1)}]$ (related to the momentum (Eq. 4.5)). After swapping the momentum and energy (or rather, the space and time), the spectrum of $Re[\chi^{(1)}]$ (see the red curve in Fig. 4-3 for an example) can be interpreted as the dispersion relation.

To recover the usual dimensions in the end, we need to scale the results by v_g. More specifically, the group velocity equals the inverse first derivative, and the second derivative needs to be multiplied by v_g^3 to get the inverse mass. Furthermore, in the regime where the medium is lossy, v_g can be negative. In that case, the sign of the mass cannot be solely determined by the second derivative of $\mathrm{Re}[\chi^{(1)}]$.

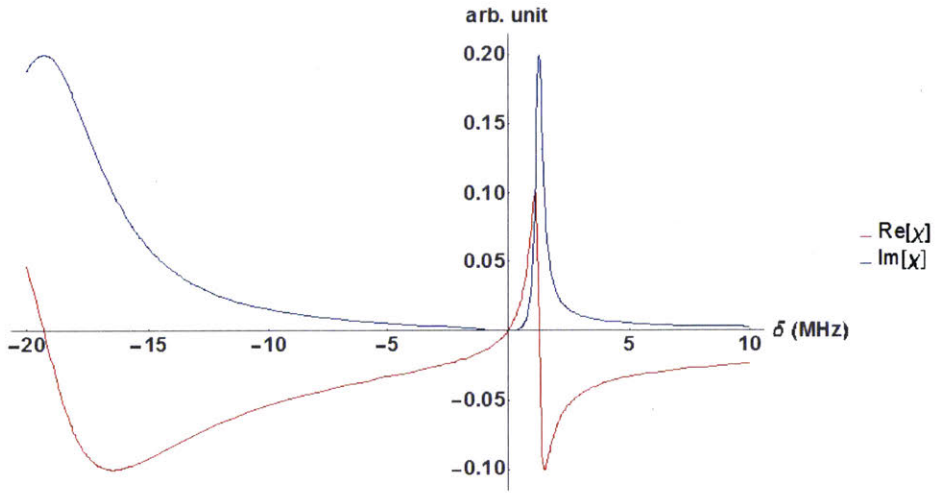

Figure 4-3: **The real (red) and imaginary (blue) parts of $\chi^{(1)}$** with the parameters $\{\Omega_c, \Gamma, OD, \gamma_{gr}, \Delta\}$=$\{10\mathrm{MHz}, 6.1\mathrm{MHz}, 40, 0, 18\mathrm{MHz}\}$.

4.4 Rydberg EIT

In 2001, M. D. Lukin et al. [53] pointed out the possibility to generate non-classical states of light using Rydberg dipole blockade. Afterwards, the blockade was observed through ionization [54–56]. In 2005, I. Friedler et al. [57] proposed to use EIT for a coherent optical detection, which is necessary for light manipulation with Rydberg blockade. The effect of Rydberg blockade on the optical transmission through an ensemble of cold atoms was first demonstrated in 2010 [58]. The first experiments demonstrating single-photon nonlinearity followed in 2012 by Y. O. Dudin and A. Kuzmich [16], D. Maxwell et al. [17], as well as our work described in Chap. 6.

Chapter 5

Experimental setup

Before going into details, I would like to start with an overview of the basic setup that is shared by all the four experiments (despite their variations). As shown in Fig. 5-1, the atoms are prepared in the ground state $|5S_{1/2}, F = 2, m_F = 2\rangle$. The cold ^{87}Rb atoms are loaded from a magneto-optical trap (MOT) to a 1064nm far detuned crossed dipole trap to increase the atomic density. The resulting peak density is $\sim 10^{12} cm^{-3}$, leading to an optical depth per blockade radius (defined in Secs. 6.1.2 and 6.2.3) larger than unity. The trapping light is off when the probe is incident on the cloud to avoid the inhomogeneous light shifts. Along the probe propagation direction, which is also the quantization axis, and the longitudinal axis of the atomic cloud, the rms width of the cloud is $\sim 35\mu m$, which is a few times the blockade radius, allowing us to study the dynamics of probe propagation with the strong interactions. Throughout the experiments we never create static Rydberg atoms. The excitation to the Rydberg states is always part of the Rydberg polariton. With two $f = 3cm$ lenses inside the vacuum chamber, the probe is focused to a Gaussian waist of $4.5\mu m$, less than a blockade radius, so that we can restrict ourselves to a one-dimensional problem, without considering the transverse dynamics. After the probe photons exit the medium, their correlations are preserved and measured by the time-resolved single-photon detections.

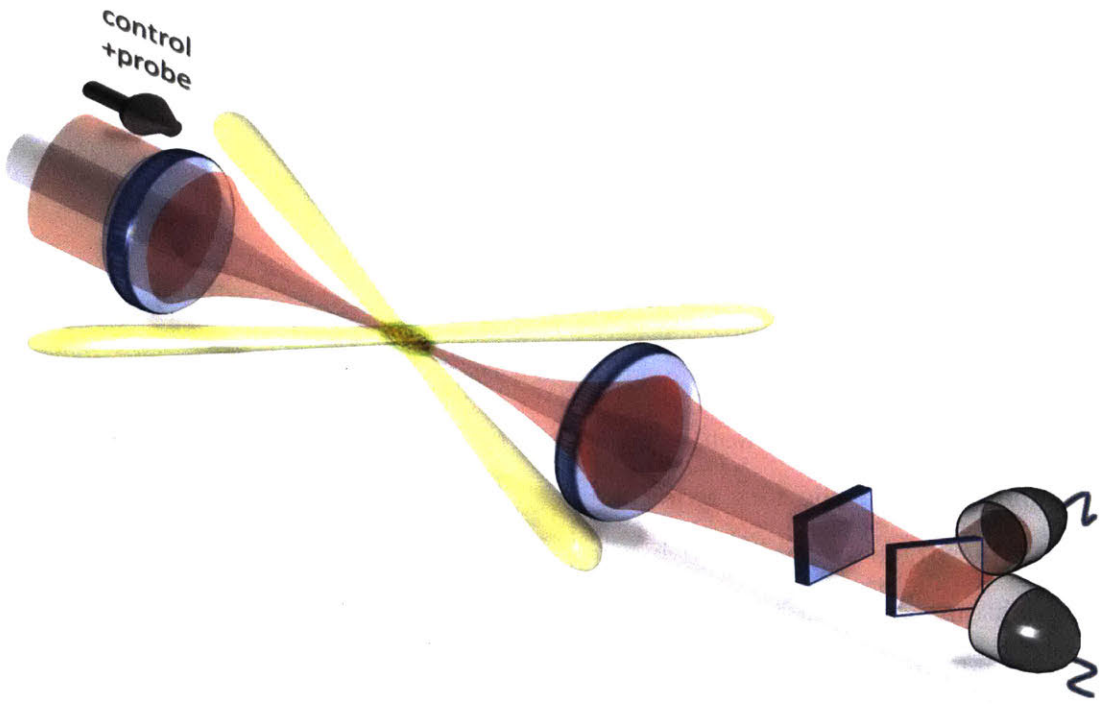

Figure 5-1: **The basic experimental setup.** We load the atoms from MOT into the 1064nm crossed dipole trap (yellow beams). The atoms are optically pumped in the dipole trap into $|5S_{1/2}, F = 2, m_F = 2\rangle$. The probe and control propagate along the quantization axis and are circularly polarized to address the specific magnetic sublevels. The atomic density is increased thanks to the dipole trap such that the optical depth per blockade radius exceeds unity. The two $f = 3cm$ lenses focus the probe and control at the position of the atomic cloud, where the probe waist is smaller than the blockade radius, leading to one-dimensional dynamics. After exiting the atomic cloud, the probe photons are split into single-photon counting modules for photon correlation measurements.

5.1 Probe and control laser systems

A TA-SHG Pro System from Toptica is used as the control laser. A diode laser from Vitaly (Russia) is used as the probe laser.

5.1.1 Pound-Drever-Hall laser locking scheme

We lock both the probe and the control lasers to the transfer cavity (see Sec. 5.1.2 for the details about the transfer cavity). In addition to locking the control whose frequency is far away from the atomic transition, we also take advantage of the narrow cavity linewidth to narrow the laser linewidths (see Sec. 5.1.4 for the results of the laser linewidths). The cavity is temperature-stabilized to 29°C. In order to correct the resonance frequency drift of the cavity mainly due to humidity since the cavity is not evacuated, we actively lock the cavity to the reference laser, which is locked to Rb^{85} (F=3→2)(F=3→3) crossover. The scheme is shown in Fig. 5-2.

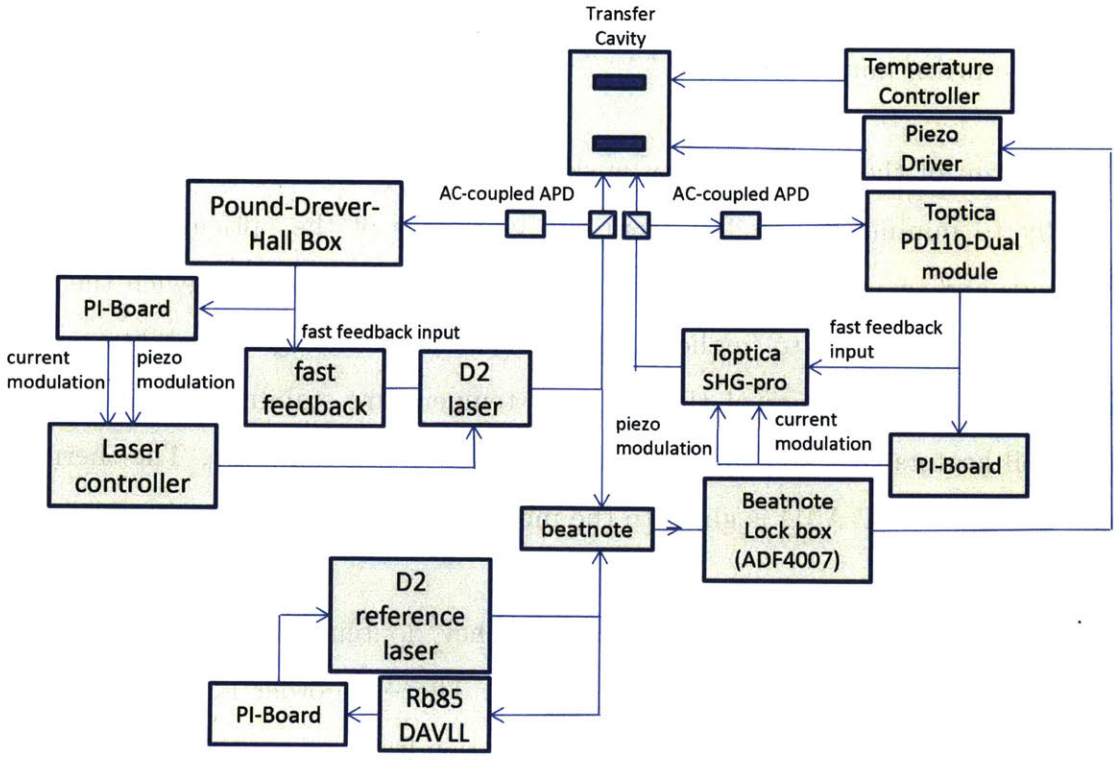

Figure 5-2: **Scheme of the probe and control laser locking system.**

5.1.2 The transfer cavity

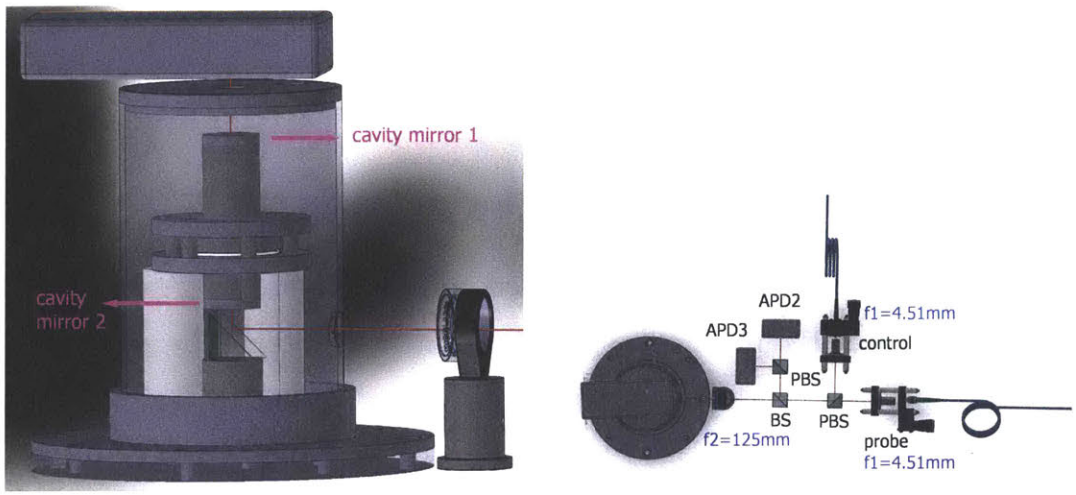

(a) the side view (b) the top view

Figure 5-3: **Transfer cavity setup.** Probe and control laser light has orthogonal polarizations, and therefore can be combined and separated with polarizing beam splitter (PBS). The transmission through the cavity is detected by APD1. APD2 and APD3 detect the probe and control reflection, respectively. The mode-matching lenses have focal lengths $f_1 = 4.51mm$ and $f_2 = 125mm$. Some mirrors are not shown for simplicity in (b). One teflon rod is set to be transparent in order not to block the view of the prism mirror in (a).

The setup of the transfer cavity is sketched in Fig.5-3. The cavity is mounted vertically to minimize the effect from the vibrations of the optical table. Three teflon rods and two teflon washers (between the two plates that sandwich the cavity mirror mount) are used to further damp the vibrations. To gain stability over the temperature, the container of the cavity is temperature stabilized with polyimide thermofoil heaters that are taped on the outer wall of the container. The thermistor (Fenwal 192-103LET-A01) is glued to the mount to which the two cavity mirrors are attached.

Infra-red probe and control (before frequency doubling) laser light is coupled through fiber electro-optic modulators (EOM). The +1st order is used to lock the laser to the cavity. Thus, by varying the modulation frequency of the fiber EOMs, we can easily control the frequency of the probe and control beams in the experiment.

The cavity mirrors have a radius of curvature 5cm. They are mounted with a

distance of about 5.6cm, in order to take the advantage of the near confocal configuration for easy alignment but keep the higher order modes separated in frequency from the fundamental mode. The free spectral range (FSR) is measured by scanning the modulation frequency of the EOM. When the transmission peaks of the $\pm$1st order sidebands overlap with the carrier, the modulation frequency equals (an integer multiple of) the FSR. The mirrors are custom coated by ATFilms to achieve transmission 0.026589% and 0.017434% at the wavelength of 780nm and 958nm, respectively, according to the datasheet. We measure the finesse of the cavity at 958nm with the ring-down measurement [64]. A typical curve of the transmitted power after the laser light is suddenly switched off is shown in Fig.5-4. Assume the power loss is only caused by imperfect mirror reflectivities and the two mirrors are the same. For the control laser, the exponential decay time constant $\tau = 531ns$ of the ring down measurement and the measured FSR= 2.672GHz give finesse $\mathcal{F} = 2\pi \cdot \tau \cdot FSR = 8.9 \times 10^3$. Similarly, the finesse for the probe laser is 6.8×10^3.

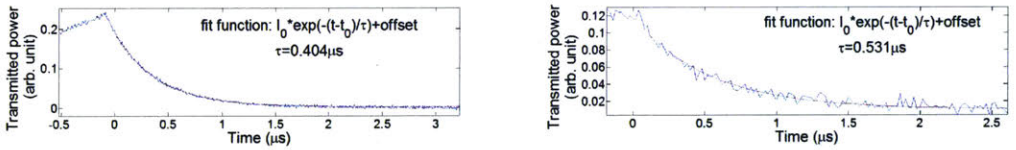

(a) ring-down measurement with the probe laser

(b) ring-down measurement with the control laser

Figure 5-4: **ring-down measurement.** The light is sent to the transfer cavity through fiber EOMs. The modulation frequency jumps (see Anton Mazurenko's Bachelor's thesis [65] for the details about our FPGA based frequency control) by $\pm$10 MHz with a period of $200\mu s$ while the cavity resonance is slowly scanned so that the +1st order sideband can be on resonance at some point. The sudden change of the modulaton frequency moves the light out of the resonance. The transmitted light of the cavity afterwards is the stored light inside the cavity. The decay of such light tells us the information about the finesse. The transmitted light is detected with a home-built avalanche photodetector (Appx. A.1.1) whose bandwidth is about 20MHz. We measured the decay time constant τ to be as low as 50ns when the surface of the cavity mirror is dirty, which again proves that the frequency jump and the detector are fast enough for the ring-down measurement.

Three avalanche photodetectors (APD) are in use. APD1 (Appx. A.1.1) detects the transmission from the cavity to monitor the lock. The other two APDs (Appx.

A.1.2) detect the probe and control laser light that is reflected from the cavity, respectively. Two interference filters (LL01-780-12.5 and LP02-830RS-25 from Semrock) are placed before the APDs to prevent cross detection. The signal from these two APDs is used to generate the error signal for the laser lock.

The beat note of the reference laser and the +1st order of the fiber EOM is divided by a factor of 8, and compared with a local oscillator (direct digital synthesizer AD9958), whose frequency is divided by a factor of 2. The division and comparison are done with a high frequency divider ADF4007. The output flips signs depending on which frequency is higher. Such error signal is sent to the servo controller (Fig. A-8). A piezoelectric transducer (HPCH 150/15-8/3 from Piezomechanik), which is glued to the top mirror, provides feedback to the cavity length.

5.1.3 Parameter tuning of the servo loop

We lock the laser with the PI controller, inject noise into the fast feedback path and measure the gain $M_f = \frac{V_{out}}{V_{in}}$ (Fig. 5-5). Then we lock the laser with both the PI controller and the fast feedback. We inject noise to the PI controller path and measure the gain $M_{PI} = \frac{V_2}{V_1}$ (Fig. 5-6). M_{fast} and M_{PI} are related to the open-loop gain of the fast feedback and the PI controller path by

$$G_f = \frac{M_f(1 - M_{PI})}{1 - M_f M_{PI}} \tag{5.1}$$

$$G_{PI} = \frac{M_{PI}(1 - M_f)}{1 - M_f M_{PI}} \tag{5.2}$$

All the gains here are complex, including both the amplitude and the phase.

We use the extracted open-loop gain to tune the parameters of the fast-feedback circuit (see Fig. 5-7 for the final circuit) and the PI-controller. We try to push the rolling of the phase to as high frequency as possible and meanwhile make sure the amplitude of the gain goes below zero when the phase slips.

For the control laser, the fast feedback works instantaneously by feeding the error

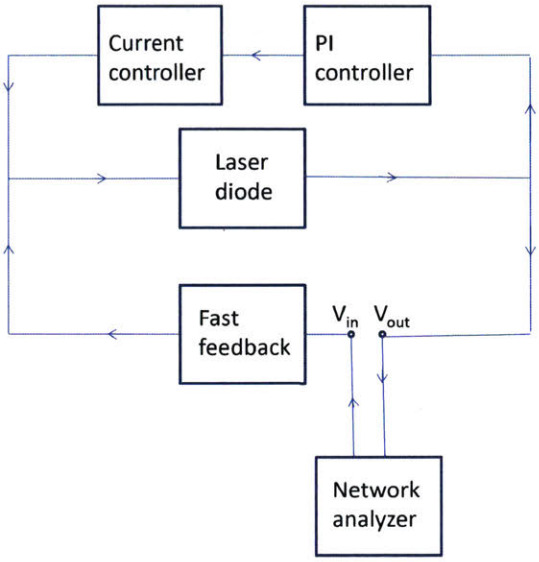

Figure 5-5: **Test circuit when noise is injected into the fast feedback path.**

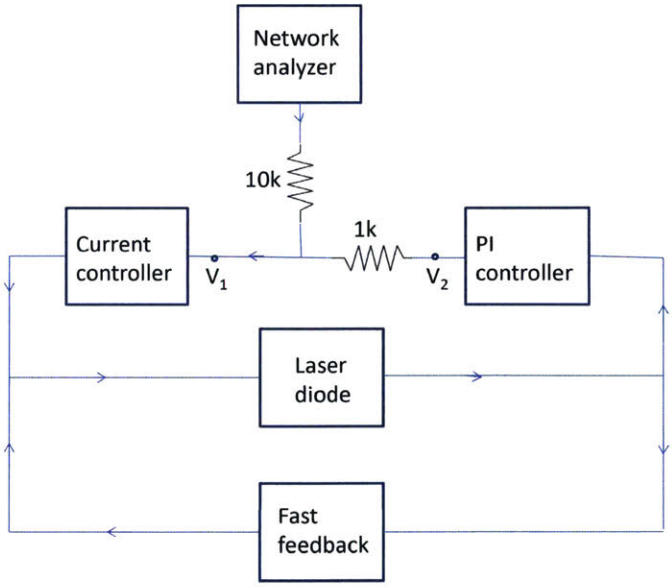

Figure 5-6: **Test circuit when noise is injected into the PI controller.**

signal to the MOSFET input. However, for the probe laser, a home-made circuit (Fig.5-7) is necessary to get the fast feedback to work. Below are the results of the tuning of the probe laser. As shown in Fig. 5-7, the circuit include a derivator and two phase compensators. The first phase compensator (R_1 and C_4) is to prevent the phase slip within 100-500kHz. This phase slip is typically caused due to the limited bandwidth of the electronics. The second phase compensator (R_5 and C_5) is to push the phase slip $1MHz$ to higher frequency. This phase slip is limited by the diode itself and the improvement from the phase compensator is very limited. The derivator is to suppress the gain when the significant phase slip happens. The gain with this circuit is plotted in Fig. 5-8.

To generate the error signal, we use the home-built electronics (Fig. 5-9) for the probe laser. For the control laser, the electronics is provided by Toptica.

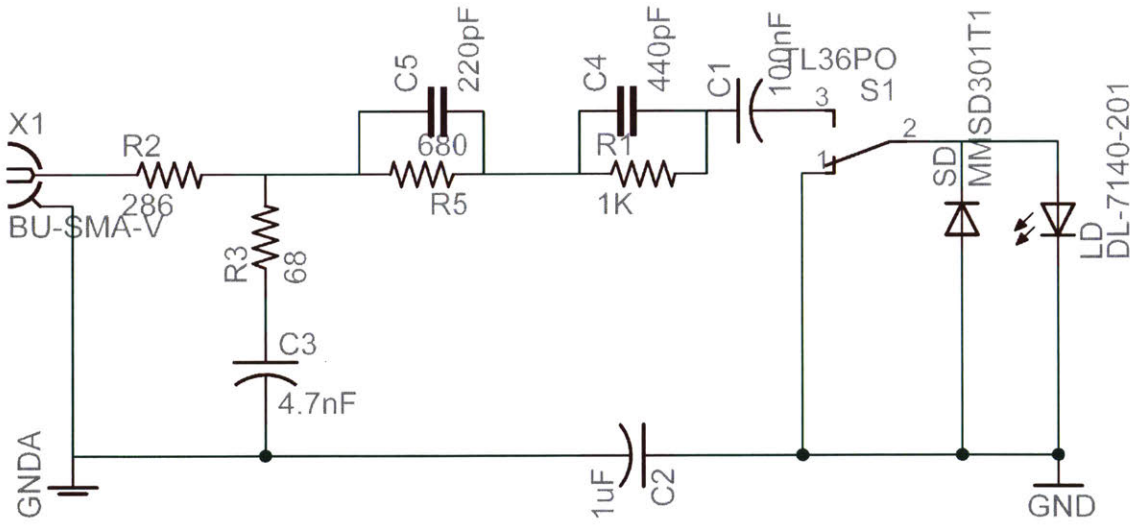

Figure 5-7: **Fast feedback to the laser diode (LD) of the probe laser.**

5.1.4 Estimation of laser linewidths

A standard method to measure laser linewidth is to beat the laser with another laser which has a narrower linewidth or with the light from the same laser but delayed more than the coherence time. Here, for convenience, we use the error signal of the lase lock

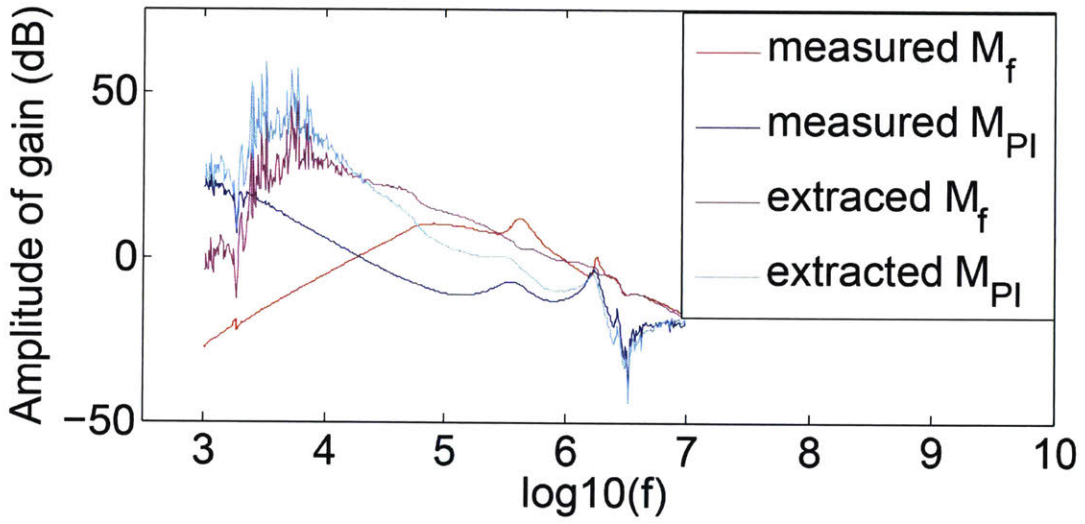

(a) Amplitude of the gain.

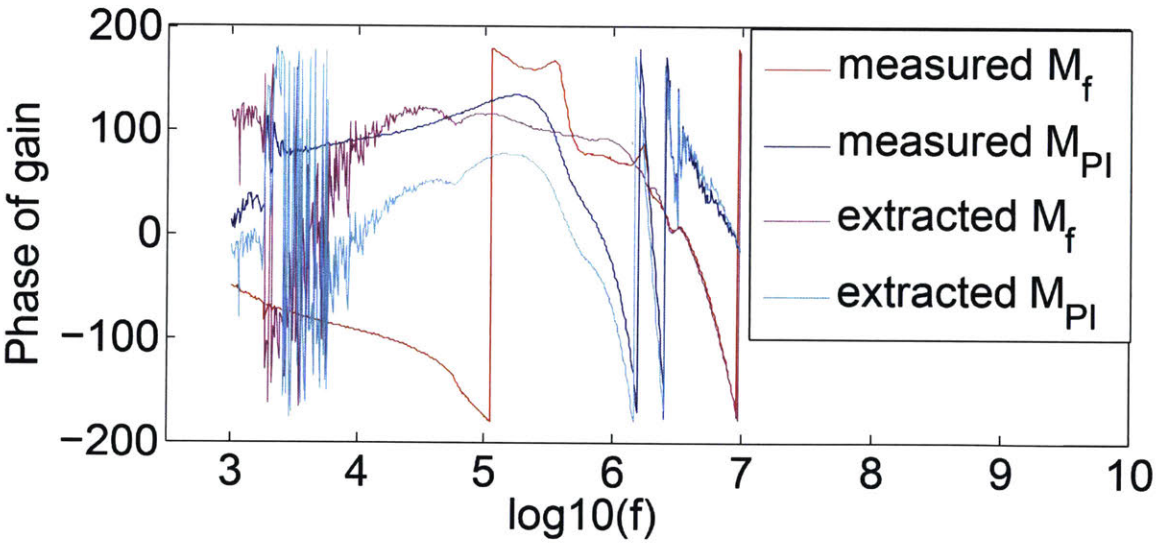

(b) Phase of the gain.

Figure 5-8: **Gain of the probe laser locking system.**

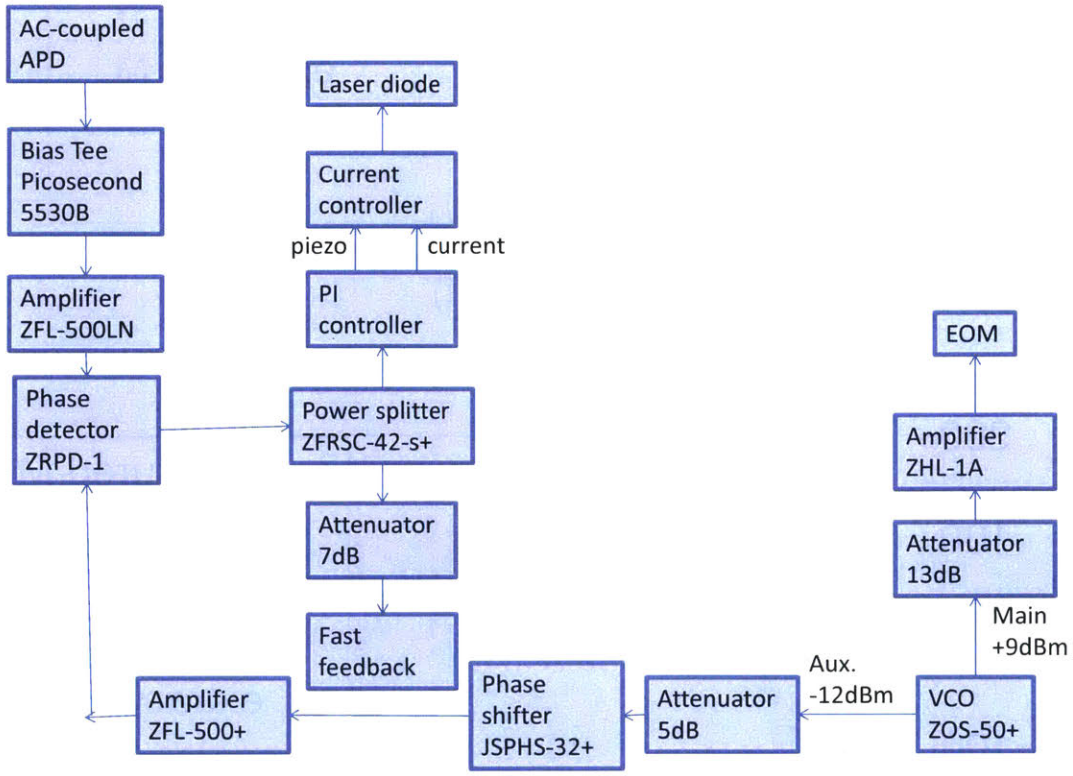

Figure 5-9: **Pound-Drever-Hall error signal generator for the probe laser.**

to estimate the laser linewidth. For the probe laser, we measure the open loop peak-to-peak value of the error signal $V_{pp} = 390$ mV. The rms value of the error signal for the closed loop is $V_{rms} = 47$ mV. The slope of the error signal is $D \equiv \frac{\epsilon}{\delta f} = -\frac{2V_{pp}}{\delta\nu}$ [66]. ϵ denotes the amplitude of the error signal, δf the deviation of the laser frequency from the locking point and $\delta\nu$ the linewidth of the transfer cavity. Using the finesse from Sec. 5.1.2, $\delta\nu = \frac{\delta_{FSR}}{\mathcal{F}} = \frac{2.672\,GHz}{6.8\times10^3} = 3.9\times10^2\,kHz$. The rms frequency deviation can be thus calculated $\Delta_{rms} = V_{rms}/D$. Usually, the laser linewidth is dominated by environmental noise due to acoustic vibrations and temperature variations, resulting in a Gaussian noise spectrum. For Gaussian distribution, FWHM width is related to rms deviation by $\Delta_{FWHM} = 2\sqrt{2ln2}\Delta_{rms} \simeq 60\,kHz$. Similarly, FWHM width of the 958nm light is estimated to be $130\,kHz$. The frequency doubling is expected to double the linewidth and therefore out estimated control laser linewdith is $260\,kHz$. All the laser linewidth measurements are taken with the transfer cavity locked to the reference laser.

Besides the instantaneous linewidth, there is a separate issue of long term drift. Even when the transfer cavity is locked to the reference laser, the frequency of the control laser can still drift at a rate of 10kHz/min, resulting probably from the barometric pressure change. We usually manually correct the frequency every ~20min.

5.2 Optical beams into the vacuum chamber

5.2.1 The crossed dipole trap

A crossed optical dipole trap is produced by a Nd:YAG laser operating at 1064 nm.

In the experiments in Chap. 6, the trap is formed by two orthogonally polarized beams with waists $w_t = 50\mu m$ intersecting at an angle of 32°. The beam is reflected after a half-wave plate (Fig. 5-10) and the power in the vacuum chamber is 5W. In order to modulate the dipole trap intensity at the MHz level, we make sure the beams have orthogonal polarizations so that no lattice is formed. Without a lattice, the trap frequency is at the kHz level, much lower than the modulation frequency. Unlike all

the other beams, the dipole trap beams do not go through an optical fiber. The laser head and the acousto-optic modulator (AOM) that controls the intensity and switch on/off the beam sits on the optical table where the vacuum chamber is located. The 0th order and the beam getting out of the chamber are absorbed by beam blocks.

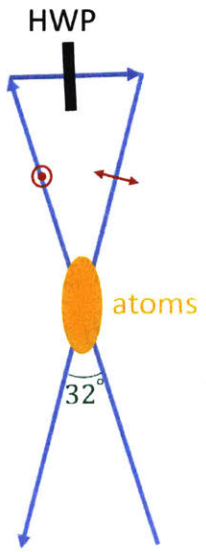

Figure 5-10: **Diple trap setup for the experiments in Chap. 6**. The blue arrows show the path of the dipole trap beams. The red marks indicate the polarization of the beams.

After those experiments, we start implementing Raman sideband cooling. A better control of magnetic fields is required. The counter-propagating orthogonal linear polarized dipole trap beams create a polarization gradient [67], which shifts different sublevels differently, resulting in an effective spatially varying magnetic field. In order to avoid such magnetic field, we switch to a new 25W trap laser. We split the power into two paths, each with its own AOM and opposite ($\pm$ 1st) order.

The trap frequencies are measured by parametric heating. The dipole trap intensity is modulated sinusoidally for 20ms with a depth of 20%, followed by a 10ms thermalization in the full dipole trap. Figure 5-11 shows the root-mean-square (rms) axial cloud size as a function of the modulation frequency after 1ms time of flight. The resulting frequencies are consistent with the measured beam power 8.9W per beam at full power and a beam waist of $44\mu m$, which predicts trap frequencies 1.8,

1.9, 0.52kHz.

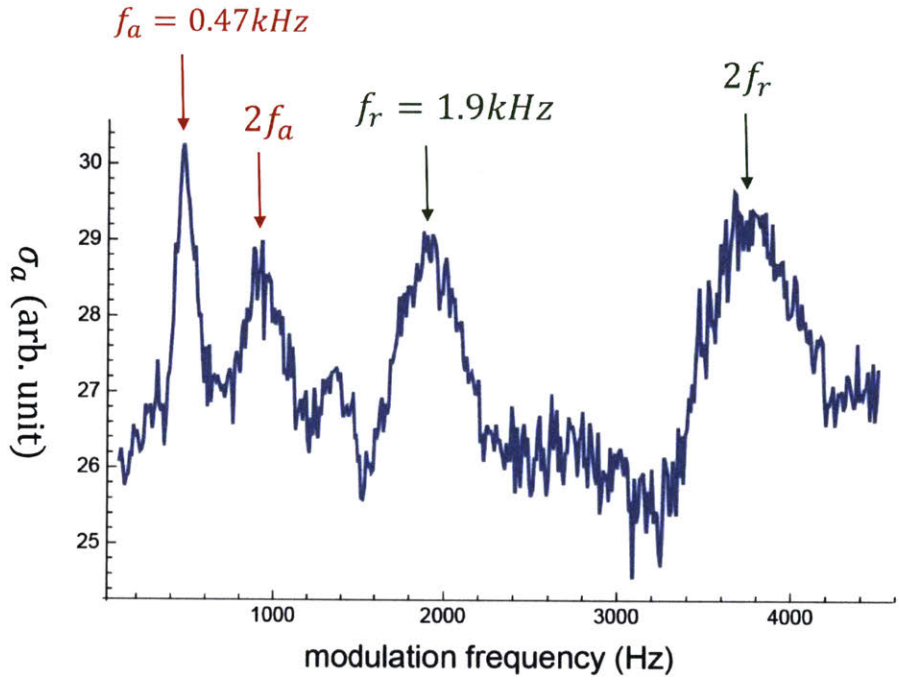

Figure 5-11: **Parametric heating measurement of the dipole trap frequency.** We attribute the four heating peaks to both the radial and axial trap frequencies. The two radial frequencies are very close. We do not expect to resolve them.

5.2.2 Probe and control

The probe beam is focused to a $1/e^2$ waist $w \approx 4.5\mu m$ by a confocal arrangement of achromatic doublet lenses with focal length 30 mm and diameter 6.25 mm (Edmund Optics, NT49-308). The same lenses focus the control beam as well. The coupling lens of the probe is A280TM-B (f=18.4mm) both before and after the chamber to SPCM. Initially, the probe is coupled to SPCM by polarization-maintaining single-mode fibers. Before the experiment in Chap. 7, we switch to non-polarization-maintaining single-mode fibers to achieve higher detection efficiency.

The control field co-propagates with the probe beam in the first experiment (Sec. 6.1). Later, in order to reduce the Doppler broadening, we switch to counter-propagating control. The $1/e^2$ waist is 12.5 μm. The transmitted control light is separated from the probe light by a combination of interference and absorption fil-

ters. The absorption filters are removed before the experiment in Chap. 7. Two interference filters (LL01-780-12.5 and LD01-785/10-12.5 from Semrock) are placed before each couplers to minimize the spurious photons and maximize the coupling efficiency.

Before the experiment in Chap. 7, we change the control beam waist to increase the Rabi frequency, or more specifically, the Autler-Townes (AT) splitting (see Sec. 5.5.1.4). The collimation lens is changed from c230TME-A (f=4.51mm) to A397TM-A (f=11mm), and the resulting beam waist at the atomic cloud is $7\mu m$. The control focus position can be optimized by maximizing AT splitting (see Sec. 4.1). All the beam waists are measured off-site.

The reduced beam waist allows us to have bigger Rabi frequency. However, the anti-trapping effect from the control beam is much more pronounced. We have significant loss of the atoms when the control beam is on. Therefore, we take data with 80% dipole trap duty cycle instead of 50% to minimize the loss of atoms.

We follow careful procedures to make sure the atomic cloud is placed at the probe focus because the Rayleigh range is very close to the length of the cloud. The alignment procedure is as follows:

1. We align the probe with the help of a guiding red beam. We overlap the reflection from the first lens in the chamber to the incoming guiding beam, and then overlap the probe with the guiding beam. Then the probe beam is never touched and everything else is aligned to it.

2. We move the MOT to roughly overlap with the probe by looking for the loss of atoms with a strong resonant probe. Once the loss is maximized, we mark the pixel on the absorption imaging CCD camera (see Sec. 5.5.2). We can move the dipole trap to this location and the loss of atoms signal can be easily found in the dipole trap as well.

3. We roughly find the probe focus in the compressed MOT (cMOT, see Sec. 5.4). The probe beam with an intensity an order of magnitude below saturation depopulates atoms from F=2 due to off-resonant excitations. We measure the

probe transmission as a function of time for each cMOT location and vary the cMOT location by the bias magnetic field along the probe propagation direction. The closer to the the focus, the smaller the probe, the higher the intensity and the faster the atoms are depumped.

4. In order to be more precise, we would like to find the probe focus with the dipole trap. At this point, we can either move the dipole trap or move the probe focus by moving its collimation lens. Moving the dipole trap requires a lot of realignment, but it works just as well with enough patience. Figure 5-13 shows an example of moving the collimation lens. With either the depumping rate or the initial transmission of the probe, we can locate the probe focus within $\sim 100\mu m$, consistent with the Rayleigh range as well as the length of the medium.

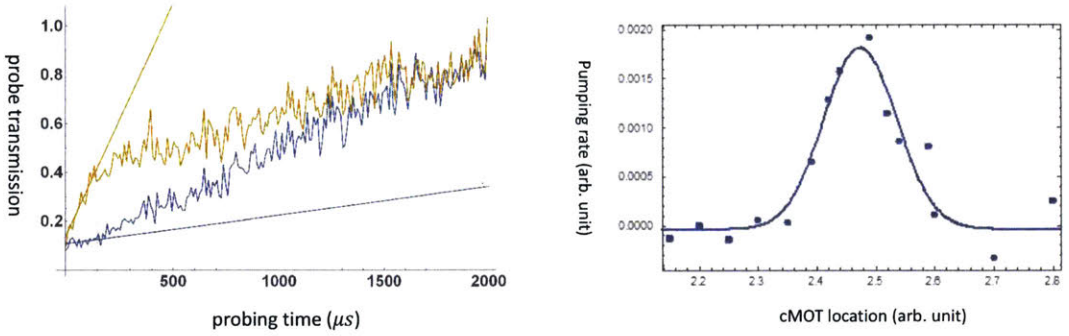

(a) Probe transmission vs probing time

(b) Fitted initial slope vs cMOT location

Figure 5-12: **Find the probe focus with cMOT.** We measure the linear dependence of the cMOT location on the bias magnetic field and move cMOT by the bias magnetic field. **(a)** We apply a linear fit to the initial probe transmission vs probing time. The fitting range is from the beginning to the grey vertical line. The yellow line has a bigger slope than the blue, and therefore its location is much closer to the probe focus. **(b)** The fitted slope is plotted as a function of the cMOT location. We apply a Gaussian fit, and the peak center is considered the probe focus.

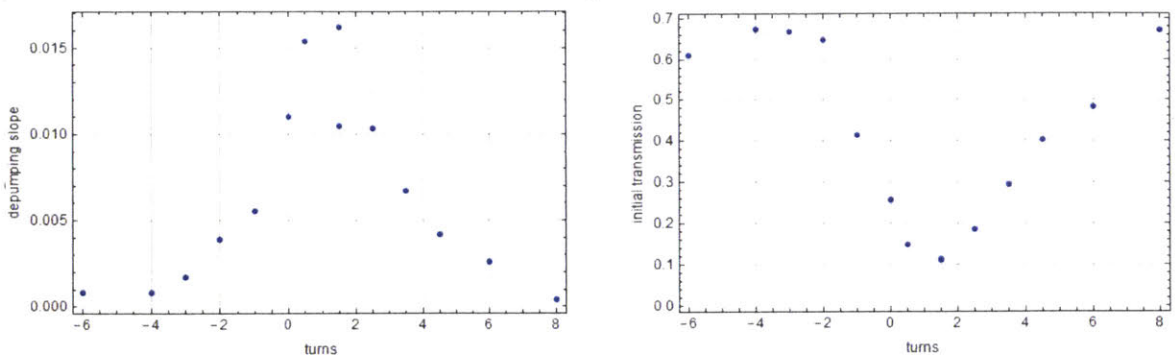

Figure 5-13: **The depumping slope (Left) defined in Fig. 5-12(a) and the initial transmission (Right) as function of the position of the z-axis translation mount (SM1Z from Thorlabs) of the coupling lens of the probe.**

5.2.3 MOT, repumper and beams for Raman sideband cooling

The magneto-optical trap (MOT) and repumper beams are the same as documented in [68]. Both are 1.5 inch diameter beams but are clipped by 1 inch diameter optics. The MOT beam is produced by an external cavity diode laser and a tapered amplifier (which steadily degrades over the past few years). The total power of the three MOT beams are $\sim 50mW$ for the experiments in Chaps. 7 and 8.

The MOT repumper couples $F = 1 \rightarrow 2$ transition. It is derived from a distributed feedback laser (Eagleyard). This laser also provides the optical pumping beam. The pumping beam passes a fiber electro-optic modulator (EOM from EO Space, PM-0K5-20-PFA-PFA-780), followed by an AOM. The EOM generates a sideband at $\sim$ 7GHz to address the $F = 2 \rightarrow 2$ transition. The pumping beam counter-propagates with the control beam and is σ^+-polarized.

After the experiments in Chap. 6, the MOT repumper laser is replaced with a distributed bragg reflector (DBR, from Photodigm) laser, which also provides the pumping beams for Raman sideband cooling. The pumping beam intersects the quantization axis (probe propagation direction) at an angle of $\sim 45°$. The σ^- light is eliminated to make $|F = 1, m_F = 1\rangle$ a dark state. The pumping beam addresses $F = 1 \rightarrow 0$ and $F = 2 \rightarrow 2$ transitions during RSC, and $F = 2 \rightarrow 1$ and $F = 1 \rightarrow 2$ during the optical pumping afterwards. See Sec. 5.4 for a typical experimental cycle.

The pumping beam is retro-reflected to minimize the momentum transfer to the atoms. Most other beams are aligned by scattering (loss) of atoms. However, the pumping beam can push the whole cloud by a distance on the order of the cloud size, which is a very clear signal for alignment. First, we block the reflection and maximize the mechanical displacement. Next, with the reflected beam, the cloud is ideally pushed back to the original place, after alignment optimization. Initially, this is not true, we then use this signal to adjust the location of the beam waist, leading to a balanced incoming and reflected beam.

The lattice for RSC is formed by a free-running DFB laser (from Sacher Lasertechnik) red detuned from D2 line by ~10GHz. After an AOM, the beam is fiber-coupled to the optical table where the vacuum chamber sits. It is then split into three paths with a total power of $\sim 20mW$, each with its own half-wave plate to tune the polarization. One of the beams is retro-reflected after a quarter-wave plate. For alignment convenience, it is chosen be a horizontal beam that goes through a different port from the pumping beam. The RSC lattice beams and the pumping beam share the same windows of the vacuum chamber as the MOT and repumper beams, and both have $\sim 1mm$ beam waist.

5.3 Raman sideband cooling

Raman sideband cooling is implemented after the experiments in Chap. 6 is finished. We follow the cooling setup in 3D lattice described in refs. [69, 70].

First, the transverse fields are zeroed by imaging with $F = 2 \rightarrow 2$ instead of the usual $F = 2 \rightarrow 3$ transition. The imaging beam is circularly polarized (Fig. 5-14). The Cartesian coordinates are defined as in Fig. 5-14. With a small B_z, if B_x and B_y are both zero, then the imaging beam will pump the atoms to the dark state and a minimal amount of atoms can be imaged. Therefore, B_x and B_y can be zeroed by minimizing the atom number in the absorption image. The smaller the B_z, the more sensitive the signal is. B_z is zeroed by maximizing the atom number with a small B_x or B_y. The repumper is on while imaging to keep the atoms in F=2. This technique

can be used to zero magnetic field during molasses as well.

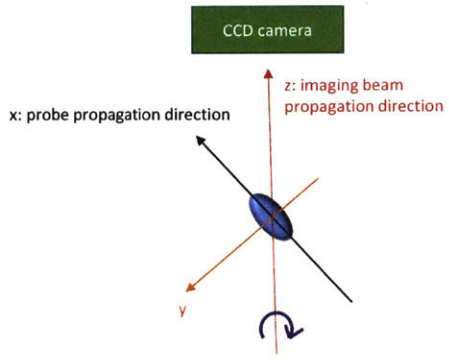

Figure 5-14: **The sketch of the Cartesian coordinates for the $F = 2 \rightarrow 2$ imaging discussion.** The purple arrow marks the polarization of the imaging beam.

Second, the pumping beam polarization is optimized by minimizing the loss of atoms, with a stronger pumping intensity than usual.

Third, we look for the cooling signal by scanning the magnetic field along the quantization axis (Fig. 5-15). A reduction and an increase of the cloud size can be seen around roughly opposite B fields, corresponding to cooling and heating. If the initial parameters are relatively far from optimum, usually at least the heating peak is visible.

Once the initial signal is found, further optimization can be achieved by tuning the polarization, frequency, intensity and its distribution among the three beams of the lattice light, the frequency and intensity of both transitions of the pumping beam, as well as the duration of the cooling.

Once RSC is optimized, we add the optical pumping stage to pump the atoms to $|F = 2, m_F = 2\rangle$. Since our goal is mostly to increase the optical depth, we usually fine tune RSC parameters to maximize OD in the end.

5.4 A typical experimental cycle

An ensemble of $\sim 10^6$ laser-cooled atoms is captured in a magneto-optical trap (MOT) every ~300 ms. The trapped cloud is compressed by the combined actions of increasing the magnetic-field gradient to 35 G/cm, red-detuning the MOT trapping

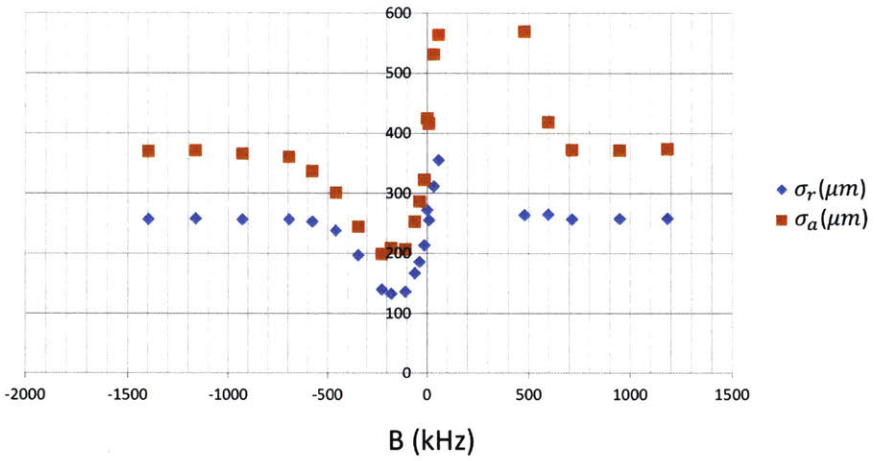

Figure 5-15: **RMS cloud sizes (characterizing the temperature) as a function of the magnetic field along the quantization axis.** The dipole trap is shut off right before we start to ramp down the lattice, which lasts for $100\mu s$. The rms cloud sizes are measured after 3ms time of flight with the CCD camera above the vacuum chamber. The blue and orange represent the radial and axial directions, respectively. Here, a cooling (heating) signal can be seen with a negative (positive) B field. The sign of B field is chosen arbitrarily.

frequency by ~30 MHz and reducing the MOT repumper intensity to ~10 $\mu W/cm^2$. The magnetic fields are then rapidly shut off, allowing for 10 ms of molasses cooling to a temperature of ~35 μK. After that, we change the magnetic field and the repumper frequency to do the Raman sideband cooling for $\sim 10ms$, resulting in a temperature of $\sim 20\mu K$ ($\sim 70\mu K$ without RSC) in the dipole trap. The quantization axis is along the probe propagation direction. RSC leaves the atoms in $|F = 1, m_F = 1\rangle$ sublevel. We ramp up the magnetic field to $\sim 3G$ and change the repumper frequency to pump the atoms to $|F = 2, m_F = 2\rangle$ sublevel. The same magnetic field is maintained during the probing, and optical pumping with much less intensity is on when dipole trap is on during the modulation. The dipole trap is always on except during probing. The crossed dipole trap holds up to 10^5 atoms at a peak density of $\sim 10^{12}$ atoms per cm^3. The radial and axial rms of the medium is ~ 10 and $\sim 35\mu m$, respectively, and the optical depth along the probe propagation direction is ~ 40.

5.5 Diagnostic tools

5.5.1 Spectra

5.5.1.1 Two-level fitting

We measure optical depth (OD) before each measurement everyday by fitting the measured photon counts per cycle as a function of the probe frequency. There are two methods of fitting we use routinely. The first one is to assume a two-level atom with a linewidth of $\Gamma = 6.1$MHz. This method has no other fitting parameters and results in a robust OD.

5.5.1.2 Optical pumping

In order to monitor and optimize the optical pumping, the second method we use is to simultaneously measure the spectra of both σ^+ and σ^- probe. We send in linear polarized probe light and separate the two polarization after the chamber. The model defines a quantity called pumping purity P. If there are N atoms in total, then PN atoms are in $m_F = 2$ sublevel while $(1-P)N$ atoms in $m_F = 1$ sublevel (Fig. 5-16). The contribution from all four transitions are included. We first fit the spectra of σ^+ probe. Then the fitting result, together with P and magnetic field B, is used to fit the σ^- spectra. We quote the OD from $m_F = 2$ atoms only as our final result. Usually, $\sim 90\%$ pumping purity is achieved. See Fig. 5-17 for some examples of the fitting.

If the purity is low, the optical pumping can be improved by optimizing the power and frequency of $F = 1 \rightarrow 2$ and $F = 2 \rightarrow 1$ pumping beams. Although usually not necessary, we can optimize the pumping further by adjusting the polarization of the pumping beam. A better signal to look at while adjusting the polarization is the loss of atoms. We increase the pumping intensity and duration so that we lose about half the atoms from the absorption imaging, and systematically change the polarization of the pumping beam until the loss is minimized. Last, we make sure all unwanted beams are not only turned off but also detuned properly during the optical pumping stage.

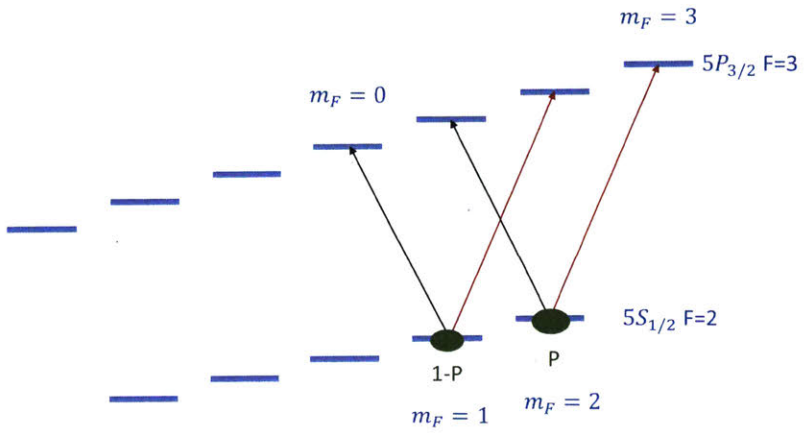

Figure 5-16: **The transitions included in the optical pumping purity fitting.**

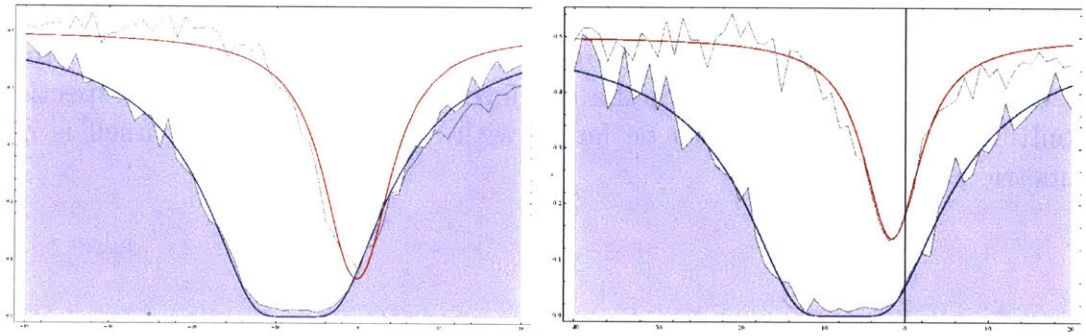

(a) Pumping purity ~0.5

(b) Pumping purity ~0.9

Figure 5-17: **Examples of pumping purity fitting.** Linear probe light is sent to the medium. σ^+ and σ^- are separately detected.

5.5.1.3 Multi-mode vs single-mode fibers

We use single-mode fibers (SMF) to couple the probe light to SPCM, because our dominant background detection is the fluorescence of 479nm control light at 780nm. This background is huge and hard to filter if multi-mode fibers (MMF) are used. Even with SMF, this is still the biggest source of spurious photons.

However, After the experiments in Chap. 6, we realize that OD measured with SMF is systematically larger than with MMF (Fig. 5-18). We attribute this to the dispersive medium off resonance, which can focus, defocus or refract the beam. After that, the beam is poorly coupled to SMF, resulting in lower counts off resonantly. This problem is more severe for larger OD. Since then, we always measure OD with MMF, and the fiber coupling is optimized and maintained with extreme care. Data are still taken with SMF to minimize the spurious photons.

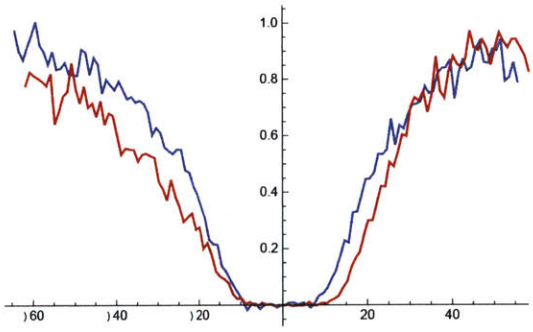

Figure 5-18: **Spectra taken with a single-mode fiber (red) and a multi-mode fiber (blue).** The fitted OD with the two-level model are 58 and 40, respectively. Not only the fitted OD tends to be larger with SMF, the spectrum itself is often asymmetric as well.

5.5.1.4 EIT spectra

We can take EIT spectra with control beam on, which helps us monitor and optimize the Rydberg-ground state decoherence. The most common reason for a larger than usual decoherence is the poor overlap of the probe and control beam, although other possible causes include stay electric field, poor control or probe locking, poor optical pumping, etc.

Operating at largest control intensity and $OD \sim 1$, we can measure the Autler-Townes (AT) splitting. We align the control beam by maximizing the splitting. We monitor the control intensity by a photodiode collecting light from the back side of a mirror very close to the vacuum chamber. The calibration of the photodiode reading vs the control Rabi frequency is done daily by fitting the AT splitting. While taking data, the photodiode reading is maintained manually to keep the control Rabi frequency constant throughout the measurement.

5.5.2 Absorption imaging

We have a permanent absorption imaging setup above the vacuum chamber, documented in Ref. [68]. The usages of the absorption imaging are listed below:

1. Measure the atom number. E.g. if OD is low, by measuring the atom number in MOT, compressed MOT and dipole trap, we can figure out which stage needs to be optimized.

2. Measure the size of the cloud and temperature by time-of-flight. This is the essential tool for RSC optimization.

3. Mark the locations. We keep track of the probe and cloud location with the pixel number of the CCD camera. Once the probe focus is found, everyday we make sure the atomic cloud is put at the same pixel.

We also set up temporary absorption imaging from the side windows. Two notable usages are:

1. Align the dipole trap. We first image the cloud from the dipole trap port and mark the pixel. Then we remove the imaging, set up the dipole trap beam to go along the same path and hit the same pixel. After that, it is usually very close to have an initial loading signal.

2. Measure temperature along the direction that cannot be seen from the top camera for the initial RSC optimization.

5.5.3 EIT resonance and slow-light group delay measurements

For the experiments operating at one-photon detuning $\Delta = 0$, the EIT resonance is unambiguous. We first find the probe resonance, without the control beam, by fitting the spectra with the two-level model. With the probe frequency fixed, we can scan the control frequency with very fine steps and fit the peak with a Gaussian lineshape to determine the center frequency.

For the experiments with large Δ, the EIT resonance with Rydberg-ground state decoherence is not located at the peak transmission. To make sure our measurements are consistent, we use the nominal resonance. Namely, we find the probe and control resonance frequency as described in the previous paragraph. Then we change the frequency by the nominal amount and consider that the EIT resonance.

To make sure everything is consistent, we usually measure the slow-light group delay τ_d and compare with the theoretical value. The group delay is related to the group velocity v_g introduced in Sec. 4.3 through $\tau_d = \frac{L}{v_g}$, where L denotes the length of the medium. We also use delay as a convenient way to monitor OD while taking data. Our standard OD measurements from the spectra require switching fibers from single-mode to multi-mode, and the delay measurements save us from this hassle. Two pulse shape measurements are done back to back with a $\sim 2\mu s$ Guassian probe pulse with and without the atoms, respectively. The delay is determined by maximizing the convolution of the two detected pulses.

5.6 Photon detection

Photons are fiber-coupled to the single photon counting modules (SPCM). We use AQRH series from Excelitas and their predecessors AQR series from Perkin Elmer. The correlation functions are the most important detections in our experiments and many other photonic systems [71–76]. Since vacuum has no dispersion, any amplitude and phase features formed inside the nonlinear medium are preserved outside, and can

be detected in the form of photon number and phase correlations. In order to obtain the arrival time of the photons precisely for the measurements of correlation functions, the counts (TTL pulses) are read by a 4-channel high resolution timing module (HRMTime from Sensl). For real time monitoring and other diagnostic purposes, the outputs of SPCM are also split to a 8-channel counter (PCI-6602 from National Instruments). We gated SPCM on during the dark of the dipole trap modulation. The AQR series output a TTL pulse the moment they are gated on. The timing of this pulse is used as time zero for that particular gate and channel. However, AQRH series do not always have such TTL pulse. Therefore, we mix the output of SPCM-AQRH with a signal that contains TTL pulses just before each gate as the indicator of the start of a new gate. All the splitting and combining of the counts are done with power splitter/combiner ZFRSC-42-S+ from Mini-Circuits. Small mismatches of the timing between different channels are corrected in the data analysis (Fig. 5-19).

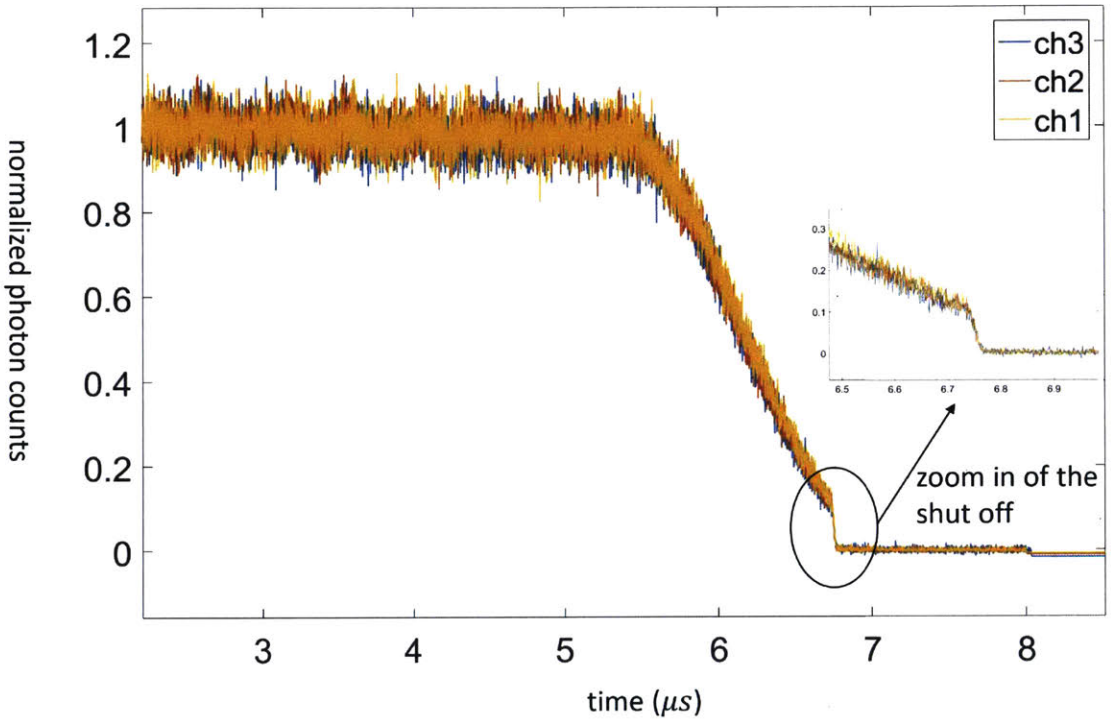

Figure 5-19: **A sharp edge of the pulse is used to synchronize all the channels.** I first subtract the noise (mean value between 7 and 7.5μs) from all the pulses and then normalize them (by the mean value between 3 and 5 μs) for comparison. With the abrupt shut off, the channels can be synchronized within a couple of nanoseconds, which is an order of magnitude smaller than our typical bin size.

Chapter 6

Single-photon nonlinearity

The realization of strong nonlinear interactions between individual light quanta (photons) is a long-standing goal in optical science and engineering, being of both fundamental and technological significance. In conventional optical materials, the nonlinearity at light powers corresponding to single photons is negligibly weak. Here we demonstrate a medium that is nonlinear at the level of individual quanta. In the dissipative regime, it exhibits strong absorption of photon pairs while remaining transparent to single photons. In the dispersive regime, the photon pairs acquire a conditional phase shift exceeding one radian, resulting in polarization entanglement.

The quantum nonlinearity can be viewed as a photon-photon blockade mechanism that prevents the transmission of any multiphoton state. It arises from the Rydberg excitation blockade, which precludes the simultaneous excitation of two Rydberg atoms that are separated by less than a blockade radius. During the optical excitation under EIT conditions, an incident single photon is converted into a Rydberg polariton inside the medium. However, owing to the Rydberg blockade, a second polariton cannot travel within a blockade radius from the first one, and EIT is destroyed. Accordingly, if the second photon approaches the single Rydberg polariton, it will be significantly attenuated in the dissipative regime, or acquire an additional phase in the dispersive regime, provided that the optical depth per blockade radius exceeds unity and the system is effectively one-dimensional.

6.1 The dissipative regime

6.1.1 Experimental setup

We demonstrate single-photon nonlinearity first in the dissipative regime $\Delta = 0$ and then in the dispersive regime $\Delta \gg \Gamma$. In the first experiment (dissipative regime), the probing is done after the dipole trap is shut off for 100μs. The resonant optical depth (OD) is 50. The probe and control co-propagate. The output of the probe is split by a 50:50 beamsplitter to two detectors for coincidence measurements.

The ^{87}Rb atoms are optically pumped into the hyperfine (F) and magnetic (m_F) sublevel $|g\rangle = |5S_{1/2}, F = 2, m_F = 2\rangle$ in the presence of a 3.6G magnetic field along the probe propagation direction. The probe beam on $|g\rangle \rightarrow |e\rangle = |5P_{3/2}, F = 3, m_F = 3\rangle$ transition and the control beam on the $|e\rangle \rightarrow |r\rangle = |nS_{1/2}, J = 1/2, m_J = 1/2\rangle$ transition are oppositely circularly polarized. See Fig. 6-1 for the energy diagram.

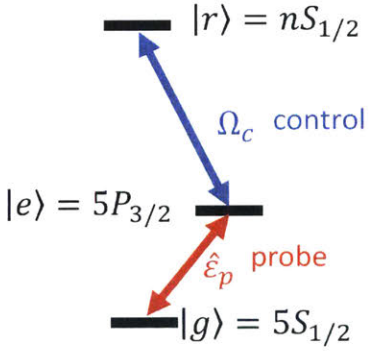

Figure 6-1: **The energy diagram.**

6.1.2 Single-photon nonlinearity: photon anti-bunching

Probe transmission spectra are presented in Fig. 6-2 for large optical depth OD=40 and the control laser tuned to the Rydberg state $|100S_{1/2}\rangle$. At very low incident photon rates $R_i \leq 1\mu s^{-1}$, the spectrum displays an EIT transparency window with 60% transmission. The transmission is mainly limited by the finite EIT decoherence rate γ_{gr}, which for our system is dominated by Doppler broadening and laser linewidth. The extraordinary nonlinearity of the Rydberg EIT medium becomes apparent as the

incident photon rate is increased: the probe beam is already strongly attenuated at a photon rate of $R_i \approx 4\mu s^{-1}$.

To demonstrate that we are operating in a quantum nonlinear regime, we show in Fig. 6-3 the correlation function $g^{(2)}(\tau)$ of the transmitted probe light, measured at $R_i = 1.2\mu s^{-1}$. For the most strongly interacting state we tried $|100S_{1/2}\rangle$ with $r_b = 13\mu m \approx 5L_a \approx 2.9w$, we observe strong anti-bunching with $g^{(2)}(0) = 0.13(2)$, largely limited by background light. The resonant attenuation length $L_a = L/OD$, where OD and L denote the resonant optical depth and the length of the medium, respectively. The resonant blockade radius is defined as $r_b = (\frac{2\Gamma C_6}{\Omega_c^2})^{1/6}$, where Γ is the decay rate of state $|e\rangle$, Rydberg-Rydberg interaction of strength C_6 between atoms at a distance r is $V(r) = \frac{C_6}{r^6}$, $C_6 = 56THz/(\mu m)^6$ for $|100S_{1/2}\rangle$, and Ω_c is the control field Rabi frequency. The probe beam is focused to a Gaussian waist of $w = 4.5\mu m < r_b$. Subtraction of the independently measured background coincidence counts yields a corrected $g_c^{(2)}(0) = 0.04(3)$. These observations are in sharp contrast to EIT transmission via a less strongly interacting Rydberg state $|46S_{1/2}\rangle$ with $r_b = 3\mu m$, where the photon statistics of the transmitted light are similar to those of the incident coherent state (see Fig. 6-3 inset).

We note that for $|100S_{1/2}\rangle$ the photons are anti-bunched over a length scale $v_g\tau \approx 50\mu m$ that exceeds the blockade radius (see top axis of Fig. 6-3). The slow-light group delay τ_d through the atomic medium is measured independently in a pulsed experiment (Sec. 5.5.3), and used to calculate the corresponding minimum group velocity $v_g = \frac{\sqrt{2\pi}\sigma_a}{\tau_d}$, where σ_a denotes the axial rms length of the atomic cloud.

Close examination (Fig. 6-5(b)) reveals that the correlation time is of the same order as, and scales inversely proportionally with, the spectral width $B = \frac{\Omega_c^2}{2\sqrt{2OD\Gamma}}$ (Eq. 4.9) of the EIT transparency window. This observation suggests that propagation effects play an important role in establishing the $g^{(2)}$ correlation time τ_c in a medium of large optical depth. We observe that, under appropriate conditions, two-photon events are suppressed inside the medium on a length scale that approaches the size $\sigma_a \approx 35\mu m$ of the entire atomic ensemble, and on a timescale that approaches the intrinsic coherence time $\gamma_{gr}^{-1} = 500$ns. To summarize, the width of the anti-bunching

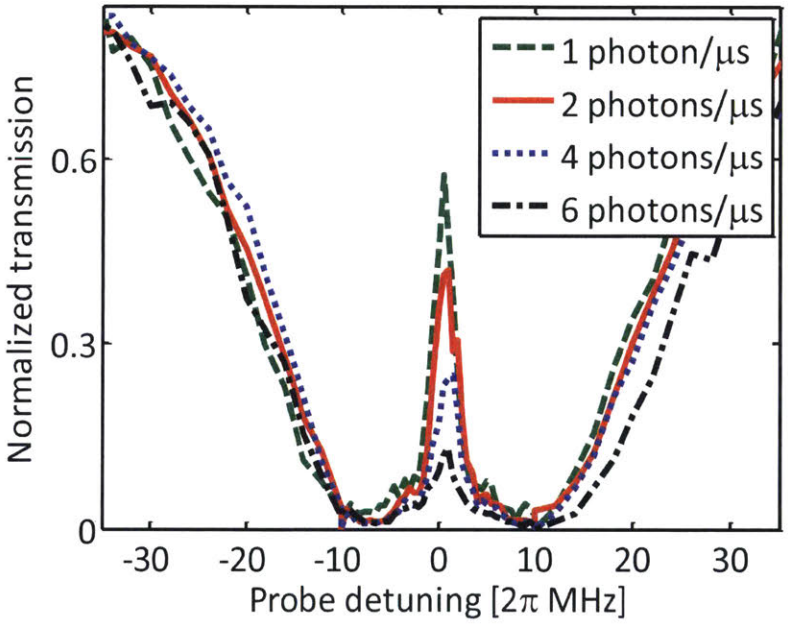

Figure 6-2: **Transmission vs probe detuning at various incoming photon rate** $R_i = 1, 2, 4, 6\mu s^{-1}$ (dashed green, solid red, dotted blue and dot-dashed black, respectively) for $|100S_{1/2}\rangle$, EIT (full) linewidth $\gamma_{EIT} = \frac{\Omega_c^2}{\Gamma} = 2\pi \times 23$MHz, and optical depth OD=40, and measured group delay $\tau_d = 250$ns. The system is strongly nonlinear at a power as low as 0.25pW.

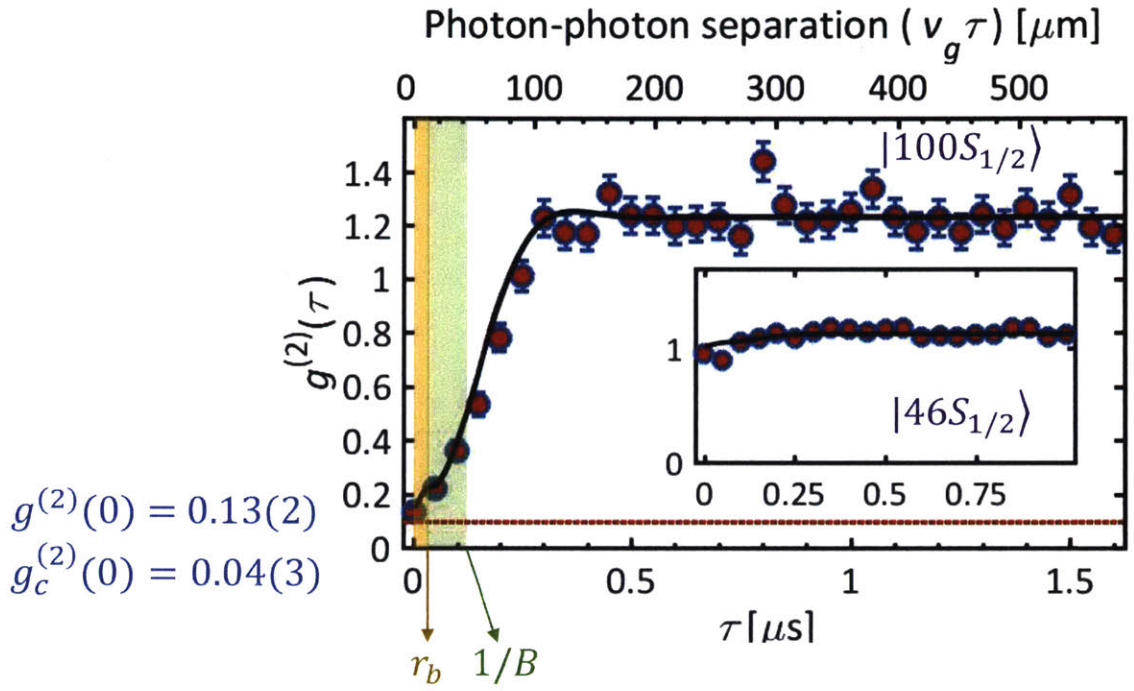

Figure 6-3: **Single-photon nonlinearity for $|100S_{1/2}\rangle$, EIT linewidth $\gamma_{EIT} = 2\pi \times 23$MHz and optical depth OD=40.** Data pioints show photon-photon correlation function $g^{(2)}(\tau)$ at EIT resonance with $R_i = 1.2\mu s^{-1}$. The top axis shows the spatial sparation $v_g\tau$ of polaritons with $v_g \approx 400m/s$. Spurious detection events set a lower bound on $g^{(2)}$ of 0.09(3) (red dotted line). Inset, $g^{(2)}$ for the less strongly interacting state $|46S_{1/2}\rangle$ with similar parameters. The solid lines in the main panel and inset are theoretical calculations as described in Secs. 6.3.1 and 6.3.2. Values $g^{(2)} > 1$ are attributed to classical fluctuations (see Fig. 6-8).

feature is determined by a competition between the blockade radius, EIT bandwidth and the coherence time. As OD increases, the blockade radius (in time scaled by v_g) grows linearly with OD, while the EIT bandwidth (converted to time) grows as $\sqrt{OD}$. At sufficient large OD, the blockade radius can go beyond the EIT bandwidth, and consequently τ_c could be limited by the blockade radius, coherence time permitting.

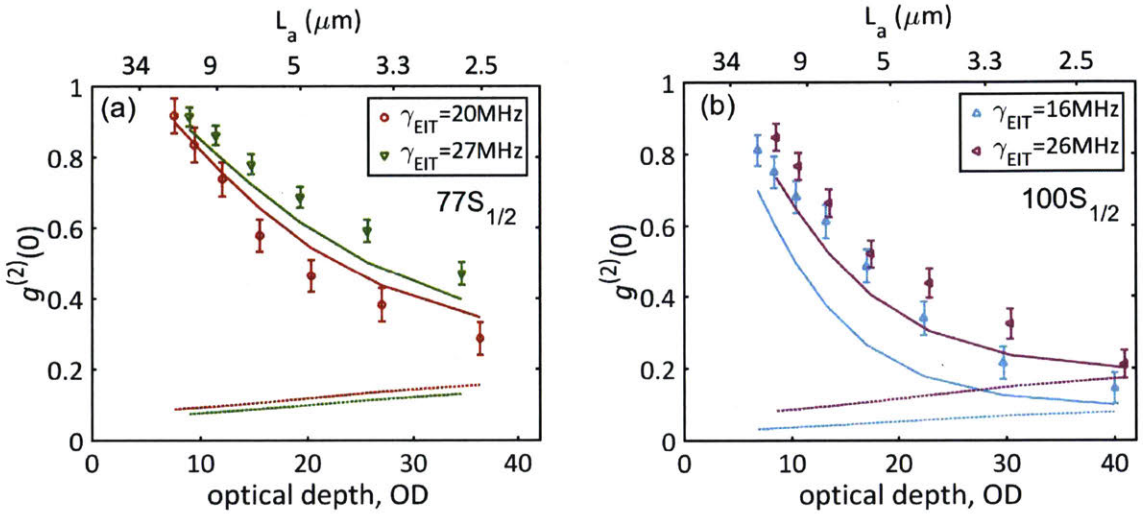

Figure 6-4: **Equal-time photonphoton correlation $g^{(2)}(0)$ as a function of OD for $|77S_{1/2}\rangle$ (a) and $|100S_{1/2}\rangle$ (b), for a set of single-atom EIT linewidths (circles, down-triangles, up-triangles, left-triangles) $= 2\pi \times (20, 27, 16, 26)$ MHz.** Solid lines are numerical solutions for a probe beam waist $w = 6\mu m$, including detection noise (dotted lines). See Sec. 6.3.4 for an analytical solution of these $g^{(2)}$ features.

Figure 6-4 shows that $g^{(2)}(0)$ improves with the principal quantum number n of the Rydberg state, resulting in a more than tenfold suppression of the two-photon transmission, limited by independently measured background light on the photon detectors (dotted lines). The blockade radius increases with n as $r_b \propto n^{11/6}$. Hence, larger n renders larger $OD_b = r_b/L_a$ and more strict one-dimensional condition $r_b > w$, resulting in a steep dependence of $g^{(2)}(0)$ upon n.

We characterize the widths of the $g^{(2)}$ anti-bunching feature by the half-width-at-half-maximum (HWHM) τ_c of the dip and plot them in Fig. 6-5. Although the Rydberg blockade only takes place within the blockade radius r_b, the finite EIT bandwidth does not allow sharp features in real space to propagate through the medium.

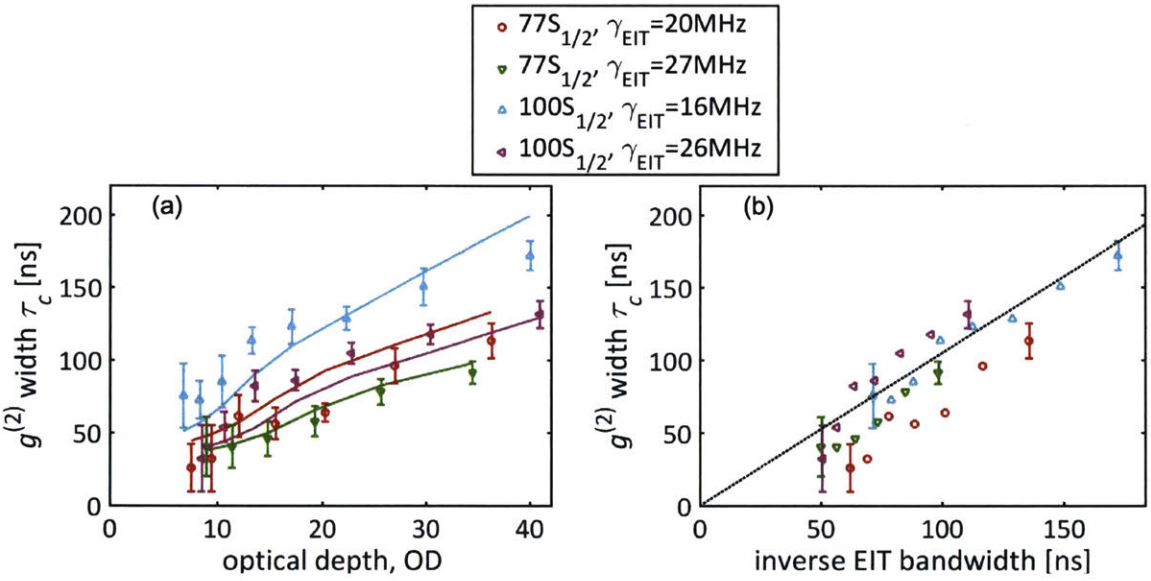

Figure 6-5: **Dependence of the $g^{(2)}$ widths τ_c on EIT parameters.** **(a)**, τ_c as a function of OD for $|77S_{1/2}\rangle$ and $|100S_{1/2}\rangle$, for a set of single-atom EIT linewidths (circles, down-triangles, up-triangles, left-triangles) $= 2\pi \times (20, 27, 16, 26)$ MHz. **(b)**, τ_c of the anti-bunching feature in $g^{(2)}(\tau)$ as a function of EIT transparency width $B = \frac{\Omega_c^2}{2\sqrt{2OD}\Gamma}$. Solid lines in (a) are numerical solutions for a probe beam waist $w = 6\mu m$. The black dashed line in (b) is $1.05/B$. See Sec. 6.3.4 for an analytical solution of these $g^{(2)}$ features.

To be specific, a sharp feature in the relative coordinate corresponds to a wide range of relative momentum. Namely, the frequency difference of the two photons is large, and there is no way to fit both photons into the EIT transparency width. Therefore, the blockade acts like a loss and the EIT bandwidth plays the role of diffusion–smoothening the anti-bunching feature. The propagation of the two-photon amplitude is governed by a diffusion equation (see Sec. 6.3.4).

6.1.3 Saturation of the output photons

To investigate the transmission characteristics of multiple photons through the medium, we plot in Fig. 6-6 the output photon rate R_o, scaled by the EIT transmission measured at low probe power, as a function of incident photon rate R_i. At first, R_o increases linearly with R_i as expected, but then saturates abruptly to a constant value of $R_o = 1.3(3)\mu s^{-1}$. Note that these observations deviate from the simplistic model of a multiphoton absorber that transmits only the one-photon component from the incoming coherent state (black dashed line in Fig. 6-6). At the same time, the observed output flux corresponds to less than one photon in the medium ($R_o^{-1} > \tau_d = 300\text{ns}$).

Recently, E. Zeuthen et al. [77] point out that there should be a bump in the saturation curve around the corner before the output rate settles to the saturated value. The simple physical picture is as follows: The scattered photon localizes the Rydberg polariton to within a blockade radius, which is too short (in real space) to fit into the EIT transparency window (in Fourier space). Therefore, the transmission is reduced by scattering other photons, and the output rate is slightly higher (the bump) before the medium is fully saturated. Unfortunately, the existing data are not sufficient to test this theory, due to the complications in the high rate regime (see insets of Fig. 6-6).

Figure 6-7 shows the saturated output rate versus the ratio r_b/w of blockade radius and probe beam waist for a wide range of principal quantum numbers, control field intensities and optical depths. The approximate $R_o \propto (w/r_b)^2$ scaling, valid for $w \gtrsim r_b$, indicates that the saturated rate for intermediate to strong interactions, $r_b > L_a$, is largely determined by the transverse geometrical constraint, that is, by

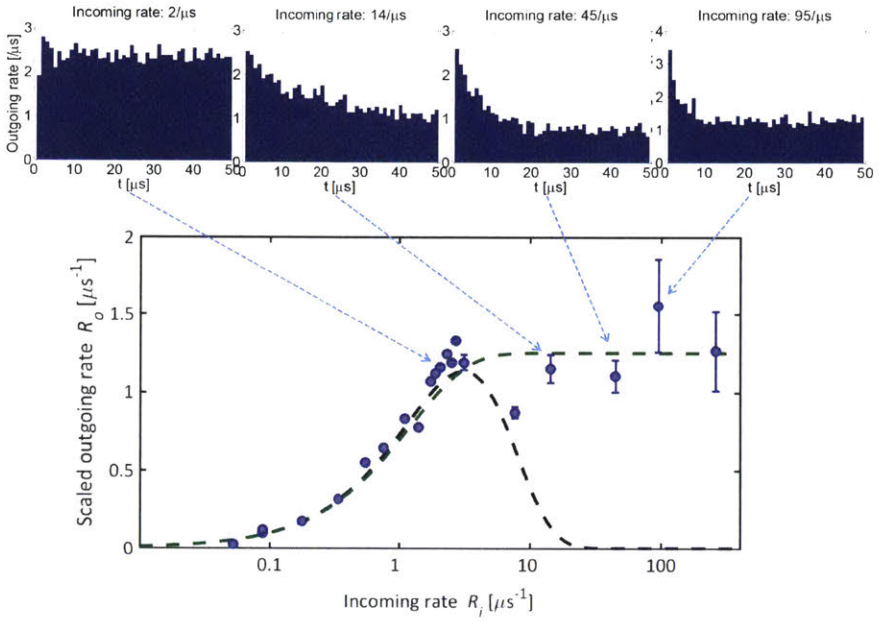

Figure 6-6: **Outgoing versus incoming photon rate** for $|100S_{1/2}\rangle$, $\gamma_{EIT} = 2\pi \times$ 15MHz, OD=26, and a measured width τ_c =130ns of the anti-bunching feature in $g^{(2)}(\tau)$. All output rates are scaled by the transmission of 50% at low photon rate due to linear absorption, and corrected for the finite detection-path efficiency. The dashed black curve outlines the expected rate if all multi-photon events in a time range τ =320ns are fully blocked, while the green dashed curve assumes that all multiphoton states within τ =800ns are converted into an outgoing one-photon state. Although not noticeable at low photon rate $R_i \lesssim 2\mu s^{-1}$, at higher rate, there is a decay of the transparency over the measurement time, which is likely to be related to molecular resonances discussed in Sec. 6.1.4. In such cases, we fit an exponential decay to the transmission curve and obtain the initial instantaneous outgoing rate. Therefore, at very high rates, error bars are greatly increased.

the extent to which the Rydberg polaritons can propagate side by side through the medium.

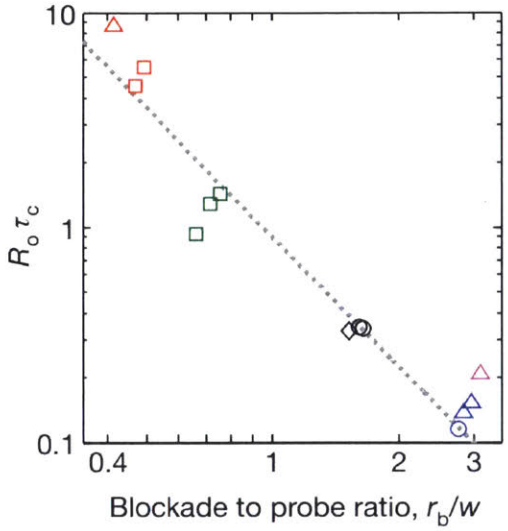

Figure 6-7: **Saturated rate of outgoing photons $R_o t_c$ per anti-bunching correlation time τ_c, scaled by the linear absorption, as a function of the ratio between the blockade radius r_b and the probe beam waist w.** The Rydberg states are $|100S_{1/2}\rangle$ (blue, $w = 4.5\mu m$, $OD_b \approx 8$; pink, $w = 4.5\mu m$, $OD_b \approx 4$), $|77S_{1/2}\rangle$ (black, $w = 4.5\mu m$, $OD_b \approx 3$), $|46S_{1/2}\rangle$ (green, $w = 4.5\mu m$, $OD_b \approx 0.7$; red, $w = 7\mu m$, $OD_b \approx 0.7$). τ_c is estimated using the single-atom EIT linewidths (squares, triangles, circles, diamonds)=$2\pi \times (6-16, 18-26, 29-36, 50)$ MHz, and varies from 60 to 330 ns. The dashed line corresponds to $0.9(w/r_b)^2$, indicating the expected scaling with transverse confinement for $w \gtrsim r_b$.

6.1.4 The super-Poissonian correlation on a longer time scale

At large atomic densities, the $g^{(2)}$ functions exhibit both a local super-Poissonian feature on a range of $\sim 20\mu s$ and a global positive offset of 0.08 from the expected value 1 at large times (Fig. 6-8). We attribute the local feature to the occasional population of metastable Rydberg levels not resonantly coupled by the control field to a fast decaying state. This process is relatively rare at the photon flux used in the $g^{(2)}$ measurements ($R_i < 2\mu s^{-1}$, where incoming and outcoming rates are compensated for detection losses). However, when it does occur, the medium becomes absorptive until the Rydberg atom has moved a distance larger than the blockade radius away from the probe beam area, or has decayed to a low-lying state. At high incoming

probe rate ($R_i \geq 5\mu s^{-1}$), it results in a strong attenuation of the transmission over the course of the experiment (Fig. 6-6 insets). As the probe power increases, the attenuation happens on a shorter timescale and settles to a lower transmission rate. For $R_i = 100\mu s^{-1}$, the cloud becomes totally opaque in $\sim 1\mu s$. If the control field is turned off for a moment, the transmission progressively returns to its initial value in $20\mu s$. The decay shows no dependence on static electric fields up to 10 V/cm, ruling out the presence of ions in the cloud. The global $g^{(2)}(\infty) = 1.08$ feature is attributed to slow drifts and classical fluctuations in our system. These include OD fluctuations, frequency drifts of the spectroscopic reference for the transfer cavity lock and alterations of the alignment, resulting in slow variations of the observed transmission on the order of 20%.

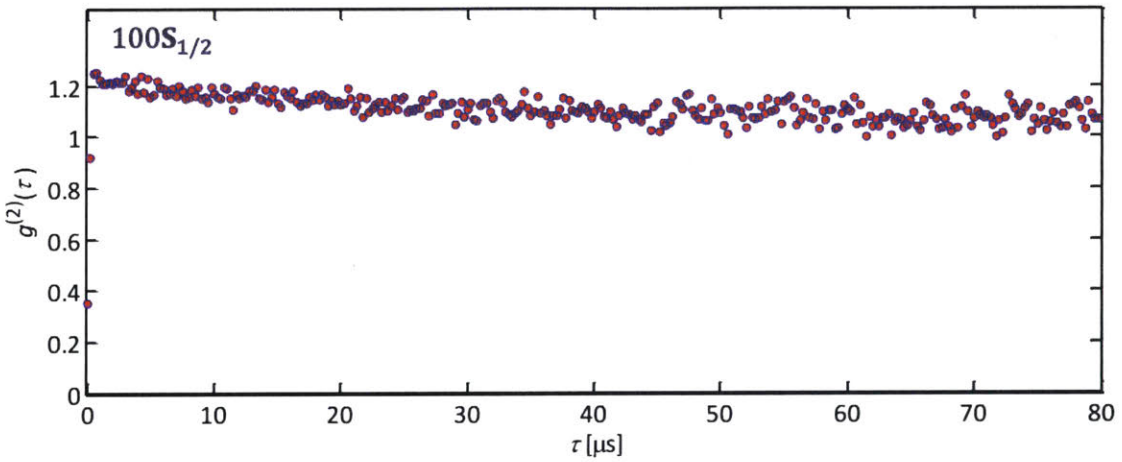

Figure 6-8: **Intensity correlation function** $g^{(2)}(\tau)$ up to τ=80 μs for $|r\rangle = 100S_{1/2}$. The first two data points are below 1. Outside the anti-bunching window, the light is super-Poissonian. We attribute this to the excitation of Rydberg atoms in the medium and, for very large τ, experimental drifts.

The exact mechanism of the creation of the contaminant Rydberg atoms has never been nailed down. One compelling hypothesis is the molecular resonances described in Ref. [78]. The driving laser field, on resonance with $100S + 100S$ dissociation limit, can resonantly excite unwanted Rydberg pairs, inside a shell around a specific R (Fig. 6-9). Inside the shell, the two excited Rydberg atoms are subjected to a mechanical force that can be either repulsive or attractive. In this particular scenario, the laser coupling to an attractive potential is negligible. For a repulsive force, the

pair of Rydberg atoms will separate into two atoms with a kinetic energy equal to the dissociation limit. An example is around $R \sim 7\mu m$, the excited pair state would split into a $99S$ and a $101S$ atom. In our experiment, a typical EIT (half) linewidth is $\frac{\Omega_c^2}{2\Gamma} \sim 8$MHz with $\Omega_c = 10$MHz. In Fig. 6-9, the excitation is assumed to have a half linewidth 10MHz and the corresponding shell has a full width $\sim 0.2\mu m$. Hence, the optical depth per shell is ~ 0.1–quite large!

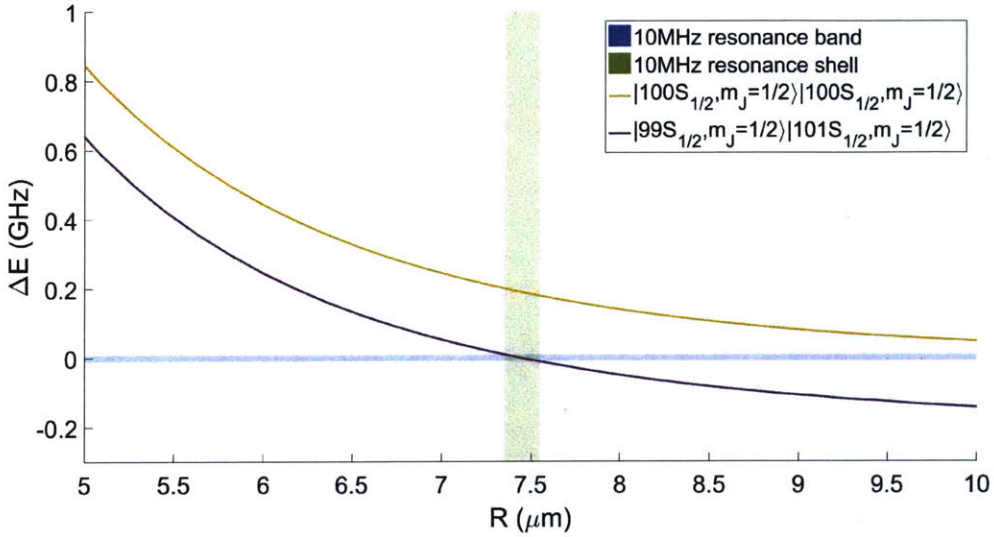

Figure 6-9: **Qualitative energy diagram of two pair states**, which are labeled by the double-atom states at the dissociation limit, $|100S_{1/2}, m_J = 1/2\rangle|100S_{1/2}, m_J = 1/2\rangle$ and $|99S_{1/2}, m_J = 1/2\rangle|101S_{1/2}, m_J = 1/2\rangle$. The energy of $|100S_{1/2}, m_J = 1/2\rangle|100S_{1/2}, m_J = 1/2\rangle$ at the dissociation limit is located at $\Delta E = 0$. The energy within the excitation linewidth of the driving fields is highlighted in blue, and the corresponding distance shell within which the pair state labeled as $|99S_{1/2}, m_J = 1/2\rangle|101S_{1/2}, m_J = 1/2\rangle$ can be resonantly excited is highlighted in green. With such small separation R as illustrated, densely packed pair states (not shown) are within the energy window. The exact energies can have kinks and other complicated structures, and need to be calculated with extreme care. See Appx. B for the calculation of the diagram.

For n=100, the kinetic energy is $\sim 10mK$ [78] and the corresponding velocity is $\sim 1\mu m/\mu s$. For a blockade radius $\sim 10\mu m$, such contaminant atoms will interact with the Rydberg polaritons for $\sim 10\mu s$ before they move away. Those interactions can significantly modify the transmission of the Rydberg polariton in a similar way as the interactions between Rydberg polaritons. However, such changes of the transmission

will not show up as anti-bunching, because the contaminant atoms are not coupled to the laser fields and will not be registered on the detectors. Instead, they appear to be variations of the linear transmission similar to classical intensity noise resulting in $g^{(2)} > 1$. The time scale for the changes of transmission to go away is the same as that for the contaminant atom to move out of the interaction range. Therefore, the super-Poisonian correlations we observe outside the anti-bunching window (Fig. 6-8) is likely to be related to these molecular resonances, on top of experimental drifts, which we do not expect to have a $\sim 10\mu s$ time scale.

6.2 The dispersive regime

6.2.1 Experimental setup

In the second experiment, the dipole trap is modulated with a 11μs period for 4ms (50% duty cycle), to increase the measurement time per MOT loading. The OD is reduced to 22 consequently. Additionally, to minimize the Doppler broadening, the probe and control counter-propagate.

To determine both the amplitude and the phase of the σ^+-polarized probe field, we send in a linearly polarized state, $|V\rangle = (|\sigma^+\rangle + |\sigma^-\rangle)/\sqrt{2}$, and the output is measured in different polarization bases (Fig. 6-10). The σ^+ and σ^- components of the incoming linearly polarized probe light respectively couple to the $|e\rangle = |5P_{3/2}, F = 3, m_F = 3\rangle$ and $|e'\rangle = |5P_{3/2}, F = 3, m_F = 1\rangle$ excited states. For our magnetic field of 3.6G, the Zeeman splitting between these levels is $2\pi \times 6.7$MHz, comparable to their inverse lifetime $\Gamma = 2\pi \times 6.1$MHz. The coupling dipole matrix element for the σ^+ transition is larger than for the σ^- transition by a factor of $\sqrt{15}$. The σ^- polarized control field couples the stretched state $|e\rangle$ to the Rydberg state with maximal projections of the nucleus spin (m_I) and total electronic angular momentum (m_J), $|r\rangle = |100S_{1/2}, m_I = 3/2, m_J = 1/2\rangle$. In addition, it couples $|e'\rangle$ to $|r'\rangle = |100S_{1/2}, m_I = -1/2, m_J = 1/2\rangle$ and $|r''\rangle = |100S_{1/2}, m_I = 1/2, m_J = -1/2\rangle$ with a $\sqrt{5}$ times weaker resonant Rabi frequency. The energies of the levels $|r\rangle$ and $|r'\rangle$ are equally shifted by the magnetic

field. Therefore, both $\sigma^+$and σ^- photons propagate under Rydberg EIT conditions. The combined effect of the Zeeman shift of the intermediate level and the reduced dipole coupling strongly suppresses the probability for σ^- photons to create or be affected by Rydberg blockade. As the σ^- probe photons interact only negligibly between themselves and weakly with σ^+ photons, they provide a reliable reference for measuring phase shifts of the σ^+ photons.

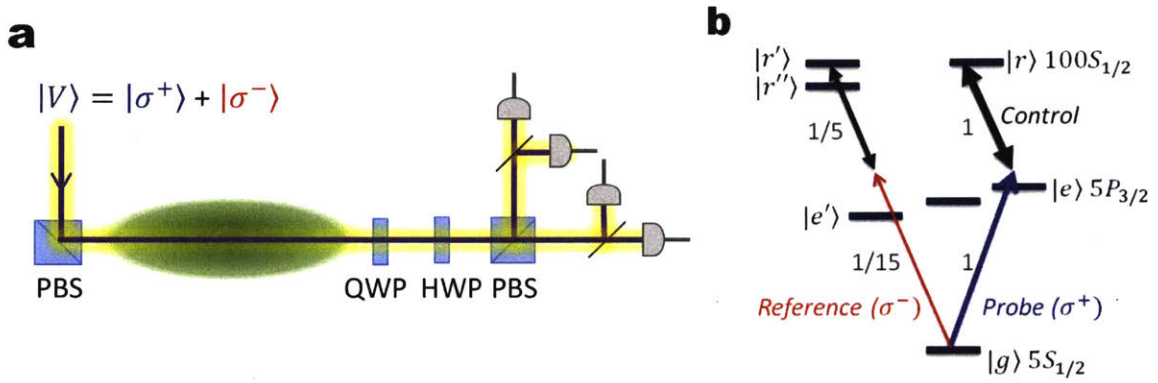

Figure 6-10: **The setup and atomic transitions for the quantum state tomography.** **(a)** The sketch of the experimental setup. **(b)** Schematic representation of the atomic transitions. The numbers next to the transitions are the squares of Clebsch-Gordan coefficients.

6.2.2 Quantum state tomography

To analyze the properties of photon pairs, we measure two-photon correlation functions, $g^{(2)}_{\alpha,\beta}$, in six polarization bases, {q, h}={$\pi/4$, $\pi/4$}, {0, 0}, {$\pi/8$, $\pi/8$}, {0, $\pi/16$}, {$\pi/8$, $\pi/16$} and {$\pi/8$, 0}, where q and h are the angles of the quarter- and half-wave plates, as shown in Fig. 6-11. The duration of the coincidence time bins, varying between 20 and 80 ns, is chosen to capture the temporal dynamics of the correlation functions with reasonable signal-to-noise ratio. For each (t_1,t_2) time bin, we numerically optimize a Hermitian, positive-semidefinite two-photon density matrix,

$\rho(t_1,t_2)$

$$\rho = \begin{pmatrix} \rho_{++,++} & \rho_{++,S} & \rho_{++,--} & 0 \\ \rho_{S,++} & \rho_{S,S} & \rho_{S,--} & 0 \\ \rho_{--,++} & \rho_{--,S} & \rho_{--,--} & 0 \\ 0 & 0 & 0 & \rho_{AA} \end{pmatrix}$$

and one-photon density matrix, $\rho^{(1)}(t)$. The two-qubit basis $\{|\sigma_1^+\sigma_2^+\rangle, |S\rangle, |\sigma_1^-\sigma_2^-\rangle, |A\rangle\}$, where $|S\rangle = (|\sigma_1^+\sigma_2^-\rangle + \sigma_1^-\sigma_2^+\rangle)/\sqrt{2}$ and $|A\rangle = (|\sigma_1^+\sigma_2^-\rangle - \sigma_1^-\sigma_2^+\rangle)/\sqrt{2}$. Because the two photons have the same frequency and spatial mode, there is no coherence between the 3×3 symmetric and 1×1 antisymmetric subspaces [79]. The optimization follows the maximum-likelihood estimate [80], where all coincidence measurements are considered.

To extract the nonlinear phase from $\rho(t_1,t_2)$, we rescale for the linear dispersion and loss effects by defining the interaction matrix $\tilde{\rho}_{i,j}(t_1,t_2) = \rho_{i,j}(t_1,t_2)/[\rho^{(1)}(t_1) \otimes \rho^{(1)}(t_2)]_{i,j}$ in the basis $\{|\sigma_1^+\sigma_2^+\rangle, |\sigma_1^+\sigma_2^-\rangle, |\sigma_1^-\sigma_2^+\rangle, |\sigma_1^-\sigma_2^-\rangle\}$. The interaction matrix generalizes the standard $g^{(2)}_{\alpha,\beta}$ definition to account for nonlinear phases and decoherence, and all its elements are equal to 1 in the absence of nonlinearity.

The intensity correlation function of σ^+ photons and the nonlinear phase can be extracted from the interaction matrix $\tilde{\rho}$ as $g^{(2)}_{++} = \tilde{\rho}_{++,++}$ and $\phi^{(2)} = \arg[\tilde{\rho}_{++,--}]$.

6.2.3 Two-photon nonlinear phase

The origin of the quantum nonlinearity is explained by the following simple model. The van der Waals interaction between two Rydberg atoms tunes the doubly excited Rydberg state far off EIT resonance for distances $|r| < r_B$, where $r_B = (\frac{4|\Delta|C_6}{\Omega_c^2})^{1/6}$ is the Rydberg blockade radius. Although the phase shift that would originate from the bare $|g\rangle \rightarrow |e\rangle$ probe transition is suppressed by EIT for photons with large separation in the medium ($|r| > r_B$), the light acquires this phase shift for small photon separations ($|r| \leq r_B$) (Fig. 6-12). Qualitatively, a substantial two-photon phase shift arises for $\frac{r_B}{L_a}\frac{\Gamma}{|\Delta|} \gtrsim 1$. Using the Rydberg state $|100S_{1/2}\rangle$, and for $\Omega_c = 2\pi\times$10MHz, we obtain $r_B \approx 18\mu m$ at detunings of a few Γ, $L_a = 4\mu m$ at the peak

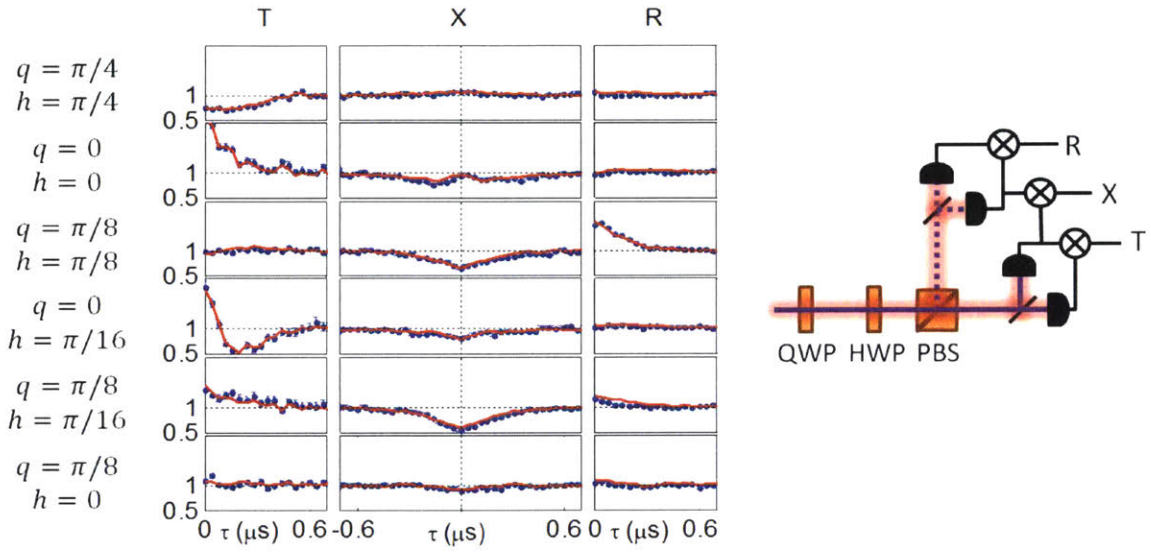

Figure 6-11: **Normalized photon-photon correlation functions in 6 polarization bases for $\Delta = 1.5\Gamma$.** Each setting of the quarter wave-plate (QWP) at an angle q and the half wave-plate (HWP) at an angle h (angles specified on the left) followed by a polarizing beam splitter determines a polarization basis for three $g^{(2)}_{\alpha,\beta}(\tau)$ measurements (blue points): for two transmitted photons (T), for two reflected photons (R), and for one-transmitted-one-reflected (X). The bases are equivalent to those proposed in Ref. [79]. The 18 pair counts from 6 different bases are used to tomographically reconstruct the two-photon density matrix using the maximum-likelihood estimation. Together with the reconstructed one-photon density matrix (obtained from the single counts), one can calculate the reconstructed $g^{(2)}_{\alpha,\beta}(\tau)$ (red line).

density, and $w = 4.5\mu m$, fulfilling the conditions for strong interactions for $|\Delta| \lesssim 5\Gamma$. To get an idea how big the phase shift is expected, we take the spectra with

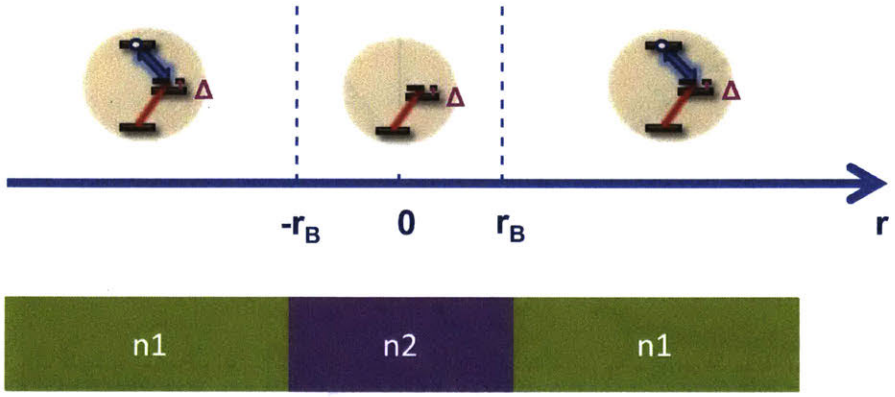

Figure 6-12: **Illustration of the change of refractive index inside and outside the blockade radius r_B.**

(representing outside r_B) and without (representing inside r_B) the control laser (Fig. 6-13). To best see the case of non-interacting photons, we use the lowest possible input rate so that two photons are rarely in the vicinity of each other. When the input photon rate is increased, a significant amount of photons are subjected to the interaction, and consequently the spectra deviate from those of low rate and change towards those without the control. Under EIT condition (marked by the vertical solid black line in Fig. 6-13), the differential phase shift with and without control is on the order of π, and the interacting photons are expected to pick up a negative phase since without control the phase is negative.

The nonlinear phase shift $\phi^{(2)}(\tau = 0)$ can reach $(-0.32 \pm 0.02)\pi$ (Fig. 6-14), at a detuning $\Delta = 2\pi \times 9$ MHz and a linear transmission of order 50%. There is a trade-off between the transmission and the phase. Recently, D. Tiarks et al. [81] realizes a π phase shift imprinted by a stored photon onto propagating photons, with much lower transmission.

6.2.4 The Schrödinger equation and effective mass

The simple picture presented in the previous section does not explain why there is very little nonlinear phase shift when $\Delta < 0$, as shown in Fig. 6-15. Here, in this

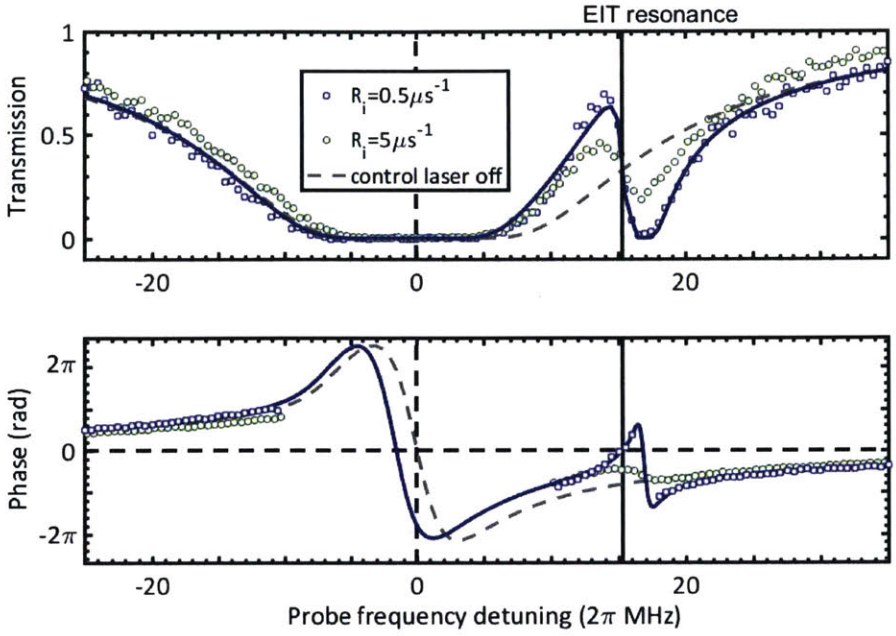

Figure 6-13: **Transmission spectra (top) and the phase shift (bottom) for σ^+ photons with an incoming rate of $R_i = 0.5\mu s^{-1}$ (blue squares) or $R_i = 5\mu s^{-1}$ (green circles), for a control field red-detuned by $\Delta = 2\pi \times 15$MHz.** The blue line shows the theoretical spectrum. The spectrum at high probe rate approaches that of the undriven two-level system (dashed grey). The solid vertical line corresponds to the EIT resonance.

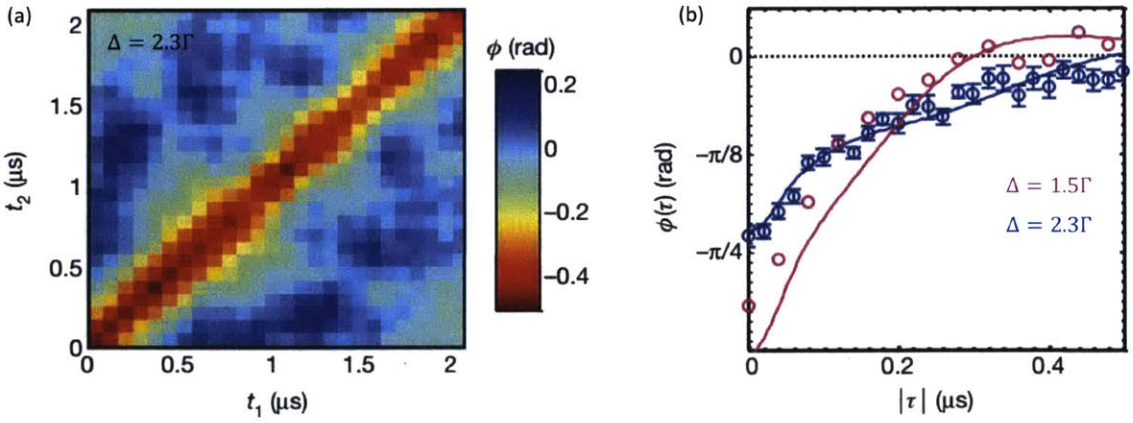

Figure 6-14: **Two-photon nonlinear phase $\phi^{(2)}$. (a)**, The photons are detected at times t_1 and t_2 for $\Delta = 2.3\Gamma$. **(b)**, $\phi^{(2)}$ vs $|\tau|$ for two different detunings ($\Delta = 1.5\Gamma$, purple, and $\Delta = 2.3\Gamma$, blue). Points are experimental data; lines are full numerical simulations.

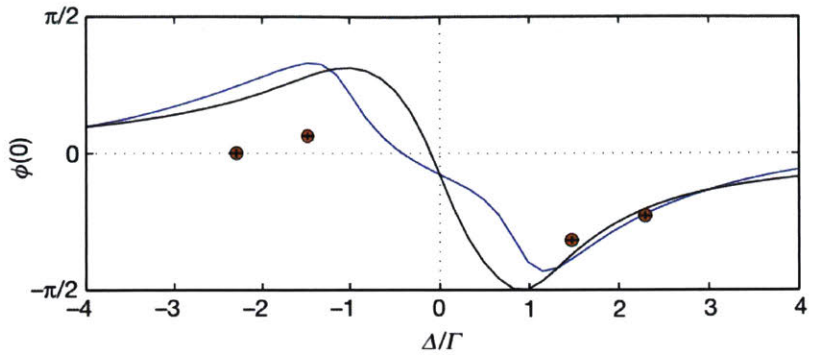

Figure 6-15: **The nonlinear phase $\phi^{(2)}(0)$ vs detuning Δ from the intermediate state $|e\rangle$.** Blue lines are full theoretical simulations and black lines are the result of the Schrödinger equation approximation, assuming a simplified δ-function potential.

section, I will more quantitative analysis to address the asymmetry under the sign change of Δ. The propagation of σ^+-polarized photon pairs can be understood by first considering an idealized situation with no decoherence between the Rydberg state and the ground state ($\gamma_{gr} = 0$). Then the steady state in a one-dimensional homogenous medium can be described by a two-photon wavefunction, $\psi^{(2)}$, whose evolution is approximately governed by a simple equation (Eq. 6.24) in terms of the centre-of-mass coordinate r and the relative coordinate r:

$$i\frac{\partial\psi^{(2)}}{\partial R} = 4L_a[i + \frac{2\Delta}{\Gamma} - \mathcal{V}(r)\frac{\Omega_c^2}{\Gamma^2}]\frac{\partial^2\psi^{(2)}}{\partial r^2} + \frac{\mathcal{V}(r)}{L_a}\psi^{(2)} \tag{6.1}$$

Here, the effective potential $\mathcal{V}(r) = \frac{1}{\frac{2\Delta}{\Gamma}+i+2\frac{r^6}{r_b^6}}$ approaches $\frac{1}{i+2\Delta/\Gamma}$ inside the blockaded volume ($|r| < r_B$) and approaches zero outside. The solution relates approximately to our measurements in the time domain for small $|\tau|$ via $\psi^{(2)}(R = L, r = v_g\tau) \approx \sqrt{g_{++}^{(2)}(\tau)}e^{i\phi^{(2)}(\tau)}$. Far off resonance ($|\Delta| \gg \Gamma$, Ω_c), Eq. 6.1 corresponds to a Schrödinger equation with R playing the part of effective time. The first term on the right-hand side is an effective mass term. The photons' effective mass can be positive or negative depending on the sign of the detuning Δ. Because the sign of the potential also changes with Δ (potential well for $\Delta < 0$; barrier for $\Delta > 0$), the effective force in both cases is attractive and the resulting dynamics similar. However, the potential for $\Delta < 0$ also has additional features near the edges of the well, corresponding to

a Raman resonance for the interaction-shifted Rydberg state at some inter-atomic distance near $|r| = r_B$. These features are probably responsible for the deviation from symmetry (or antisymmetry) under the change of the sign of Δ displayed in Figs. 6-17(a) and 6-15.

6.2.5 Photon bunching

A particle with negative mass in a potential barrier can be seen as one with positive mass in a potential well propagating reversely in time, and experiences attractive force. Therefore, I will refer to both $\Delta \gtrless 0$ as in a potential well. This potential well does not only induce a nonlinear phase shift, but also causes photon bunching– Photons are attracted towards each other. To emphasize, unlike the photon anti-bunching described in Sec. 6.1, the bunching here is driven by force not differential loss between the one- and two-photon components. As shown in the top panel of Fig. 6-13, under EIT condition, with our parameters, the transmission with and without the control laser is about the same. This represents the loss outside and inside the blockade radius is similar.

Figure 6-16(b) shows the intensity correlation in the dissipation-dominated anti-bunching regime at $\Delta = 0$ and in the dispersive regime at $|\Delta| > \Gamma$, where there is bunching. The transition from the dissipative regime to the dispersive is summarized in Figs. 6-17(a) and 6-15.

It is worth noting that the mass term sets a profound difference between our nonlinear system and a conventional Kerr medium. P. Bienias and H. P. Büchler [82] show that when the mass term is dropped, with a delta function potential, Shapiro's no-go problem is recovered. Additionally, without the mass term, no photon bunching is induced, although there is a nonlinear phase shift whose value is different from that with the mass.

Last, the van der Waals interactions of the nS Rydberg states are generally repulsive, because the dominant contribution comes from the $(n-1)P$ states just below nS states, and consequently the second-order interaction pushes nS states up. At first glance, it seems anti-intuitive that the repulsive Rydberg-Rydberg interaction leads

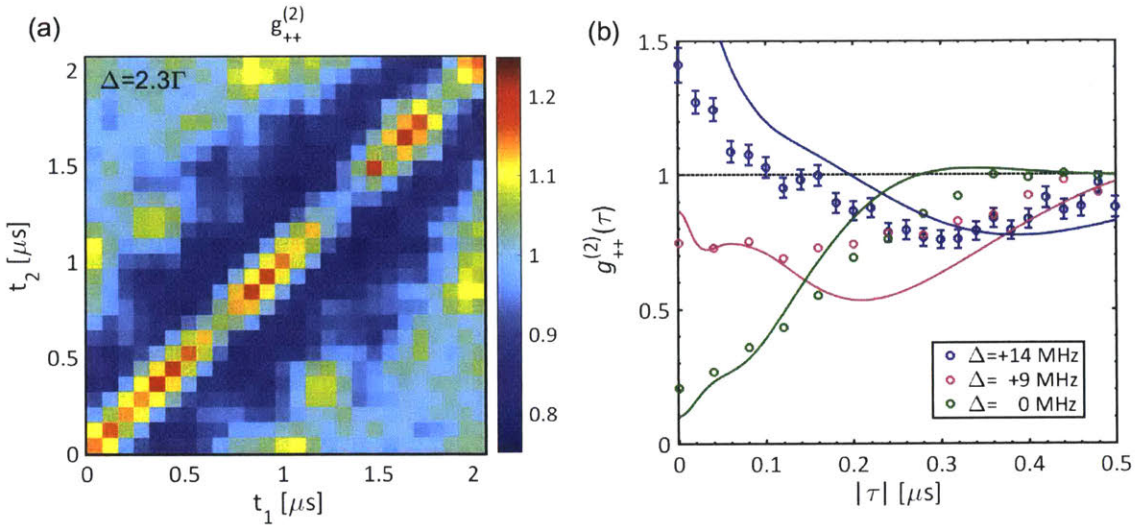

Figure 6-16: **Second-order correlation function $g^{(2)}_{++}$ of interacting photon pairs. (a)**, Measured $g^{(2)}_{++}$ for photons are detected at times t_1 and t_2 and $\Delta = 2.3\Gamma$. **(b)**, $g^{(2)}_{++}$ as a function of the time difference $|\tau| = |t_1 - t_2|$ between the photons, showing the transition from anti-bunching on resonance ($\Delta = 0$, green) to bunching at large detuning ($\Delta = 2.3\Gamma$, blue). Points are experimental data; lines are full numerical simulations. All $g^{(2)}_{++}$ measurements are rescaled by their value at $\tau > 1.5\mu s$.

to an attraction between the photons. However, as can been seen from the simple picture in Sec. 6.2.3, the sign of the nonlinear phase does not depend on whether the Rydberg-Rydberg interaction is repulsive or attractive. We merely use the fact that the interaction shifts the Rydberg level out of resonance. P. Bienias et al. [83] has shown that in order to change the interaction from attractive to repulsive, we need to work in a regime where the group velocity of the photon pairs is slower than the singles, opposite from where we are now. Using a large control Rabi frequency $\Omega_c > |\Delta|$ will satisfy the group velocity requirement.

6.2.6 Entanglement

we study the quantum coherence and polarization properties of the transmitted photon pairs. In Fig. 6-18(a), we compare the purity of the two-photon density matrix $\rho(\tau)$, which includes photon interactions, with the purity of the product of one-photon matrices $\rho^{(1)} \otimes \rho^{(1)}$ for non-interacting photons. At large photon separation τ, the

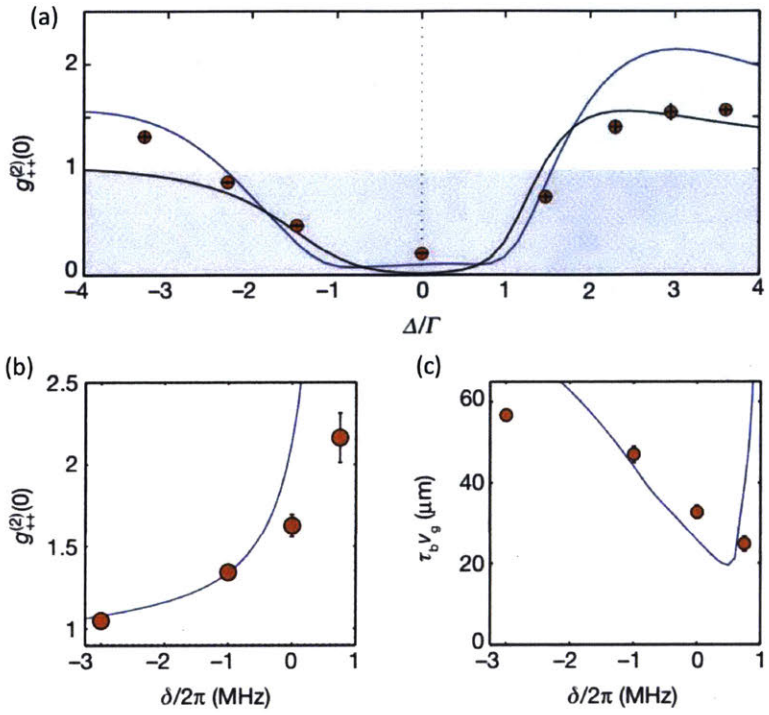

Figure 6-17: **Dependence of $g^{(2)}_{++}$ on detuning.** Equal-time two-photon correlation $g^{(2)}_{++}(0)$ **(a)** vs detuning Δ from the intermediate state $|e\rangle$. Blue lines are full theoretical simulations and black lines are the result of the Schrödinger equation approximation, assuming a simplified δ-function potential. Equal-time correlation function **(b)** and spatial extent of the bunching feature **(c)** versus Raman detuning δ from the EIT resonance $|g\rangle \rightarrow |r\rangle$ for $\Delta = 3\Gamma$, showing increased photonphoton attraction due to a deeper potential near Raman resonance. The characteristic bunching timescale τ_b is the half-width of the cusp feature of $g^{(2)}_{++}$, defined at half-height between the peak value at $\tau = 0$ and the local minimum closest to $\tau = 0$. Close to the Raman resonance at $\delta = 2\pi \times 1.3\text{MHz} \approx \frac{\Omega_c^2}{4\Delta}$, the single-photon component of the probe field is strongly absorbed. Thus, the theoretical model (solid line) breaks down because it computes the denominator only from the one-photon component and the numerator only from the two-photon component.

purity $P(\tau)$ of the two-photon density matrix is dominated by the one-photon decoherence due to partial depolarization of the transmitted light. This depolarization is attributed to the difference in group delay τ_d, between the σ^+ photons and the faster σ^- photons ($\tau_d^{\sigma^+} - \tau_d^{\sigma^-}$=280ns), which is not negligible compared with the coherence time of the probe laser (650 ns). At the same time, σ^+ photons bound to each other travel faster and are more robust against this decoherence mechanism, as evidenced by the greater purity at small τ. Even in the presence of this depolarization, the coherent nonlinear interaction in the dispersive medium produces entanglement in the outgoing polarization state of two photons. We quantify the degree of polarization entanglement in terms of a time-dependent concurrence $C(\tau)$ (Fig. 6-18(b)). The obtained value $C(0) = 0.09 \pm 0.03$ indicates deterministic entanglement of previously independent photons on passage through the quantum nonlinear medium. The measured value is in reasonable agreement with the theoretical prediction, $C(0) = 0.13$, calculated for a conditional phase $\phi^{(2)}(0) = \pi/4$, purity $P(0) = 0.73$ and 50% σ^+ linear transmission.

6.3 Theoretical description

6.3.1 Set up the equations

Adding the interaction term to Eq. 4.1 leads to

$$\begin{aligned}
\partial_t \hat{\mathcal{E}}(z,t) &= -c\partial_z \hat{\mathcal{E}}(z,t) + i\frac{g_p}{2}\sqrt{\rho(z)}\hat{\mathcal{P}}(z,t) \\
\partial_t \hat{\mathcal{P}}(z,t) &= -(\frac{\Gamma}{2} - i(\Delta+\delta))\hat{\mathcal{P}}(z,t) + i\frac{g_p}{2}\sqrt{\rho(z)}\hat{\mathcal{E}}(z,t) + i\frac{\Omega_c}{2}\hat{\mathcal{S}}(z,t) \\
\partial_t \hat{\mathcal{S}}(z,t) &= -(\frac{\gamma_{gr}}{2} - i\delta)\hat{\mathcal{S}}(z,t) + i\frac{\Omega_c}{2}\hat{\mathcal{P}}(z,t) - i\int dz' V(z-z')\hat{\mathcal{S}}^\dagger(z',t)\hat{\mathcal{S}}(z',t)\hat{\mathcal{S}}(z,t)
\end{aligned} \tag{6.2}$$

where the van der Waals interaction $V(z) = \frac{C_6}{z^6}$.

We define

$$\psi^{(2)}(z_1,z_2) = \frac{EE(z_1,z_2)}{E(z_1)E(z_2)} \tag{6.3}$$

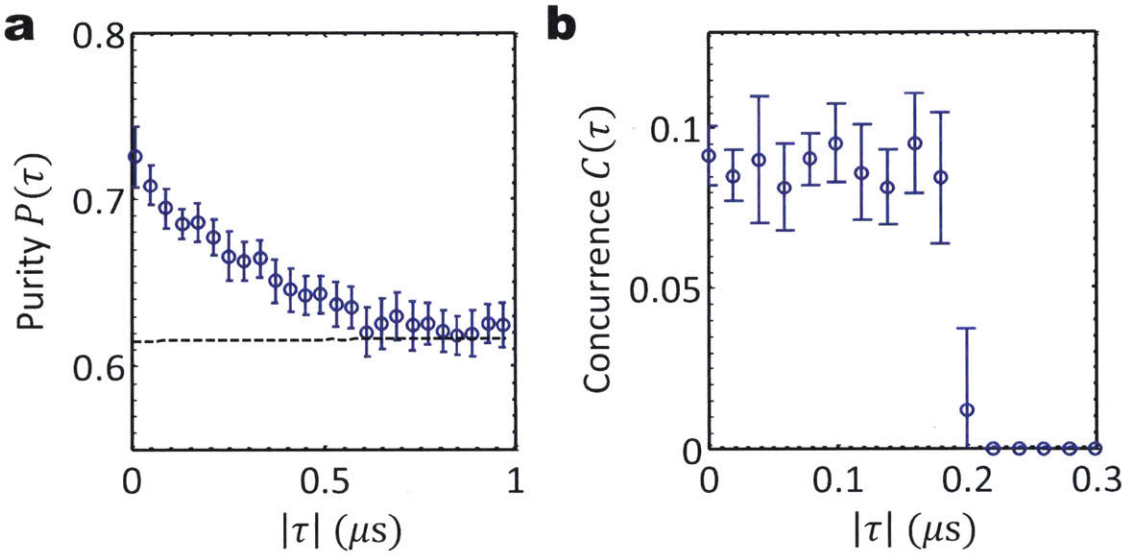

Figure 6-18: **Quantum coherence and entanglement.** **(a)** Purity $P(\tau) = Tr[\rho(\tau)^2]$ of the measured two-photon density matrix ρ for $\Delta = 2.3\Gamma$ (blue symbols), which at large photon separation approaches the purity expected from the measured one-photon density matrix $Tr[(\rho^{(1)} \otimes \rho^{(1)})^2]$ (dotted black line). Interacting $\sigma^+\sigma^+$ photon pairs near $\tau = 0$ exhibit lower decoherence. Error bars are derived from the uncertainty in the density matrix due to detection shot-noise. **(b)** Concurrence $C(\tau)$ calculated from ρ, indicating polarization entanglement of proximal photons on transmission through the quantum nonlinear medium.

which is unity in the absence of interactions, and

$$\psi^{(2)}(\tau \geq 0) = \psi^{(2)}(z_1 = z_0 + c\tau, z_2 = z_0) \tag{6.4}$$

where z_0 is outside the medium, and the two-photon probability amplitude is defined as $EE(z_1, z_2) = \langle 0|\hat{\mathcal{E}}(z_1)\hat{\mathcal{E}}(z_2)|\Psi\rangle$, where $|\Psi\rangle$ is the state of the system. With these definitions, at low rate limit, $g^{(2)}(\tau) = |\psi^{(2)}(\tau)|^2$ and $\phi^{(2)}(\tau) = \arg(\psi^{(2)}(\tau))$. Compared with the standard definition $g^{(2)} = \frac{\langle\Psi|\hat{\mathcal{E}}^\dagger(z_2)\hat{\mathcal{E}}^\dagger(z_1)\hat{\mathcal{E}}(z_1)\hat{\mathcal{E}}(z_2)|\Psi\rangle}{\langle\Psi|\hat{\mathcal{E}}^\dagger(z_2)\hat{\mathcal{E}}(z_2)|\Psi\rangle\langle\Psi|\hat{\mathcal{E}}^\dagger(z_1)\hat{\mathcal{E}}(z_1)|\Psi\rangle}$, we assume the denominator is dominated by the single-photon component and the numerator by the two-photon component.

We now turn to the two-excitation components. We divide the $z_1 - z_2$ plane into nine regions (Fig. 6-19). To obtain the equations governing the two-particle amplitudes in these regions, we use Eq. 6.2 and identities of the form $ES(z_1, z_2) = \langle 0|\hat{\mathcal{E}}(z_1)\hat{\mathcal{S}}(z_2)|\Psi\rangle$ and $EP(z_1, z_2) = \langle 0|\hat{\mathcal{E}}(z_1)\hat{\mathcal{P}}(z_2)|\Psi\rangle$.

In region 7, neither of the photons has entered the medium, and from Eq. 4.2, $EE(z_1, z_2) = \alpha^2$. This gives a time-independent boundary condition

$$EE(z_1, z_2 = 0) = \alpha^2 \tag{6.5}$$

for region 4, where the equations of motion are

$$\begin{aligned}
\partial_t EE(z_1, z_2) &= -c(\partial_{z_1} + \partial_{z_2})EE(z_1, z_2) + i\frac{g_p}{2}\sqrt{\rho(z_2)}EP(z_1, z_2) \\
\partial_t EP(z_1, z_2) &= -(c\partial_{z_1} + \frac{\Gamma}{2} - i(\Delta + \delta))EP(z_1, z_2) + i\frac{g_p}{2}\sqrt{\rho(z_2)}EE(z_1, z_2) + i\frac{\Omega_c}{2}ES(z_1, z_2) \\
\partial_t ES(z_1, z_2) &= -(c\partial_{z_1} + \frac{\gamma_{gr}}{2} - i\delta)ES(z_1, z_2) + i\frac{\Omega_c}{2}EP(z_1, z_2)
\end{aligned} \tag{6.6}$$

These equations describe the propagation of the photon component at position z_1 outside the medium at the speed of light and the propagation of the Rydberg polariton at position z_2 inside the EIT medium. The time-independent boundary condition Eq. 6.5 gives rise to a steady-state solution of Eq. 6.6, leading to boundary conditions for

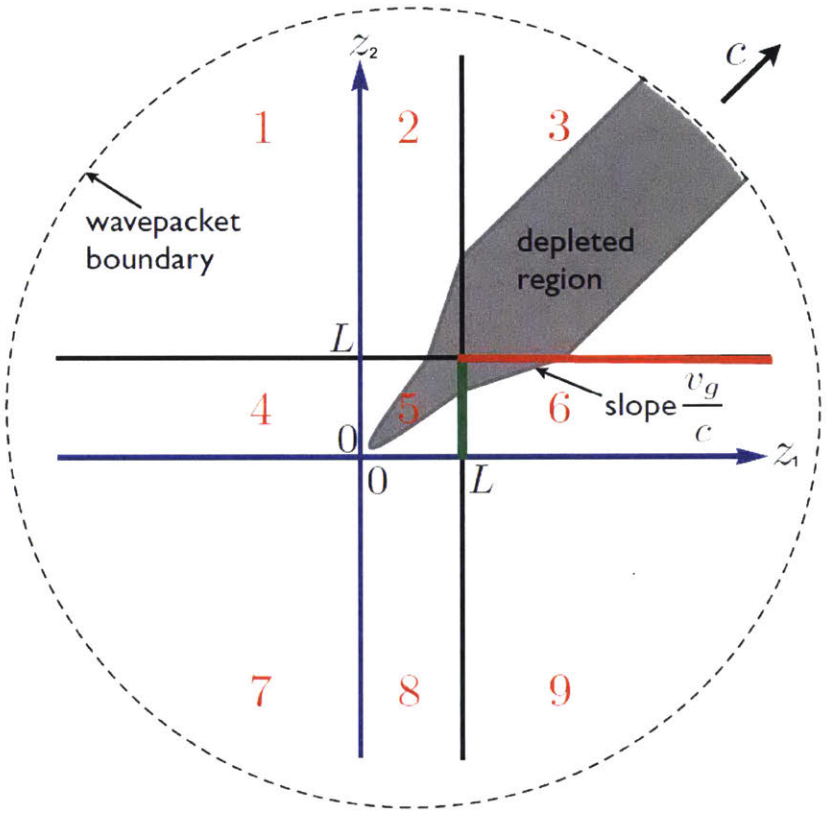

Figure 6-19: **The schematic diagram of the two-particle wavefunction.** z_1 and z_2 are the coordinates of the two particles, and the medium extends from 0 to L. In regions 1, 3, 7, and 9, both excitations are outside the medium. In regions 2, 4, 6, and 8, one excitation is inside the medium, while the other one is outside. Finally, in region 5, both excitations are inside the medium. We assume that the incident wavepacket is much longer than the extent of the medium (even after EIT compression). Therefore, the two-excitation wavepacket (boundary shown by the dashed line), which is moving in the top-right direction with c, is much larger than region 5. The distortion of the wavepackets boundary due to EIT time delay is not shown. For the ease of presentation, the broadening of the depletion region in region 6 assumes $c/v_g = 3$ (in the experiment, c/v_g is 5 orders of magnitude larger). The diagram is symmetric across the line $z_1 = z_2$.

region 5

$$
\begin{aligned}
EE(z_1=0,z_2) &= \alpha E(z_2) \\
ES(z_1=0,z_2) &= -\alpha\frac{g_p\sqrt{\rho(z_2)}}{\Omega_c}\frac{1}{[1+(\frac{\Gamma}{2}-i(\Delta+\delta))(\frac{\gamma_{gr}}{2}-i\delta)/(\Omega_c/2)^2]}E(z_2) \\
EP(z_1=0,z_2) &= \alpha\frac{i\frac{g_p\sqrt{\rho(z_2)}}{2}(\frac{\gamma_{gr}}{2}-i\delta)}{(\frac{\Omega_c}{2})^2+(\frac{\Gamma}{2}-i(\Delta+\delta))(\frac{\gamma_{gr}}{2}-i\delta)}E(z_2)
\end{aligned}
\tag{6.7}
$$

where $E(z_2)=\alpha\exp[-\frac{\frac{\Gamma}{2}(\frac{\gamma_{gr}}{2}-i\delta)\frac{OD}{2}}{(\frac{\Omega_c}{2})^2+(\frac{\Gamma}{2}-i(\Delta+\delta))(\frac{\gamma_{gr}}{2}-i\delta)}\int_{-z_2/2}^{z_2/2}\rho(z')\frac{dz'}{\sqrt{2\pi}\sigma_a}]$. Intuitively, since one photon is outside the medium and therefore there is no interaction between the two photons, the two-photon components can be written as the products of the one-photon components. Namely, $EE(z_1=0,z_2)=E(z_1=0)E(z_2)$, $ES(z_1=0,z_2)=E(z_1=0)S(z_2)$ and $EP(z_1=0,z_2)=E(z_1=0)P(z_2)$, where $E(z_1=0)=\alpha$. The one inside the medium is governed by Eq. 6.2, without the interaction term. In region 5, both excitations are inside the medium and are subject to interactions as described by the following propagation equations:

$$
\begin{aligned}
\partial_t EE(z_1,z_2) = &\quad -c(\partial_{z_1}+\partial_{z_2})EE(z_1,z_2)+\frac{ig_p}{2}(\sqrt{\rho(z_2)}EP(z_1,z_2)+\sqrt{\rho(z_1)}EP(z_2,z_1)) \\
\partial_t EP(z_1,z_2) = &\quad -(c\partial_{z_1}+\frac{\Gamma}{2}-i(\Delta+\delta))EP(z_1,z_2) \\
&\quad +\frac{ig_p}{2}(\sqrt{\rho(z_2)}EE(z_1,z_2)+\sqrt{\rho(z_1)}PP(z_1,z_2))+\frac{i\Omega_c}{2}ES(z_1,z_2) \\
\partial_t ES(z_1,z_2) = &\quad -(c\partial_{z_1}+\frac{\gamma_{gr}}{2}-i\delta)ES(z_1,z_2)+\frac{ig_p}{2}\sqrt{\rho(z_1)}PS(z_1,z_2)+\frac{i\Omega_c}{2}EP(z_1,z_2) \\
\partial_t PS(z_1,z_2) = &\quad -(\frac{\Gamma}{2}-i(\Delta+\delta)+\frac{\gamma_{gr}}{2}-i\delta)PS(z_1,z_2) \\
&\quad +\frac{ig_p\sqrt{\rho(z_1)}}{2}ES(z_1,z_2)+\frac{i\Omega_c}{2}(PP(z_1,z_2)+SS(z_1,z_2)) \\
\partial_t PP(z_1,z_2) = &\quad -2(\frac{\Gamma}{2}-i(\Delta+\delta))PP(z_1,z_2)+\frac{ig_p}{2}(\sqrt{\rho(z_1)}EP(z_1,z_2) \\
&\quad +\sqrt{\rho(z_2)}EP(z_2,z_1))+\frac{i\Omega_c}{2}(PS(z_1,z_2)+PS(z_2,z_1)) \\
\partial_t SS(z_1,z_2) = &\quad \frac{i\Omega_c}{2}(PS(z_1,z_2)+PS(z_2,z_1))-(iV(z_1-z_2)+2(\frac{\gamma_{gr}}{2}-i\delta))SS(z_1,z_2)
\end{aligned}
\tag{6.8}
$$

The time-independent boundary conditions Eq. 6.7 allow us to solve Eq. 6.8 in steady state. The resulting depletion of $|EE(z_1, z_2)|^2$ in region 5 when $\Delta = 0$ is shown schematically in Fig. 6-19 and is plotted in Fig. 6-20. This gives a boundary condition at $z = L$ to region 6, which, together with the boundary condition $EE(z > L, 0) = \alpha^2 \exp[-\frac{\frac{\Gamma}{2}(\frac{\gamma_{gr}}{2} - i\delta)\frac{OD}{2}}{(\frac{\Omega_c}{2})^2 + (\frac{\Gamma}{2} - i(\Delta+\delta))(\frac{\gamma_{gr}}{2} - i\delta)}]$, yields a steady-state solution in region 6, where Eq. 6.6 hold. Finally, in region 3, both photons are outside the medium, so $EE(z_1, z_2)$ is constant along constant $z_1 - z_2$.

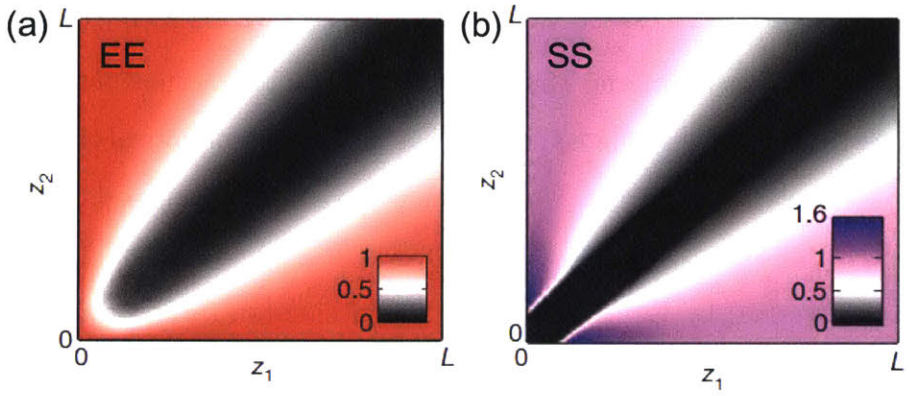

Figure 6-20: **Numerical simulations showing the spatial evolution of the probability distribution associated with two photons (a) and two Rydberg excitations (b) at positions (z_1, z_2) inside the medium, normalized by their values in the absence of blockade.** Two Rydberg excitations are excluded from the blockaded range, resulting in the formation of an anti-bunching feature in the light field, whose width increases during the propagation due to the finite EIT transparency width $B = \gamma_{EIT}/\sqrt{8OD}$. The plots are made for $\Delta = 0$. When $\Delta \gg \Gamma$, there is a similar broadening of the depletion region of $SS(z_1, z_2)$, but $EE(z_1, z_2)$ is not depleted.

6.3.2 The numerical solution

The denominator of $\psi(\tau)$ can be easily found analytically using Eq. 4.4. To compute $g^{(2)}(\tau)$ numerically for comparisons to the experiment, we take into account the transverse extent of the beam by writing $V(z) = \frac{C_6}{[z^2 + r_\perp^2]^3}$, where $r_\perp$ is the transverse profile of the probe beam. Neglecting probe-beam diffraction, this amounts to solving Eq. 6.8 for different $r_\perp$. The numerator of $g^{(2)}(\tau)$ is then computed by taking an average over the $r_\perp$ distribution. We achieve best agreement for a beam waist of $w = 6\mu m$, which is slightly larger than the measured value of $4.5\mu m$, possibly due

to the imperfect positioning of the cloud relative to the waist and finite diffraction (Rayleigh range $z_R = 82\mu m$) of the beam along the length of the atomic cloud.

In Fig. 6-3, the theoretical curves obtained from the mode are corrected for independently measured detection noise ($g^{(2)}_{corrected}(\tau) = g^{(2)}(\tau) + (1 - g^{(2)}(\tau))(p_1 + p_2)$, where p_i denotes the ratio of the noise counts to the signal counts for the i^{th} detector), and then linearly scaled to approximately account for the super-Poissonian behavior at large τ.

6.3.3 The analytical solution

In order to obtain an approximate single equation describing the steady-state behavior of the two-particle wavefunction, we now analyze the steady state of Eq. 6.8. We define $ES_{\pm}(z_1, z_2) = (ES(z_1, z_2) \pm ES(z_2, z_1))/2$, $EP_{\pm}(z_1, z_2) = (EP(z_1, z_2) \pm EP(z_2, z_1))/2$ and $PS_{\pm}(z_1, z_2) = (PS(z_1, z_2) \pm PS(z_2, z_1))/2$, as well as center-of-mass and relative coordinates $R = (z_1 + z_2)/2$ and $r = z_1 - z_2$ of the two excitations.

To simplify the equations, we approximate the medium as a homogeneous slab with length $L = 4.2\sigma_a$. The factor of 4.2 is chosen such that the analytical solution agrees with the numerical solution of the full sets of equations. With this approximation, $\rho(z) = 1$ in $[0, L]$ and 0 otherwise, and $\frac{g_p^2}{\Gamma c} = \frac{OD}{L}$. Furthermore, we take $\delta = \gamma_{gr} = 0$ so that $E(z) = \alpha$.

In steady-state, Eq. 6.8 then become

$$0 = -c\partial_R EE + ig_p EP_+ \tag{6.9}$$

$$0 = -c\partial_R EP_+ - 2c\partial_r EP_- - (\Gamma - 2i\Delta)EP_+ + ig_p(EE + PP) + i\Omega_c ES_+ \tag{6.10}$$

$$0 = -c\partial_R EP_- - 2c\partial_r EP_+ - (\Gamma - 2i\Delta)EP_- + i\Omega_c ES_- \tag{6.11}$$

$$0 = -c\partial_R ES_+ - 2c\partial_r ES_- + ig_p PS_+ + i\Omega_c EP_+ \tag{6.12}$$

$$0 = -c\partial_R ES_- - 2c\partial_r ES_+ + ig_p PS_- + i\Omega_c EP_- \tag{6.13}$$

$$0 = -(\Gamma - 2i\Delta)PS_+ + ig_p ES_+ + i\Omega_c(PP + SS) \tag{6.14}$$

$$0 = -(\Gamma - 2i\Delta)PS_- + ig_p ES_- \tag{6.15}$$

$$0 = -(\Gamma - 2i\Delta)PP + ig_p EP_+ + i\Omega_c PS_+ \tag{6.16}$$

$$0 = i\Omega_c PS_+ - iVSS \tag{6.17}$$

We next simplify these equations using a number of approximations. We solve Eq. 6.16 for EP_+ and insert the result into Eq. 6.9.

$$0 = -c\partial_R EE + (\Gamma - 2i\Delta)PP - i\Omega_c PS_+ \tag{6.18}$$

We solve Eqs. 6.15 for PS_-, insert the result into Eqs. 6.13, and neglect all but two terms that form the dominant balance.

$$0 = -2c\partial_r ES_+ - \frac{g_p^2}{\Gamma - 2i\Delta} ES_- \tag{6.19}$$

We only keep the two dominant terms in Eqs. 6.10 and 6.11.

$$0 = -2c\partial_r EP_- + ig_p PP \tag{6.20}$$

$$0 = -(\Gamma - 2i\Delta)EP_- + i\Omega_c ES_- \tag{6.21}$$

We neglect the last term in Eq. 6.12.

$$0 = -c\partial_R ES_+ - 2c\partial_r ES_- + ig_p PS_+ \tag{6.22}$$

Finally, we combine eqs. (6.14) and (6.17) into an expression for PS_+ by eliminating SS.

$$0 = -(\Gamma - 2i\Delta - i\frac{\Omega_c^2}{V})PS_+ + ig_pES_+ + i\Omega_c PP \tag{6.23}$$

Eliminating EP_- and PP from eqs. (6.18), (6.20) and (6.21), we find that $-\frac{g_p}{\Omega_c}EE$ obeys the same equation of motion as ES_+ in Eq. 6.22. Since $-\frac{g_p}{\Omega_c}EE$ also has the same boundary conditions as ES_+, $EE = -\frac{\Omega_c}{g_p}ES_+$ at all R and r. This means that ES_+ and EE obey the dark-polariton relationship (Eq. 4.20) for all R and r. This is a surprising result, as one would not naively expect this relationship to hold within the blockaded region. Eliminating EP_-, PP, ES_- and PS_+ from eqs. (6.19) to (6.23), and keeping in mind that EE obeys the same equation as ES_+, we find a Schrödinger equation for the two-photon probability amplitude EE for $z_1, z_2 \in [0, L]$

$$i\partial_R EE(R,r) = [-\frac{1}{2\tilde{m}(r)}\partial_r^2 + U(r)]EE(R,r) \tag{6.24}$$

where the spatially dependent mass $\tilde{m}(r)$ and potential $U(r)$ are given by

$$-\frac{1}{2\tilde{m}(r)} = \frac{4L}{OD}(\frac{2\Delta}{\Gamma} + i - (\frac{\Omega_c}{\Gamma})^2\mathcal{V}(r)) \tag{6.25}$$

$$U(r) = \frac{OD}{L}\mathcal{V}(r) \tag{6.26}$$

with $\mathcal{V}(r) = \frac{1}{\frac{2\Delta}{\Gamma}+i+2\frac{r^6}{r_b^6}}$. The resonant blockade radius is defined as $r_b = (\frac{2\Gamma C_6}{\Omega_c^2})^{1/6}$. The initial condition is $EE(z_1 = 0, z_2) = EE(z_1, z_2 = 0) = \alpha^2$.

By comparing the solutions of Eq. 6.24 with the numerical simulations of the full dynamics, we find that for $\Delta \neq 0$, this equation does not approximate the full dynamics as well as it does for $\Delta = 0$, with the error in EE as large as $\sim 20\%$. However, it still captures the main qualitative features of the two-photon evolution. In the regime $|\Delta| \gg \Gamma$, Ω_c, an excellent agreement with the full dynamics can be achieved by keeping higher-order derivatives in the effective equation.

In the presence of nonzero Δ, the blockade radius is increased to $\bar{r}_B = r_b((\frac{2\Delta}{\Gamma})^2 + 1)^{1/12}$. In the limit of $|\Delta| \gg \Gamma$, it corresponds to the off-resonant blockade radius $r_B = (\frac{4|\Delta|C_6}{\Omega_c^2})^{1/6}$. Outside the blockade region, $\tilde{m}(r > \bar{r}_B)$ stems directly from the

effective mass of a single dark-polariton. In the limit of $|\Delta| \gg \Gamma$, the mass is given by Eq. 4.24. Expressing Eq. 4.24 with different quantities and write out $\hbar$ explicitly (remember Ω_e is given in half width),

$$m = -\frac{1}{16\pi}\frac{c}{v_g}\frac{\lambda}{L_a}\frac{\Gamma}{\Delta}\frac{\hbar\omega}{c^2} = \frac{2\hbar}{v_g}\tilde{m} \tag{6.27}$$

where the factor of 2 comes from the two-body reduced mass, $\lambda\omega = 2\pi c$, and $L_a = L/OD$ is the resonant attenuation length. For our parameters, at the center of the medium, $|m|c^2 \approx 10^3\hbar\omega$.

6.3.4 The correlation function in the dissipative regime

Setting $\Delta = 0$ in Eq. 6.24 leads to

$$\partial_R EE = -i\frac{OD}{L}\mathcal{V}(r)EE + \frac{4L}{OD}(1 + i(\frac{\Omega_c}{\Gamma})^2\mathcal{V}(r))\partial_r^2 EE \tag{6.28}$$

with $\mathcal{V}(r) = \frac{1}{i+2\frac{r^6}{r_b^6}}$.

$g^{(2)}(\tau)$ can be read out from the solution of this equation along the boundary $z_1 = L$ (green line in Fig. 6-19) via

$$g^{(2)}(\tau) \approx \frac{|EE(z_1 = L, z_2 = L - v_g\tau)|^2}{|\alpha|^4} \tag{6.29}$$

It is remarkable that, for the full range of parameters considered in this experiment, the set of nine equations 6.9 to 6.17 is well-approximated by a single simple diffusion equation with a local loss term. The second term on the right-hand-side of Eq. 6.28 is the diffusion term, while the first term is the local loss term. Outside of the blockade radius ($\mathcal{V}(r) = 0$), we have a pure diffusion equation with a $4L/OD$ diffusion coefficient and no loss. Inside the blockade radius ($\mathcal{V}(r) = -i$), the diffusion coefficient is increased to $4(1+(\Omega_c/\Gamma)^2)L/OD$. An increase in the diffusion coefficient increases $g^{(2)}(0)$ and increases the half-width-at-half-maximum (HWHM) τ_c of the dip in $g^{(2)}(\tau)$.

In particular, a larger Ω_c gives a larger $g^{(2)}(0)$. The local loss term is nonzero on a strip of width $\approx 2r_b$ (or more precisely $\approx 2r_b/2^{1/6}$) where it has rate OD/L. This amplitude OD/L is consistent with physical intuition: $|EE|^2$ decays as $|EE(R = L)|^2 \propto |EE(R = 0)|^2 \exp[-2OD]$. The factor of 2 accounts for the fact that either of the two photons can be absorbed. The physics of this diffusion equation is as follows: the local loss term tries to deplete a narrow strip of width $\approx 2r_b$, while the diffusion term competes with the loss, preventing the depleted region from being too narrow. The diffusion term comes from the fact that the EIT medium cannot support without loss features narrower than the EIT bandwidth B. Its effect is illustrated by the following simple situation. Suppose we had no loss term and an incoming boundary condition $EE(0, r) = \delta(r)$. Then $EE(L, r)$ will acquire a width $L/\sqrt{OD}$. Converting to time using v_g, we would have a width $\sim L/(v_g\sqrt{OD}) = \tau_d/\sqrt{OD} \sim 1/B$, in agreement with the EIT bandwidth limit.

Under the approximation that $\mathcal{V}(r)$ is a delta function or a step function and assuming the boundary conditions are along $R = 0$ and $r = \pm\infty$, Eq. 6.28 can be solved analytically using a Laplace transformation in R. The inverse Laplace transform can be taken exactly in certain limits.

Specifically, in the case of $V(r) \approx -2ir_b\delta(r)$, we find that $g^{(2)}(0)$ depends only on $x \equiv OD_b\sqrt{OD}$, where $OD_b = ODr_b/L$ is the blockaded optical depth. In particular, for $x \ll 1$, $g^{(2)}(0) \approx 1 - x\sqrt{2/\pi}$, while for $x \gg 1$, $g^{(2)}(0) \approx 8/(\pi x^2)$. For $x \gg 1$, the HWHM of the dip in $|EE(L - r/2, r)|^2$ is given by $\approx 4\text{InverseErfc}[1 - 2^{-1/2}]/\sqrt{OD} \approx 3/\sqrt{OD}$. To get to the time units, one has to multiply by the EIT time delay τ_d, so we get the correlation time

$$\tau_c \approx 1.05/B \tag{6.30}$$

as expected from the physical intuition that the EIT medium cannot support without loss features wider in frequency space than B. Eq. 6.30 is shown as a dashed line in Fig. 6-5(b). It is remarkable that this simple formula derived by analytically solving the diffusion equation with delta-function loss term matches extremely well the experimental results.

In the case of $\mathcal{V}(r)$ being a unit step of length $2r_b$ [i.e. $f(|r| < r_b) = -i$ and $f(|r| > r_b) = 0$], in the limit of large OD, we find:

$$g^{(2)}(0) \approx \frac{4(1+(\frac{\Omega_c}{\Gamma})^2)}{\pi OD}\exp[-\frac{OD_b}{\sqrt{1+(\Omega_c/\Gamma)^2}}] \tag{6.31}$$

While $g^{(2)}(0)$ drops exponentially as one increases OD_b beyond unity, the reduction in $g^{(2)}(0)$ due to an increase in OD (for a fixed OD_b) is much slower ($\sim 1/OD$). We also see from Eq. 6.31, that the condition for the blockade to work used at the beginning of this chapter ($OD_b > 1$) can be stated more precisely as $OD_b^2 > 1+(\Omega_c/\Gamma)^2$. This condition simply means that the loss term must exceed the diffusion on the length scale of the blockade radius.

6.4 Summary and outlook

To conclude, we demonstrate strong single-photon nonlinearities in both dissipative and dispersive regimes by coupling to highly polarizable Rydberg states. In the dissipative regime, strong photon anti-bunching is observed. In the dispersive regime, nonlinear phase shifts on the order of π, as well as photon bunching, are demonstrated. The discussion about the dispersive regime will continue in the next chapter to further reveal the rich features of our unique nonlinear system.

Our observations suggest intriguing prospects for ultimate quantum control of light quanta. First, by accessing other Rydberg states via, for example, microwave transitions or additional laser fields, it is possible to control the state of multiphoton pulses with just one quantum of light, thereby realizing a single-photon transistor [20–22] for applications in quantum networks, and the creation of multiphoton entangled states. Second, by colliding two counter-propagating photons or storing a photon inside the medium, it may be possible to imprint a spatially homogeneous phase shift of π on the photon pair, corresponding to a deterministic quantum gate for scalable optical quantum computation [81,84]. Third, our results may open the door to exploring the quantum dynamics of strongly interacting photonic many-body systems. For exam-

ple, it may be possible to create a crystalline state of strongly interacting polaritons. At the same time, the realization of coherent, dispersive photon-photon interactions opens up the possibility to explore a novel quantum matter composed from strongly interacting, massive photons. Measurements of higher-order correlation functions may give direct experimental access to quantum solitons composed of a few interacting bosons, or to the detection of crystalline states of a photonic gas. Beyond these specific applications, our work demonstrates that unique quantum nonlinear optical materials can be created by combining slow-light propagation with strong atom-atom interactions, an approach which can be potentially extended to realize other material systems with quantum nonlinearities.

Chapter 7

Bound states of photons

In the previous chapter, I discussed the nonlinear phase shift and photon bunching due to the attractive force when operating in the dispersive regime. In this chapter, we further analyze those features and associate them with an indication of a two-photon bound state.

Although bound states are ubiquitous for massive particles, such as nuclei, atoms or molecules, bound states of photons have never been realized owing to their weak interactions and linear dispersion (no mass term). Nevertheless, bound states of light quanta have been proposed to exist in specifically engineered media with strong nonlinearity [85–88]. These can be viewed as quantum solitons [24, 25, 89], a stable wavepacket enabled by the cancellation of nonlinear and dispersive effects. The distinguishing feature of the quantum solitons is the nonlinearity so strong that the wave packet shape should strongly vary with the number of constituting photons. Extending these studies to create stable, complex bound states is of great interest. For one thing, it is a novel states of light and is along the lines of fundamental studies of photonic quantum matter [90, 91]. For another, it finds applications in areas such as quantum information [92, 93].

7.1 The two-photon bound state

In our nonlinear medium, the dynamics of the two-photon probability amplitude is governed by a Schrödinger equation with a potential well in 1D. In theory, such a system supports at least one bound state. In the experimentally relevant regime, the effective potential is weak enough such that it supports only one bound-state $\psi_B^{(2)}(r)$ (Fig. 7-1).

In our cw experiment, the initial wavefunction $\psi^{(2)}(R=0,r)=1$. At the entrance of the medium ($R=0$), the effective potential is suddenly switched on and $\psi^{(2)}$ is decomposed into a superposition of the bound state $\psi_B^{(2)}(r)$ and the continuum of scattering states (Fig. 7-1). The exit of the medium is a similar quench problem where the effective potential is suddenly switched off. This is very different from a usual scattering problem where a particle moves towards a potential, and have some forward and backward scattering amplitude, but never excite the bound states.

The quench approximation is valid when the variation of the density of the medium is faster than the length scale of the bound state. The experiments satisfy this requirement well, as shown in Fig. 7-2. Moreover, close to the edge of the medium, where the atomic density is lower, the extent of the bound state is even larger owing to a shallower potential.

From this picture, the photon bunching, or the accumulation of probability near $r=0$, can then be understood as arising from the interference between the bound and scattering states that evolve at different frequencies, and the observed bunching feature in $g_{++}^{(2)}$ reveals the wavefunction of the two-photon bound state. The strength of the two-photon interaction potential can be tuned by varying the probe field relative to the EIT resonance. As the probe detuning approaches the Raman absorptive resonance, the difference in refractive indices inside and outside the blockade radius increases and the potential deepens (Fig. 6-13). Consequently, the bound state becomes more localized and the bunching, quantified by $g_{++}^{(2)}(0)$, is enhanced (Fig. 6-17(b), (c)). We note that the size of the two-photon bound state and, correspondingly, the width of the bunching feature, $2\tau_b v_g \approx 70\mu m$, exceed the width of the potential

well, $2r_B \approx 35\mu m$, as expected for a potential with one weakly bound state.

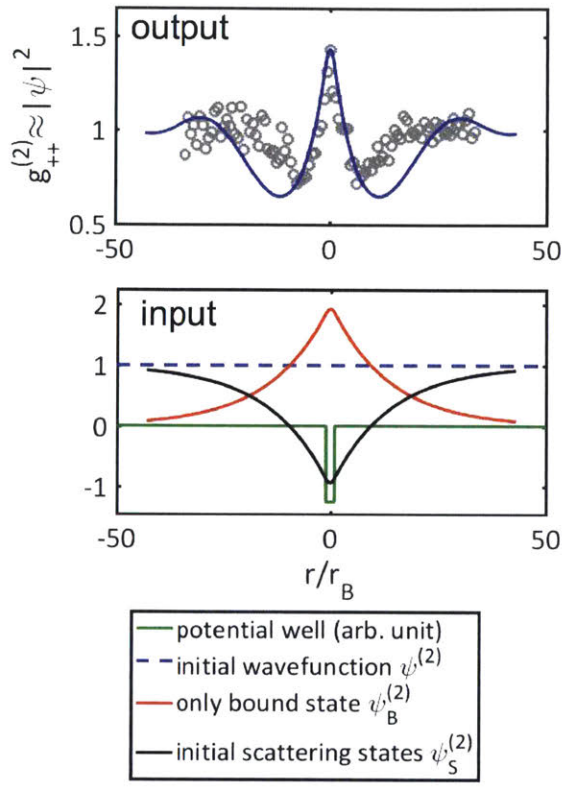

Figure 7-1: **Photon bunching and two-photon bound state.** Theoretically predicted photon-photon correlation function in the Schrödinger equation approximation (top, blue line) for $\Delta = 2\pi \times 14$MHz, with a potential well of width $2r_B$ (bottom, green line). At the entrance of the medium, the initial wavefunction, $\psi^{(2)} = 1$ (bottom, dashed blue) is projected onto the bound state (bottom, red) and the superposition of scattering states (bottom, black). The two-photon bound state results in the observed bunching in the correlation function, $g^{(2)}_{++} \approx |\psi^{(2)}|^2$ (top, grey circles), where time has been converted into distance using the group velocity v_g. The boundary effects resulting from the finite extent of the atom cloud become important for $r \geq 5r_B$.

To simplify the analysis, we make an additional approximation by assuming that the boundary conditions are $EE(R = 0, r) = EE(R, r = \pm\infty) = \alpha^2$. We find that this approximation is more forgiving than the approximations used in the derivation of Eq. 6.24. Dropping the r-dependent term in the effective mass (since it is typically small) and approximating the potential with a square well, we end up with a Schrödinger equation with a complex mass and a square-well potential with a complex amplitude, which can be solved directly. The analytical solution is further simplified

if one approximates the square-well potential with a δ function of the same area. This is a reasonable approximation because the variations in $EE(R,r)$ occur at a scale much larger than $\bar{r}_B$. For $|\Delta| \gg \Gamma$, when the mass and the potential are real, this follows from the fact that there is a single bound state and its extent is much larger than $\bar{r}_B$, as we will verify below. The mass and the potential then simplify to

$$-\frac{1}{2\tilde{m}(r)} = \frac{4L}{OD}(\frac{2\Delta}{\Gamma} + i) \tag{7.1}$$

$$U(r) = c_0 2OD_B \frac{1}{\frac{2\Delta}{\Gamma} + i}\delta(r) \tag{7.2}$$

where $OD_B = OD\frac{\bar{r}_B}{L}$ is the optical depth within a blockade radius and $c_0 = \frac{\pi}{2^{1/6}3} e^{i\,arg[(\frac{2\Delta}{\Gamma}+i)^{1/6}]}$ is chosen to keep $\int dr U(r)$ unchanged under the approximation. For $|\Delta| \gg \Gamma$, $arg[c_0] = 0$ and $\pi/6$ for $\Delta > 0$ and $\Delta < 0$, respectively, accounting for non-negligible Raman absorption for $\Delta < 0$ and capturing the asymmetry between positive and negative Δ in Figs. 6-17(a) and 6-15. The resulting problem is equivalent to a free-particle Schrödinger equation on $R \in [0, L]$ and $r \in [0, \infty]$ with mixed boundary conditions at $r = 0$. Using Laplace transformation in R, we find

$$\psi^{(2)}(\tau = 0) = \psi^{(2)}(R = L, r = 0) = e^{u^2}\text{erfc}[u] \tag{7.3}$$

where erfc is the complementary error function and

$$u = \frac{c_0\sqrt{OD}OD_B}{2(1 - i\frac{2\Delta}{\Gamma})^3/2} \tag{7.4}$$

This formula is used to make the solid black curves in Figs. 6-17(a) and 6-15. At small u, we have $\psi^{(2)} - 1 = -\frac{2u}{\sqrt{\pi}} + \mathcal{O}(u^2)$, which, for $|\Delta| \gg \Gamma$, gives $\arg[\psi^{(2)}(0) - 1] = \pm\pi/4 + arg[c_0]$ for $\Delta \lessgtr 0$.

Within the δ-function approximation and by further assuming that $\Delta \gg \Gamma$, we obtain a real (negative) mass and a real (positive) potential. To get insight into the

role of the bound state, we solve for the dynamics in this case analytically:

$$\psi^{(2)}(R,r) = \psi_B^{(2)}(R,r) + \psi_S^{(2)}(R,r) \tag{7.5}$$

where $\psi_B^{(2)}$ and $\psi_S^{(2)}$ are the contributions of the bound state and the scattering states, respectively.

$$\psi_B^{(2)}(R,r) = 2e^{-\kappa|r|}e^{-i8\kappa^2 RL\Delta/(OD\Gamma)} = 2e^{-\kappa|r|}e^{-i\frac{\kappa^2}{2\bar{m}}(-R)} \tag{7.6}$$

$$\psi_S^{(2)}(R,r) = \int_0^\infty dk \frac{i(b_k^{-1}-1)}{2\pi k}(e^{ik|r|} + b_k e^{-ik|r|})e^{i8k^2 RL\Delta/(OD\Gamma)} \tag{7.7}$$

where $\kappa = c_0(OD\Gamma/\Delta)^2\bar{r}_B/(16L^2)$ and $b_k = (ik+\kappa)/(ik-\kappa)$. Taking $OD = 22$, $\Delta = 2\pi \times 14$MHz, and $\Omega_c = 2\pi \times 10$ MHz, the condition $\kappa\bar{r}_B = c_0(OD_B\Gamma/\Delta)^2/16 \approx 1/14 \ll 1$ ensures that the extent of the bound state is indeed much wider than the blockade radius justifying the δ-function approximation. The last equality of Eq. 7.6 makes use of Eq. 7.1 when $\Delta \gg \Gamma$. It shows that the bound state would acquire a negative phase before the phase wraps around.

For the case of a square well, $\psi_B^{(2)}(0,r)$, $\psi_S^{(2)}(0,r)$ and $|\psi^{(2)}(L,r)|^2$ are shown as red, black, and solid blue curves in Fig. 7-1. Within this solution, the observed bunching can be understood as resulting from the relative phase evolution between the bound and the scattering states. For the parameters given above, both terms in Eq. 7.5 contribute to the super-Poissonian feature at $r = 0$. The bound state $\psi_B^{(2)}$ acquires a phase and becomes the dominant contribution to the imaginary part of $\psi^{(2)}$. The superposition of scattering states $\psi_S^{(2)}$ starts with a dip (because the bound-state contribution is subtracted), but its phase evolution quickly "fills in" the dip associated with the real part of $\psi^{(2)}$, while contributing very little to the imaginary part. A combination of both the real and imaginary parts of $\psi^{(2)}$ results in the bunching feature of $|\psi^{(2)}|^2$. Therefore, consistent with a simple intuition, the super-Poissonian $g^{(2)}(0)$ is indeed driven by the bound-state formation (see Fig. 7-2).

In the limit of a very long medium (increasing OD and L proportionally), the

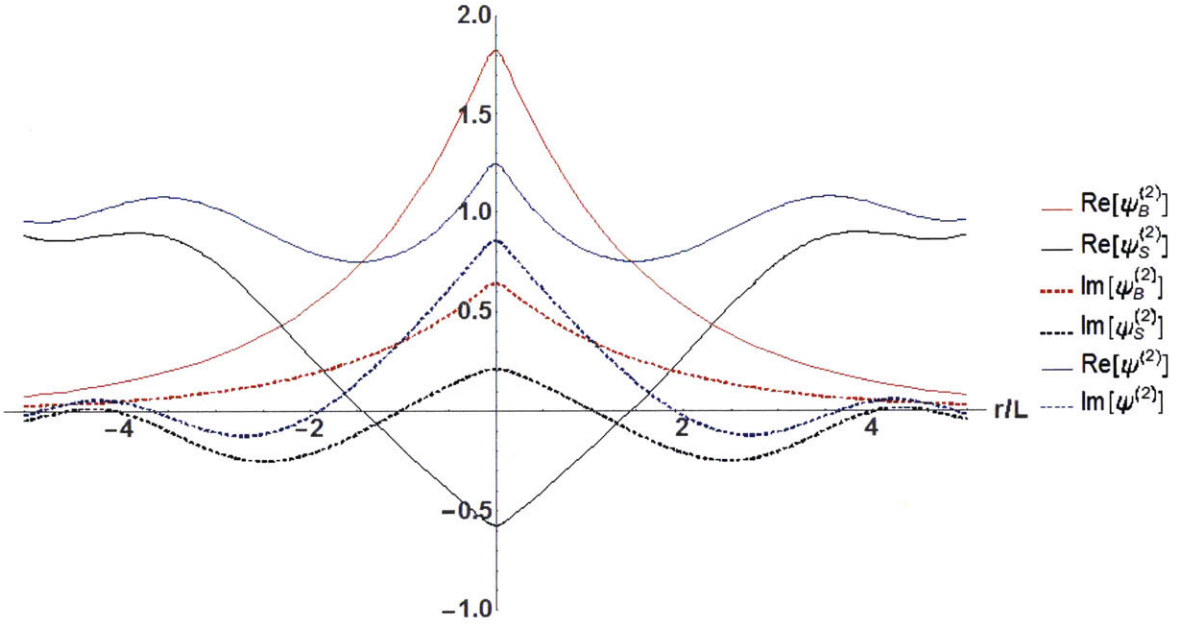

Figure 7-2: **The real (solid) and imaginary (dashed) parts of the two-photon wavefunction $\psi^{(2)}$ (blue), $\psi_B^{(2)}$ (red) and $\psi_S^{(2)}$ (black) with parameters $OD = 22$, $\Omega_c = 2\pi \times 10$MHz and $\Delta = 2\pi \times 14$MHz, by analytically solving Eq. 6.24 with a square well of width $2r_B$.** The horizontal axis is the relative coordinate r, in the unit of the medium length $L = 4.2\sigma_a$.

scattering states will destructively interfere and play very little role in the total wavefunction. As shown in Fig. 7-3, increasing OD and L by a factor of 10 leads to a wavefunction that resembles the bound state wavefunction until it decays to a very small value. At larger r, the amplitude of the wavefunction gradually goes to 1, as expected for two photons separated by more than the length of the medium, or rather, never in the medium simultaneously. Within the extent of the bound state wavefunction, the phase is flat, and then reduced to zero, for the same reason as the amplitude goes to 1. Therefore, in the long medium limit, the width of the phase feature is the same as the width of the amplitude of the bound state wavefunction or twice the width of $g^{(2)}$. For a finite medium, before $\psi_S(R = L, r)$ vanishes, as the amplitude of the bound state decreases with increasing photon separation, the scattering states' contribution continuously increases. Hence, the phase gradually drops to zero without a flat region. It is worth noting that compared to a usual δ-function well, here we need to be careful that the mass can be varied with the parameters in addition to the potential, and therefore increasing OD_B does not have the same effect as increasing OD while keeping OD/L constant.

Last, as established in Sec. 6.3, we always work in a low input photon rate regime, and model the $g^{(2)}$ numerator with the two-photon component and the denominator with one-photon component. The one-photon probability amplitude is considered a trivial number. The nontrivial dynamics is only in the two-photon sector where the strong nonlinear interaction creates new frequencies and correlations. We will use a similar model for the three-photon correlations. $g^{(3)}$ is directly connected to the three-photon probability amplitude with a trivial denominator determined solely by the one-photon sector.

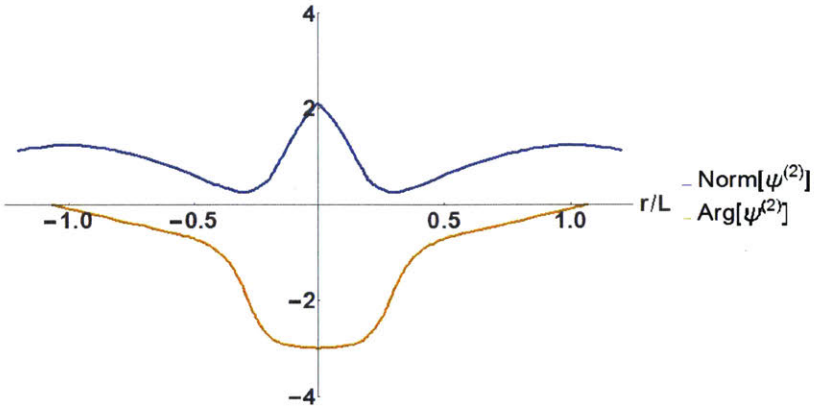

Figure 7-3: **The amplitude (blue) and phase (yellow) of the two-photon wavefunction $\psi^{(2)}$ in a medium that is 10 times as long as in the real experiment, by analytically solving Eq. 6.24 with a square well.** $OD = 10 \times 22$, $\Omega_c = 2\pi \times 10\text{MHz}$ and $\Delta = 2\pi \times 14\text{MHz}$. The horizontal axis is the relative coordinate r, in the unit of the medium length $L = 4.2\sigma_a = 4.2 \times 36\mu m$.

7.2 Experimental setup for the observation of the three-photon bound state

The ^{87}Rb atoms are loaded form a 3D magneto-optical trap (MOT) into a 1064nm crossed dipole trap. The dipole trap is modulated with a period of 40 μs and 80% duty cycle. A $\sim 6\mu s$ long probe pulse is sent to the atomic cloud while the dipole trap is off to avoid inhomogeneous AC Stark shift. The modulation of the trap and therefore the measurements last for 120ms before a new atomic cloud is loaded. The average resonant optical depth along the atomic cloud is 39. The root-mean-square (rms) length of the medium is $32\mu m$. The blockade radius r_B defined as $(C_6 \frac{4|\Delta|}{\Omega_c^2})^{\frac{1}{6}}$ is 20 μm, where C_6 is the van der Waals coefficient. Although the Raman sideband cooling setup is implemented (and therefore the pumping beam intersects the quantization axis at an angle of $\sim 45°$), the data in this chapter are taken without Raman sideband cooling.

To investigate the quantum dynamics of three-photon states, we measure the three-photon correlation function and conditional phase. The three-photon or third-order correlation function has been measured before for coupled atom-cavity [10]

or quantum dot-cavity [35, 36] systems, as well as thermal and laser sources. Non-classical states of three photons such as the Greenberger-Horne-Zeilinger (GHZ) [94], 'N00N' [95] and W [96] state have been constructed via quantum state tomography. More recently, three-photon interference has been isolated and observed [97,98]. Here, as sketched in Fig. 7-4, we measure the three-photon correlation function by splitting the light onto three single-photon counting modules. Additionally, by mixing a detuned local oscillator (LO) into the final beamsplitter, we can also perform a heterodyne measurement, conditioned on detecting one or two photons with the other two detectors. We switch from the polarization reference to a detuned local oscillator, because the latter approach has the advantage of directly accessing the nonlinear phase that interests us, without reconstructing the full density matrix. This greatly reduces the amount of measurements, which is an obstacle when scaling up the number of particles in the system.

The first two beamsplitters are polarizing beamsplitters (PBS), and the last one is a 8:92 pellicle beamsplitter to minimize loss of the probe photons. There are polarization optics before the first PBS to clean up the polarization of the probe, after which a half-wave plate is placed before each PBS to balance the detection rates on the three detectors. None of the polarization optics are shown in Fig. 7-4. Since we only detect one output port of the pellicle beamsplitter, the intensity noise cannot be cancelled as in a balanced detection. Therefore, we have to make a comprise, and the counts from the LO is kept about four times of that from the probe on detector D_3.

The 79MHz frequency difference between the local oscillator (LO) and the probe is generated by an acousto-optic modulator (AOM). The probe is derived from the -1st order of the AOM, and LO does not pass any AOM. Afterwards, the two beams are sent through their own optical fibers. In order to take out the decoherence caused by the fibers, we beat the probe and LO. The beat note of probe and LO is sent to a digital delay generator (SRS DG645) to produce the trigger for SPCMs, which serves as a time zero for each probe pulse. We use 79MHz because the delay generator does not respond to a signal faster than 80MHz. Unlike the probe, the LO does not propagate

through the atomic cloud, causing a phase drift on a time scale of tens of milliseconds. The remaining phase drift is taken care of in the data analysis, documented in detail in Appx C. In short, we keep track of the phase drift by fitting the unconditional phase for each time interval of $\sim 10ms$. The interpolation of this time-dependent unconditional phase is subtracted from each detection event on detector D_3 (phase measurement). In other words, after the subtraction, unconditional phase shift is zero, and conditional phase shift is referenced to the unconditional phase shift–including the drift and linear phase shift of the medium. After taking care of the drift, the conditional phase measurements can be averaged over hours.

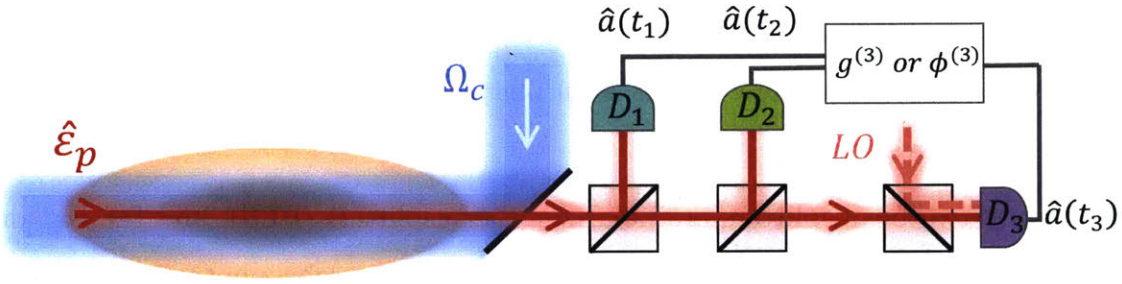

Figure 7-4: **Setup of the three-photon correlation function and conditional phase measurements.** The atoms are optically pumped into the hyperfine (F) and magnetic (m_F) sublevel $|g\rangle = |5S_{1/2}, F = 2, m_F = 2\rangle$ in the presence of a 3G magnetic field along the quantization axis, which is defined by the common propagation direction of the probe and control beams along the long axis of the cloud. The weak coherent probe light is coupled to the Rydberg state, via an intermediate state $|e\rangle = |5P_{3/2}, F = 3, m_F = 3\rangle$, of linewidth $\Gamma/2\pi = 6.1MHz$, by means of a control field that is detuned by Δ below the resonance frequency of the upper transition, $|e\rangle \rightarrow |r\rangle = |100S_{1/2}, J = 1/2, m_J = 1/2\rangle$. Strong interactions between probe photons are detected via photon correlation functions of the transmitted light, which is split onto three single-photon detectors with equal intensities by manipulating the polarization optics before the polarizing beamsplitters. To perform phase measurements, a local oscillator 79 MHz blue detuned from the probe laser is mixed into detector D_3.

To produce the unconditional phase measurement in Fig. 7-6(a), we turn off the dipole trap after modulation and allow the atomic cloud to expand for 1ms. We measure the unconditional phase after the expansion of the cloud for 4ms and use it as the reference for the phase during the last 5ms of modulation. The sequence is

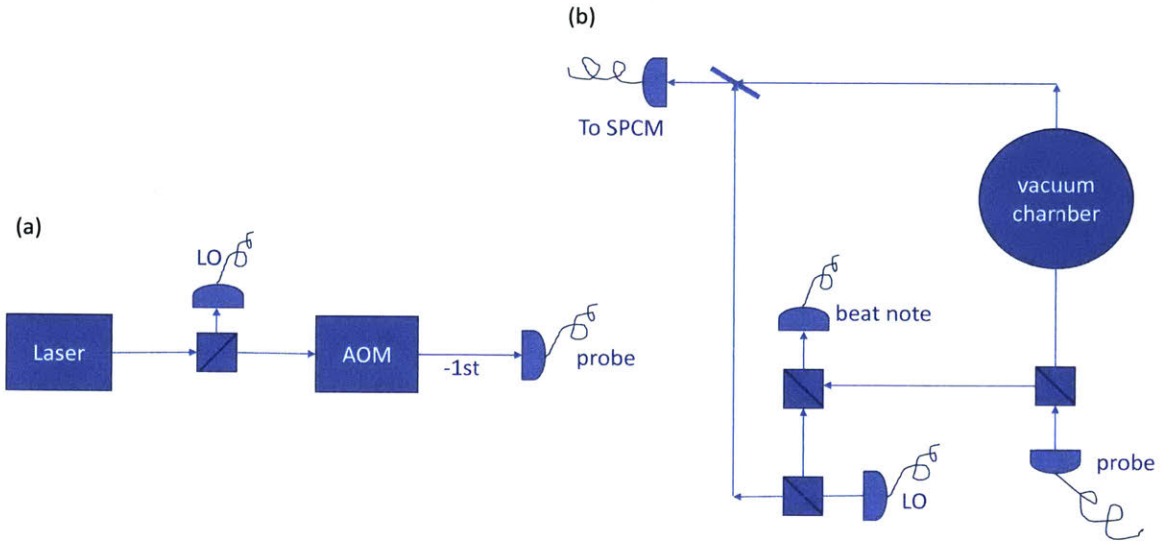

Figure 7-5: **The sketch of the probe and LO beam paths. (a)** Beam preparation on a separate table from the vacuum chamber. **(b)** LO and probe are fiber-coupled to the optical table where the vacuum chamber sits. LO does not go through the vacuum chamber. A beat note is derived before the probe is attenuated to the single-photon level and is used to trigger SPCMs. The probe and LO is combined with a 8:92 pellicle beamsplitter to minimize loss of the probe photons.

adjusted such that during this 5ms, the average optical depth is the same as a usual sequence.

The rate-dependent $\phi^{(1)}$ in Fig. 7-6(b) is generated by alternating relatively strong and weak (input photon rate of $0.5\mu s^{-1}$) pulses. The weak pulse serves as the phase reference, and a constant offset is applied to all the points such that the linear fit crosses the origin.

7.3 Evidence of the three-photon bound state: intensity correlation functions

To isolate dispersive (force-induced) from dissipative (loss-induced) effects, we work at large detuning $\Delta \geq 3\Gamma$ from atomic resonance (Γ is the population decay of the $5P_{3/2}$ state, and at a two-photon detuning where the transmission through the medium is the same with and without EIT while the phase differs significantly (Fig. 7-6(a)).

Consequently, the transmission hardly varies with probe intensity (Fig. 7-6(b) top), while a strongly nonlinear phase with a slope of 0.40(7) rad·μs is observed (Fig. 7-6(b) bottom).

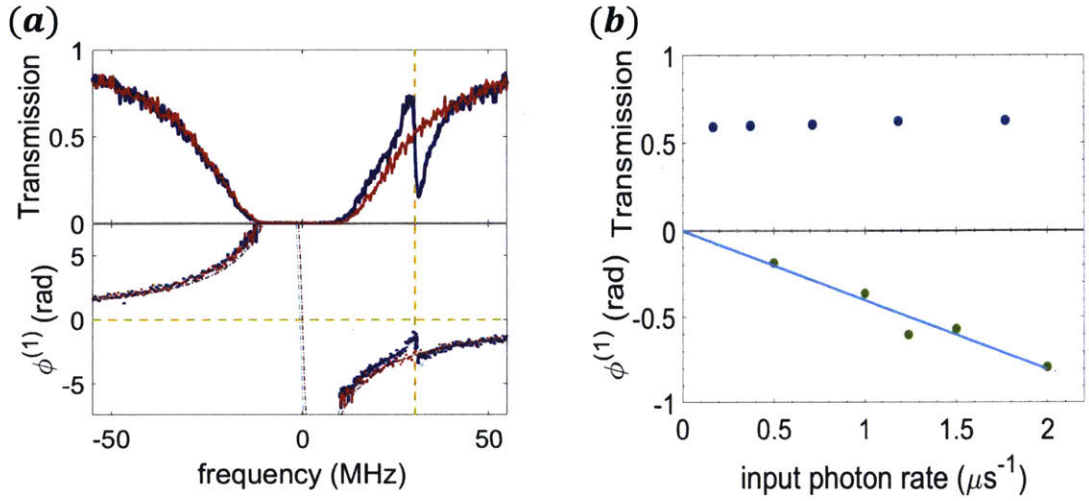

Figure 7-6: **Transmission and unconditional phase. (a)**, Transmission (top) and unconditional phase $\phi^{(1)}$ (bottom) as a function of probe frequency measured at a low ($0.5\mu s^{-1}$) input photon rate. The blue and red data are from measurements with and without control beam, respectively. The blue and red dashed lines in the bottom graph are theoretical expectation. The vertical yellow dashed line marks EIT resonance. **(b)**, Rate dependence of transmission (top) and unconditional phase (bottom) on two-photon resonance $|g\rangle \rightarrow |r\rangle$, with a one-photon detuning of $\Delta = 30$MHz. While the transmission is rate-independent, the phase is rate dependent (slope is 0.4 rad$*\mu s$), indicating a strong dispersive nonlinearity.

To analyze our observations, we consider the output state in the following form, we write the output state as follows assuming the state stays pure and ignoring higher photon number Fock state:

$$|\psi\rangle = |0\rangle + \int dt_1\, \psi_1(t_1)|t_1\rangle + \int dt_1 dt_2\, \psi_2(t_1,t_2)|t_1,t_2\rangle + \int dt_1 dt_2 dt_3\, \psi_3(t_1,t_2,t_3)|t_1,t_2,t_3\rangle, \tag{7.8}$$

where $|t_1,\cdots,t_N\rangle = \frac{1}{N!}a^\dagger(t_1)\cdots a^\dagger(t_N)|0\rangle$ and $a^\dagger(t)$ is the creation operator of the time bin mode t. The correlation functions can be related to the wavefunctions as

$$g^{(2)}(t_1,t_2) = \quad = \frac{|\psi_2(t_1,t_2)|^2}{|\psi_1(t_1)|^2|\psi_1(t_2)|^2} \tag{7.9}$$

and

$$g^{(3)}(t_1, t_2, t_3) = \frac{|\psi_3(t_1, t_2, t_3)|^2}{|\psi_1(t_1)|^2|\psi_1(t_2)|^2|\psi_1(t_3)|^2} \tag{7.10}$$

where the last equality in both the two equations is valid in the low rate limit.

The experimentally measured $g^{(3)}$ function, plotted in Fig. 7-7(a), (b), displays a clear bunching feature: the probability to detect three photons within a short time of one another is six times as likely as for non-interacting photons in a laser beam. The increase at $t_1 = t_2 = t_3$ is accompanied by a depletion region for photons arriving within $\sim 0.7\mu s$ of one another, particularly visible along the lines of two-photon correlations $t_i = t_j \neq t_k$ in Fig. 7-7(a): This depletion region is caused by the inflow of probability current towards the center $t_1 = t_2 = t_3$.

Figure 7-7(b) compares the binding between two photons separated by time τ ($g^{(2)}(t, t+|\tau|)$) to the binding of one photon to two other coincident photons ($g^{(3)}(t, t, t+|\tau|)$). The trimer feature (fitted decay time $\tau_3 = 0.14\mu s$) is approximately twice narrower than the dimer feature (fitted decay time $\tau_2 = 0.31\mu s$), showing that the interaction between a photon and a dimer is two times stronger than the interaction between two single photons.

Figure 7-7(c) illustrates the binding of a third photon to two photons that are detected with a time separation T. If T exceeds the dimer time scale τ_2, then the third photon binds independently to the other photons, while for $T < \tau_2$ the two peaks merge into a single, more tightly bound trimer. This is analogous to the binding of a particle to a double-well potential as the distance between the wells is varied. For large T, as shown in (iii), where the two conditioning photons are uncorrelated, we expect the decay rate of the two peaks to be the same as $g^{(2)}$. This is verified to be true within the error bars.

To quantitatively model these results, we resort to an effective field theory [99], which is a lot easier to generalize to N photons than the Schrödinger equation used previously for the two-photon bound state. we describe our system by a slow-light

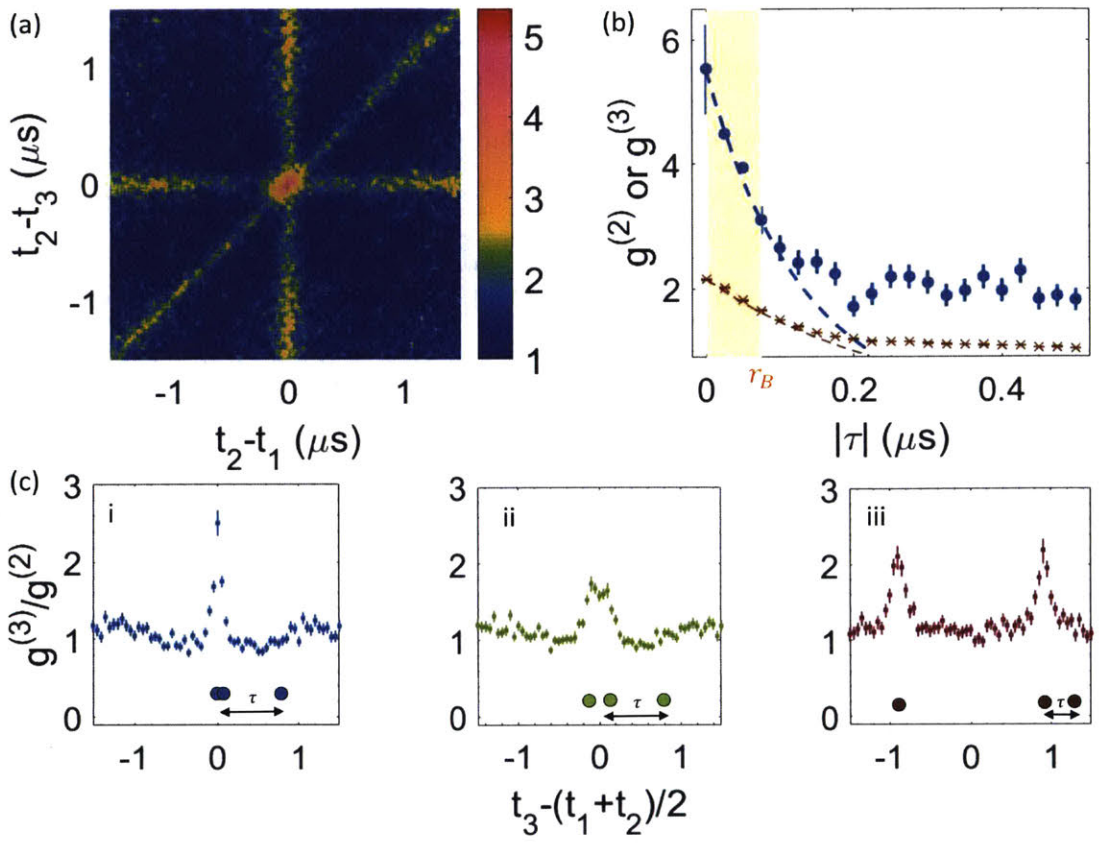

Figure 7-7: **Photon correlation functions measured at one-photon detuning $\Delta = 2\pi \times 30$MHz, control Rabi frequency $\Omega_c = 2\pi \times 10$MHz, input photon rate of $1\mu s^{-1}$ and on EIT resonance.** **(a)**, Two dimensional representation of three-photon correlation function $g^{(3)}(t_1, t_2, t_3)$, with t_i being the photon detection time at detector D_i. Three-photon bunching corresponds to the central region, two-photon bunching to the stripes. **(b)**, $g^{(3)}(t, t, t + |\tau|)$ (blue data points) and $g^{(2)}(t, t + |\tau|)$ (brown data points). The decay rates of the dashed lines come from an ab-initio calculation with inputs from independently measured parameters such as the control Rabi frequency, the optical depth, etc. They are scaled to match the amplitudes of data. The decay rate of $g^{(3)}$ is a factor of 2 faster than that of $g^{(2)}$ from the calculation, showing that a photon is more strongly bound to two photons than to one. $g^{(3)}(t, t, t + |\tau|)$ is the average of the cuts along the lines where two photons are within $25ns$ of each other, with τ being the interval of the mean arrival time of these two conditioning photons and the third photon. The fitted time constants are $\tau_3 = 0.14\mu s$ and $\tau_2 = 0.31\mu s$ for $g^{(3)}$ and $g^{(2)}$, respectively. **(c)**, Three representative plots of $g^{(3)}(t_1, t_2, t_3)/g^{(2)}(t_1, t_2)$ for fixed $|t_1 - t_2| = 0\mu s$ (i), $|t_1 - t_2| = 0.2\mu s$ (ii), and $|t_1 - t_2| = 1.8\mu s$ (iii), within a 50ns window. As we condition on the two photons being further and further away, the sharply decaying $g^{(3)}$ function transitions to a slower decaying $g^{(2)}$ function. For intermediate time separations (ii), there is interference between all states including the dimer and trimer. All permutations of the detectors are used to generate the data in (b),(c).

Hamiltonian density with a contact interaction,

$$\mathcal{H} = -\hat{\psi}^\dagger \left(i\hbar v_g \partial_z + \frac{\hbar^2}{2m}\partial_z^2 \right) \hat{\psi} - \frac{\hbar^2}{ma}\hat{\psi}^{\dagger 2}\hat{\psi}^2, \tag{7.11}$$

where v_g is the medium group velocity, $m = -\hbar\Omega_c^2/(8\Delta v_g^2)$ is the effective photon mass, $a = \frac{2^{\frac{25}{6}}\cdot 3}{\pi}\frac{1}{r_B}(\frac{\Delta}{\Gamma})^2(\frac{L}{OD})^2$ is the scattering length, Ω_c is the control laser Rabi frequency, and Δ is the one-photon detuning, in a one-dimensional homogenous medium where the nonlinear phase a photon would pick up is smaller than π. $\hat{\psi}$ is a quantum field annihilation operator, which corresponds to a photon outside the medium and a Rydberg polariton inside. $\mathcal{H}$ supports both bound states and scattering states. The bound states can be determined from the Bethe ansatz solution to $\mathcal{H}$, resulting in the correlation functions $g^{(3)}(t_1, t_2, t_3) \propto e^{-\frac{|t_1-t_2|}{a/(2v_g)}} e^{-\frac{|t_2-t_3|}{a/(2v_g)}} e^{-\frac{|t_1-t_3|}{a/(2v_g)}}$ and $g^{(2)}(t_1, t_2) \propto e^{-\frac{|t_1-t_2|}{a/(2v_g)}}$.

If we consider $t_1 = t_2 = t$ as before we see that $g^{(3)}(t, t, t+|\tau|) \propto e^{-2|\tau|/\tau_0}$. In this case, a telltale sign of a three-photon bound state emerges, namely that the width of $g^{(3)}$ is half that of $g^{(2)}$ computed from the same data. We find $a/(2v_g) = 0.32\mu s$ from an ab-initio calculation and plot it along the data (Fig. 7-7(b), dashed lines). The three-photon bound state solution, which features a two times smaller time constant than the two-photon bound state, agrees with the data well for small $|\tau|$.

The insight about the two-photon bound state in Sec. 7.1 still holds true for the three-photon bound state. The depletion region $\tau \sim 0.5\mu s$ arises from a inward probability current of photons towards each other. Since the length of the medium is finite, photons that are never together inside the medium remain uncorrelated, and $g^{(3)}$ rise would be observed again. If the medium were infinitely long, we would just see the soliton-like bound state. The initial state is decomposed to the bound state and the continuum of scattering states [19] following the quantum quench (entry of the medium). The composite structure observed in the experiment can be interpreted as a quantum interference between the bound state and scattering states. Due to the initial decomposition and the destructive interference, the contribution from the scattering states is small when all photons are detected near to each other, i.e. the

bound state dominates the $g^{(3)}$ function near $\tau = 0$. The dimer binding energy can be estimated as $-\frac{\hbar^2}{ma^2}$=0.1MHz, and the trimer binding energy is four times larger. They are about 10^{10} times smaller than diatomic molecules such as NaCl and H_2, and similar to Efimov trimers in refs. [100, 101].

7.4 Three-photon conditional phase

The dispersive and distance dependent photon-photon interaction also manifests itself in the phases of the wavefunctions. We refer the phase of N-photon wavefunction as N-photon phase, namely, $\phi^{(1)}(t_1) = \arg[\psi_1(t_1)]$, $\phi^{(2)}(t_1, t_2) = \arg[\psi_2(t_1, t_2)]$ and $\phi^{(3)} = \arg[\psi_3(t_1, t_2, t_3)]$. We perform the measurement of three-photon phase by conditioning on detecting probe photons at times t_1 and t_2 on detector D_1 and D_2 and a heterodyne measurement at time t_3 on detector D_3.

Suppose the LO is a strong classical field and the last beamsplitter in Fig. 7-8 has full transmission of the light from the probe field. Then the conditional phase measurement can be written as

$$\langle \psi, 0, 0 | \hat{b}^\dagger(t_1) \hat{b}(t_1) \hat{c}(t_2)^\dagger \hat{c}(t_2) \hat{p}(t_3) | \psi, 0, 0 \rangle \tag{7.12}$$

where $\hat{b}(t)$, $\hat{c}(t)$ and $\hat{p}(t)$ are the annihilation operators of the spatial modes labeled as in Fig. 7-8 at time t. $|\psi, 0, 0\rangle$ denotes the joint states of the output of the probe after propagation in the medium and the two vacuum states mixed into the first two beamsplitters. Applying the unitary transformation of the beamsplitter defined in Eq. 2.17, Eq. 7.12 is proportional to

$$\langle \psi, 0, 0 | \hat{a}^\dagger(t_1) \hat{a}^\dagger(t_2) \hat{a}(t_3) \hat{a}(t_2) \hat{a}(t_1) | \psi, 0, 0 \rangle = \psi_3(t_1, t_2, t_3) \psi_2^*(t_1, t_2) \tag{7.13}$$

The phase of this measured quantity is $\phi^{(3)}(t_1, t_2, t_3) - \phi^{(2)}(t_1, t_2)$. We can extract $\phi^{(2)}(t_1, t_2)$ from the same data by conditioning on detecting one probe photon, assuming the results are independent of which detector is in use. Then $\phi^{(3)}$ and $\phi^{(2)}$ are referenced to three and two uncorrelated photons, respectively. More specifically, the two-

photon phase reference is $\phi^{(2)}_{ref} \equiv \phi^{(2)}(t_1, t_2 \to \infty) = \phi^{(1)}(t_1) + \phi^{(1)}(t_2)$, and the three-photon phase reference $\phi^{(3)}_{ref} \equiv \phi^{(3)}(t_1, t_2, t_3) \xrightarrow{|t_i - t_j| \to \infty} \phi^{(1)}(t_1) + \phi^{(1)}(t_2) + \phi^{(1)}(t_3)$, for any $i \neq j$. $\phi^{(3)}(t, t, t + |\tau|)$ at large $|\tau|$ asymptotically goes to $\phi^{(2)}(t, t)$, because $\phi^{(3)}(t, t, t + |\tau|) - \phi^{(3)}_{ref} \xrightarrow{|\tau| \to \infty} \phi^{(2)}(t, t) + \phi^{(1)}(t + |\tau|) - \phi^{(3)}_{ref} = \phi^{(2)}(t, t) - \phi^{(2)}_{ref}$, where the last equality makes use of the fact that the phase does not depend on the absolute time. In other words, $\phi^{(1)}$ is time independent, and $\phi^{(2)}$ ($\phi^{(3)}$) only depends on the time interval(s). The phase references are not explicitly written out elsewhere.

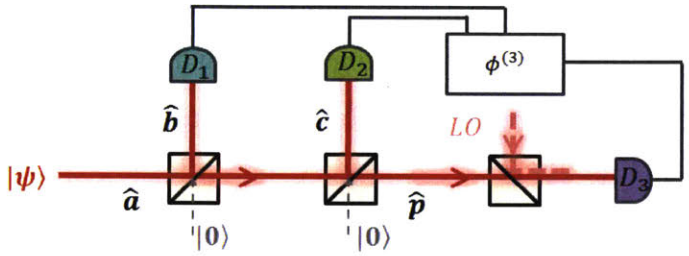

Figure 7-8: **Conditional phase measurements setup.** $\hat{a}(t)$, $\hat{b}(t)$, $\hat{c}(t)$ and $\hat{p}(t)$ are the annihilation operators at time t of the corresponding input and output ports of the first two beamsplitters.

We observe a large conditional phase shift $\phi^{(3)}(t, t, t + |\tau|)$ for the trimer near $\tau = 0$ (Fig. 7-9(a)) that is significantly larger than the dimer phase shift $\phi^{(2)}(t, t+|\tau|)$ (Fig. 7-9(b)). This confirms the stronger interaction between a photon and a dimer compared to that between one photon and another. $\phi^{(3)}(t, t, t+|\tau|)$ at large $|\tau|$ carries the phase of the two simultaneous conditioning photons. Thus, it has the same value as the initial two photon phase $\phi^{(2)}(t, t)$. Qualitatively, the widths of the phase feature is twice of the corresponding $g^{(N)}$ feature. As the bound state wavefunction amplitude becomes smaller the contribution of the scattering states sets in, which reduces the magnitude of the phase. Therefore, the widths of the phase feature roughly reflect the widths of the wavefunction, which is twice the width of $g^{(N)}$, $N = 2, 3$.

The Hamiltonian of Eq. 7.11 predicts that $\phi^{(3)}$ ($\phi^{(2)}$) equals the product of the trimer (dimer) binding energy times the propagation time in the medium, for the contribution from the bound state only. Thus from the bound state contributions one would expect a ratio $\phi^{(3)}/\phi^{(2)} = 4$, independent of the atom-light detuning Δ. While the observed ratio is approximately constant (Fig. 7-10), it is smaller than

4 due to two contributions of comparable magnitude. One correction arises from scattering states, or equivalently, from the fact that our Rydberg medium ($\sim 80\mu m$) is of the size as the two-photon bound state ($\sim 140\mu m$). The other, more intriguing correction is due to an effective three-photon force that is not the sum of pairwise interactions. Namely, when all three photons are within one blockade radius of one another, there can be only one Rydberg excitation and the potential cannot get deeper compared to two photons [99, 102]. This saturation effect appears as an additional repulsive force that reduces the trimer binding energy. Another small correction comes from the fact that we make measurements at finite photon rate such that at finite detection efficiency there are contributions from more than three (two) photons when we measure $\phi^{(3)}(\phi^{(2)})$.

The EFT in Fig. 7-10 employs the dipolariton field method to find the value of the effective three-body forces that matches the physical scattering amplitudes in the microscopic model. It takes into account the finite medium, and compares the results with and without the repulsive three-photon force. The deviation of the latter from the ratio 4 reflects the role of the finite medium. In case of a short medium, compared with the length of the bound state, one expects the ratio to be 3, consistent with the conventional Kerr medium [82]. Including the three-photon force allows the ratio to go below 3, resulting in better agreement with the data. This deviation from 3 predominantly arises from the effect of the three-photon force on the interaction between scattering states in the system. There is an additional correction to the binding energy of the trimer that contributes to this deviation, but this correction is suppressed due to the distributed nature of the trimer compared to the microscopic range of the interactions. The lower bound 2 of the ratio stems from a fully saturated medium, where the interaction potential does not increase with the photon number.

Last, I will show more details about our phase reference. we use the average value when all photons are far away from each other as the phase reference and interpret it as the sum of linear phase $\phi^{(1)}$. Alternatively, the unconditional phase can be regarded as $\phi^{(1)}$ as well. Figure 7-11 presents the same data as in Fig. 7-9, with unconditional phase as the reference instead. Although at large $|\tau|$, both conditional

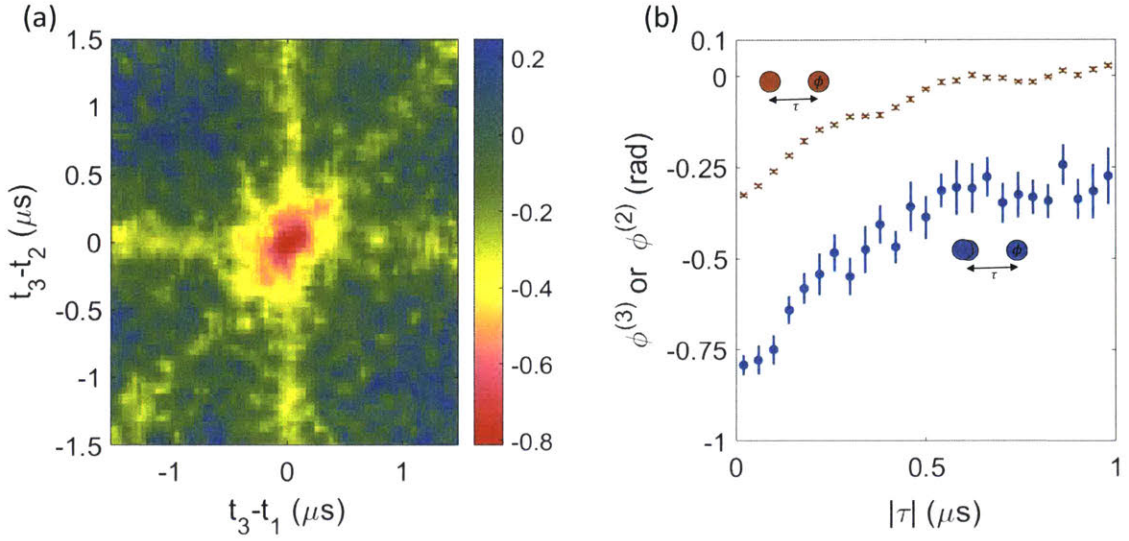

Figure 7-9: **Nonlinear phase measured at identical conditions as the data in Fig. 7-7. a**, Conditional phase $\phi^{(3)}(t_1, t_2, t_3)$, where t_1 and t_2 correspond to photon detection events at detectors D_1, D_2, and a heterodyne measurement is performed on detector D_3 at time t_3. **(b)**, Diagonal cut $\phi^{(3)}(t, t, t+|\tau|)$ (blue), with the two conditioning probe photons within $40ns$ of each other, and $\phi^{(2)}(t, t+|\tau|)$ (brown) showing a large photon phase when conditioning on two other near-simultaneous photons ($\phi^{(3)}$) than on one near-simultaneous photon ($\phi^{(2)}$). $\phi^{(3)}$ and $\phi^{(2)}$ are referenced to three and two uncorrelated photons, respectively. More specifically, the two-photon phase reference is $\phi^{(2)}_{ref} \equiv \phi^{(2)}(t_1, t_2 \to \infty) = \phi^{(1)}(t_1) + \phi^{(1)}(t_2)$, and the three-photon phase reference $\phi^{(3)}_{ref} \equiv \phi^{(3)}(t_1, t_2, t_3) \xrightarrow{|t_i - t_j| \to \infty} \phi^{(1)}(t_1) + \phi^{(1)}(t_2) + \phi^{(1)}(t_3)$, for any $i \neq j$. $\phi^{(3)}$ at large $|\tau|$ asymptotically goes to $\phi^{(2)}(t, t)$, because $\phi^{(3)}(t, t, t+|\tau|) - \phi^{(3)}_{ref} \xrightarrow{|\tau| \to \infty} \phi^{(2)}(t, t) + \phi^{(1)}(t+|\tau|) - \phi^{(3)}_{ref} = \phi^{(2)}(t, t) - \phi^{(2)}_{ref}$, where the last equation makes use of the fact that the phase does not depend on the absolute time. In other words, $\phi^{(1)}$ is time independent, and $\phi^{(2)}$ ($\phi^{(3)}$) only depends on the time interval(s). The phase references are not explicitly written out elsewhere.

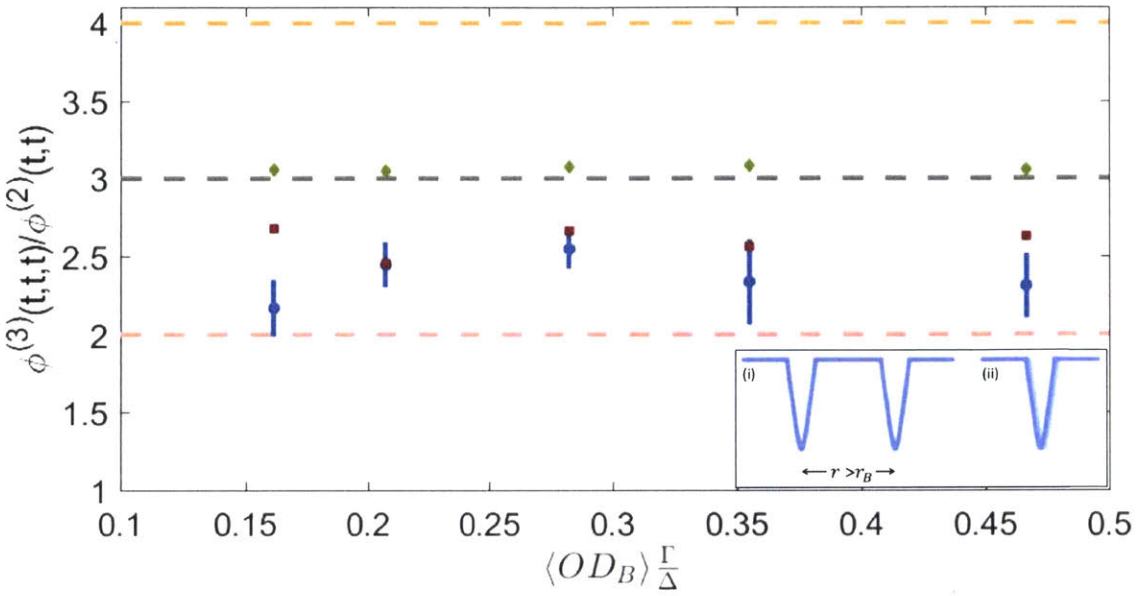

Figure 7-10: **Measured ratio of $\phi^{(3)}(t,t,t)/\phi^{(2)}(t,t)$ (blue) and the EFT predictions (with the three-photon force in brown; without in green) as a function of $\langle OD_B \rangle \frac{\Gamma}{\Delta}$, where $\langle\rangle$ refers to the average over the Gaussian profile of the atomic density.** The control Rabi frequency $\Omega_c = \{22,18,10,10,8\}$ MHz for $\Delta = \{54,42,30,24,18\}$ MHz is chosen such that the transmission is insensitive to the input photon rate (Fig. 7-6). We also change the input photon rate $\{0.7, 1, 1, 1.3, 2.5\}$ photons/μs to achieve similar data acquisition rates since the losses are larger at smaller detunings. Finally, the bin sizes are $\{75, 75, 40, 100, 65\}$ns. All the three (for $\phi^{(3)}$) or two (for $\phi^{(2)}$) detections are within one bin size of each other. From a fully saturated medium, one expects $\phi^{(3)}/\phi^{(2)} = 2$; for bound states in a long medium and no three-photon force, one expects $\phi^{(3)}/\phi^{(2)} = 4$ (see text). EFT is calculated with parameters from independent measurements, and the two-photon detuning is the only parameter varied within the experimental uncertainty to fit the two-photon phase. The inset illustrates the potential the third photon would see induced by the other two photons. (i) When the two photons are separated by more than a blockade radius, each of them creates a potential; (ii) When the two photons are within one blockade radius, since there can be at most one Rydberg excitation, the potential is not deeper than that created by one photon. Therefore, we overestimate the attractive potential by considering pairwise interaction only, and a repulsive three-body force is required to make the correction.

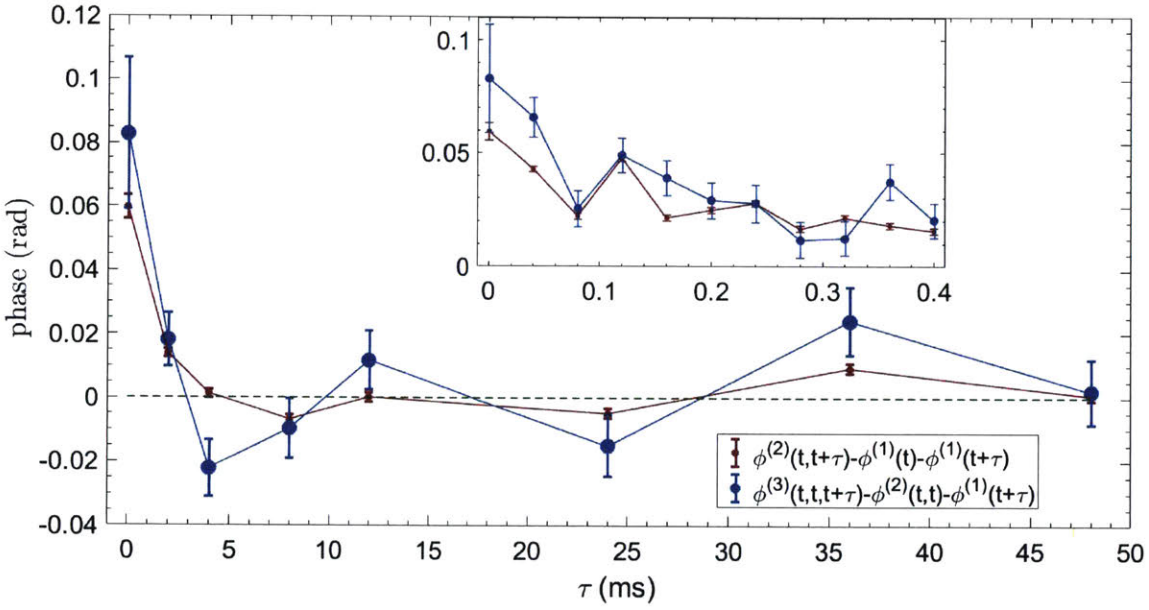

Figure 7-11: **The long range behavior of the conditional phase referenced to the local unconditioned phase.** The blue and brown data represent $\phi^{(3)}(t,t,t+\tau)-\phi^{(2)}(t,t)-\phi^{(1)}(t+\tau)$ and $\phi^{(2)}(t,t+\tau)-\phi^{(1)}(t)-\phi^{(1)}(t+\tau)$, respectively. The inset shows the same quantities at a shorter time scale. These data with τ much longer the probe pulse ($\sim 6\mu s$) are generated by taking detection events from different pulses.

phases are expected to go to 0, there is nevertheless small disagreement between the unconditional phase and the conditional phase with well separated photons. The conditional phases vary at a time scale of a few tens of microseconds, much slower than the bound state physics. Additionally, the mismatch is only less than 20% of the phase of the concurrent photons. Therefore, we do not believe the phase offset at large τ to have significant impact on our main results.

7.5 Control Rabi frequency dependence

At the beginning of Sec. 7.3, I point out we work under the condition that with and without the control laser, the transmission of the probe is the roughly the same. The two cases represent the photon pairs outside and inside the potential well, respectively. By matching the transmission, we minimize the nonlinear absorption.

Here, I will show how the nonlinear absorption affects our result by varying the control Rabi frequency Ω_c. With finite decoherence γ_{gr}, the transmission with the control laser increases as Ω_c increases. Therefore, for large Ω_c, photon pairs at the vicinity of each other (small $|\tau|$) has lower transmission than single photons, resulting in antibunching, and vice versa. As shown in Fig. 7-12, $g^{(2)}$ dramatically changes from bunching to antibunching as Ω_c gets bigger. Another feature in the figure is that the width of the $g^{(2)}$ feature decreases with Ω_c, because the group velocity v_g (Eq. 4.13) increases, and therefore the same distances convert to shorter times.

7.6 Input photon rate dependence

As shown in Fig. 7-6(b), the magnitude of unconditional phase increases as the input photon rate. The input photon rate is calibrated by the output rate without the atoms scaled by the detection efficiency and losses through the optics. As the rate increases, the undetected higher photon number events play a more and more significant role. Since the nonlinear phases are negative (Fig. 7-9), the "contaminated" one-photon phase becomes more and more negative.

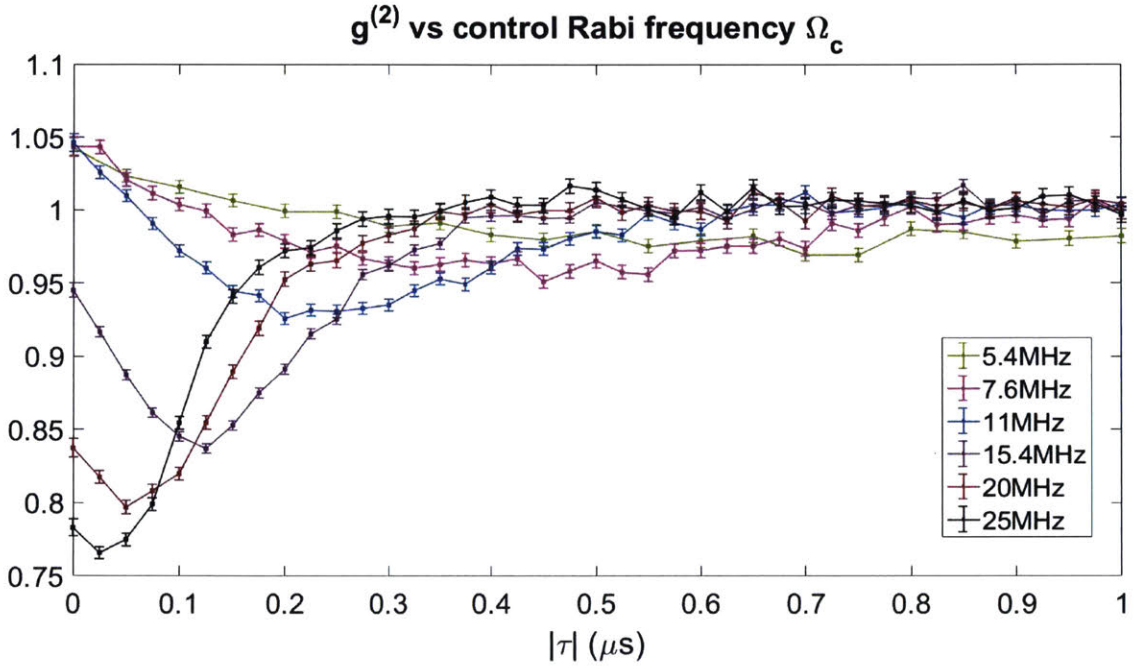

Figure 7-12: $g^{(2)}(|\tau|)$ **as a function of the control Rabi frequency** Ω_c **for one-photon detuning** $\Delta = 18$**MHz,** $OD = 45$ **and an input photon rate of** 1.1 **photons/**μs**.** Ω_c for each data is listed in the legend. All $g^{(2)}$ is normalized by dividing its own mean value when $|\tau| > 2\mu s$.

The rate dependence of the conditional phase is shown in Fig. 7-13. The magnitude of both the initial two- and three-photon phase decreases with the rate. Recall that both phases are referenced to the one-photon phase (see Sec. 7.4). The positive slope indicates that impact of the higher photon number events on the phase reference is larger than on the bare two- and three-photon phase. The fitted slopes are 0.2(0.2) and 0.6(0.2) $(rad \cdot \mu s)$ for $\phi^{(2)}(t,t)$ and $\phi^{(3)}(t,t,t)$, respectively. Hence, the contamination caused by the probe photon rate largely cancels when we plot $\phi^{(3)}(t,t,t)/\phi^{(2)}(t,t)$ in Fig. 7-10.

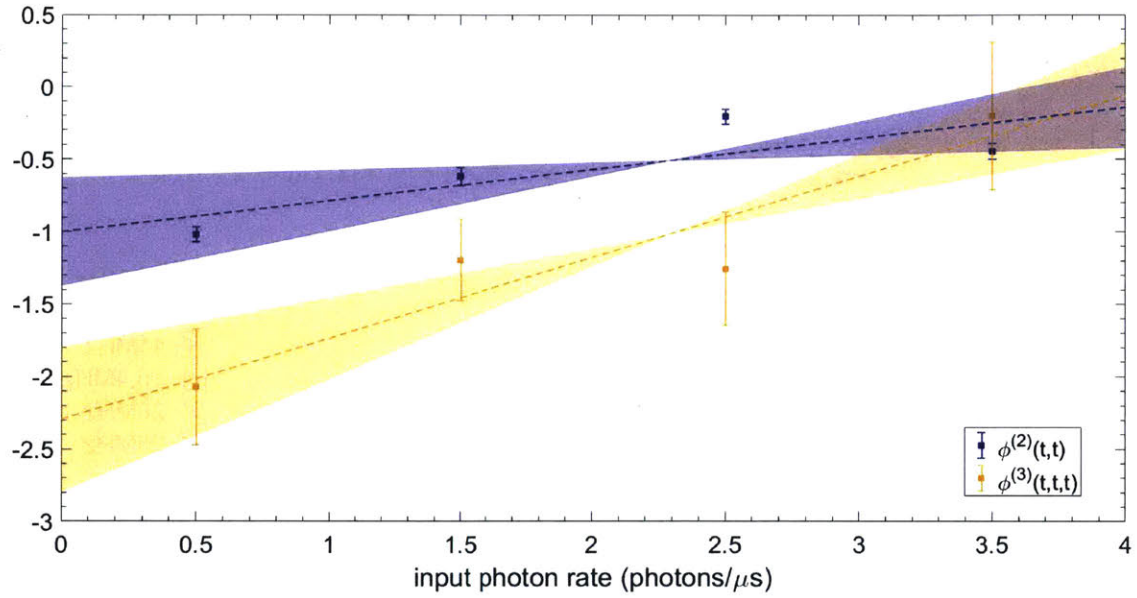

Figure 7-13: **The conditional phases of simultaneous photons as a function of the input probe rate, for one-photon detuning $\Delta = 18$MHz, $\Omega_c = 8$MHz, $OD = 40$ and on EIT resonance.** The two (three) detections for $\phi^{(2)}(t,t)$ ($\phi^{(3)}(t,t,t)$) are within 100ns of each other. The dashed lines are a linear fit of the data. The shaded areas give the 1σ range of the fitted slopes.

7.7 Summary and outlook

To conclude, we observe two- and three-photon bound states by measuring the intensity correlation functions and the conditional phase. The associated stable two- and three-photon wavepackets owing to the balance of the dispersion and the attractive

interaction can be seen as quantum solitons. Inside the medium, the propagation of the two-photon wavefunction is governed by an effective Shrödinger equation with a negative mass and positive potential, which looks like a particle with a positive mass evolving reversely in time in a potential well. This leads to a negative phase accumulated by the bound state. The measured $g^{(2)}$ and $\phi^{(2)}$ are dominated by the bound state over the scattering states.

We see photon bunching in both $g^{(2)}$ and $g^{(3)}$, manifesting the wavefunction of the bound states. The factor of 2 increase in the decay rate of $g^{(3)}(t,t,t+|\tau|)$ compared with $g^{(2)}(t,t+|\tau|)$ is predicted by the Bethe ansatz solution and verified experimentally. This feature is our key evidence of the trimer, and is robust despite the contribution from the scattering states and experimental imperfections such as the finite input photon rate. Another robust feature relatively insensitive to the finite rate is the ratio of the initial phase $\phi^{(3)}(t,t,t)/\phi^{(2)}(t,t)$. We measure roughly constant phase ratio for various parameters. The deviation from a universal ratio of 4 predicted by an effective field theory can be partially attributed to a three-photon force originating from the saturation of the Rydberg interactions.

The results in this work can be extended in a variety of other directions. First, the strong rate dependence of $\phi^{(3)}$, governed by $g^{(4)}$ and $\phi^{(4)}$, indicates the possible existence of four-photon bound states. An improvement in the detection efficiency and data acquisition rate might allow us to observe larger photonic molecules. Second, by using an elliptical or larger round probe beam and carefully engineering the mass along different directions, the system geometry can be changed to two and three dimensions, possibly permitting the observation of photonic Efimov states. Finally, an increase in the atomic density by roughly a factor of three, where another bound state appears, should result in resonant photon-photon scattering and a tunable scattering length [103].

Chapter 8

Symmetry-protected collisions

So far, we make use of Rydberg-Rydberg interaction as a mechanism to shift the Rydberg level out of the resonance, inducing a distance (between the photons) dependent level scheme. Inside the blockade radius, the probe couples to the $|g\rangle \rightarrow |e\rangle$ transition; Outside the blockade radius, together with a control laser, the probe is on EIT resonance.

On the other hand, there is another type of interaction when the pair Rydberg state is in resonance with another pair, which we call exchange interaction, as discussed in Chap. 3. In that case, it is inappropriate to talk about the shift since the interaction does not act as a perturbative shift, but mix and split the two resonant states.

In this chapter, we explore this resonant exchange interaction by colliding a propagating photon with a stored one which is coupled to a different Rydberg level using a microwave transition. Additionally, we go back to the so called dissipative regime, where the probe is resonantly coupled to the unstable intermediate state $|e\rangle$. In this regime, with the blockade shift type interaction, we observe photon antibunching caused by the increased absorption of photon pairs compared with singles, as documented in Sec. 6.1. Now, with the exchange interaction, in stark contrast, we demonstrate coherent exchange collisions between two photons that is accompanied by a $\pi/2$ phase shift, with low loss.

The effect is robust in that the value of the phase shift is determined by the

interaction symmetry rather than the precise experimental parameters, and in that it occurs under conditions where photon absorption is minimal. This phase is analogous to that acquired by a spin-1/2 particle undergoing resonant spin rotation. The half-integer value of the phase shift in units of π is protected by the symmetry of the effective Hamiltonian against variations in the experimental parameters, unlike the recently demonstrated π nonlinear phase shift based on the blockade type interaction [81] and our work in the previous chapters. The measured phase shift of $0.48(3)\pi$ is in excellent agreement with a theoretical model. These observations open a route to realizing robust single-photon switches and all-optical quantum logic gates, and to exploring novel quantum many-body phenomena with strongly interacting photons.

8.1 Experimental setup

The probe field at 780 nm is resonant with the $|g\rangle \equiv |5S_{1/2}, F = 2, m_F = 2\rangle$ to $|e\rangle \equiv |5P_{3/2}, F = 3, m_F = 3\rangle$ transition. The control field Ω_c at 479 nm couples $|e\rangle$ to $|S\rangle \equiv |100S_{1/2}, m_J = 1/2\rangle$. The microwave frequencies are 3.72, 3.67 and 11.4 GHz, respectively, to drive $100S_{1/2}$ to $99P_{3/2}$, $99S_{1/2}$ and $97S_{1/2}$. Rabi frequency $\Omega_\mu = 2\pi \times 3$ MHz is used to transfer population between Rydberg states, from $|S\rangle$ to $|P\rangle \equiv |99P_{3/2}, m_J = 3/2\rangle$. The control Rabi frequency $\Omega_c = 2\pi \times 16$ MHz. The magnetic field $B = 3$G. Each dipole trap beam has a power of 8W. The intensity is modulated with a period of $38\mu s$ with $7\mu s$ off time to probe. The atomic sample is cooled to $20\mu K$ with Raman sideband cooling.

In this experiment, probe and LO are not both on at the beginning of each gate, and their pulse shapes are very different. Therefore, probe and LO are independently controlled by their own AOM and their beat note cannot be used as a trigger for SPCMs. Instead, the SPCMs are triggered by the 79MHz DDS frequency. Meanwhile, the same signal is used to drive both probe and LO's AOM. Probe is derived from +1st order while LO from the -1st order. Therefore, LO is red detuned by 158MHz compared with probe. They are coupled through the same fiber to the vacuum chamber. The setup is sketched in Fig. 8-1. The large detuning and low power

(on the same order as the probe) ensure that the LO does not interact with the Rydberg levels, so any phase shift in the probe-LO beatnote arises from phase shifts in the probe field.

Because of the negative detuning of the LO, the positive phase shift of the beatnote shown in Figs. 8-4(a) and 8-5(a) actually corresponds to a phase lag of the probe, in agreement with the negative phase shift predicted by the solution to Eq. 8.1 for $C_3 > 0$.

There can be a very small phase drift due to the different AOM paths. In order to make fine adjustments, an extra gate is added to the end of each experimental cycle. The beat note, whose frequency is divided by a factor 64 (ADF4007) and then converted to TTL by a comparator (EVAL-ADCMP601BKSZ-ND), is read by HRMTime. The typical drift per cycle is $\lesssim 10^2$ps. These counts also help to precisely determine the frequency of the beat note.

For the two-mode measurements, we switch the AOM in the LO path to +1st order and use it as the second probe mode, since we do not perform any phase measurement with the two spatial modes. The two independently coupled probe beams are nearly overlapped on a beamsplitter before entering the chamber. Their separation (5.4 μm) is measured using a CCD camera that images the focal plane in the center of the atomic cloud. The output light is directed to two single-mode fibers by a beamsplitter. One of the fibers is aligned to each mode, allowing them to be separately detected by independent SPCMs. There is a small amount of crosstalk resulting from imperfect fiber alignment and finite separation between the modes. About 10% of the light detected in the mode A photon counter is actually from mode B, and vice versa.

8.2 Experimental sequence

We engineer collisions between polaritons coupled to two Rydberg levels $|S\rangle$ and $|P\rangle$ (Fig. 8-2(b)) using a combination of EIT and microwave manipulation between Rydberg states, in a sequence depicted in Fig. 8-3. Initially, a single photon from a weak optical *gate* pulse enters the atomic cloud and is slowed and stored in the

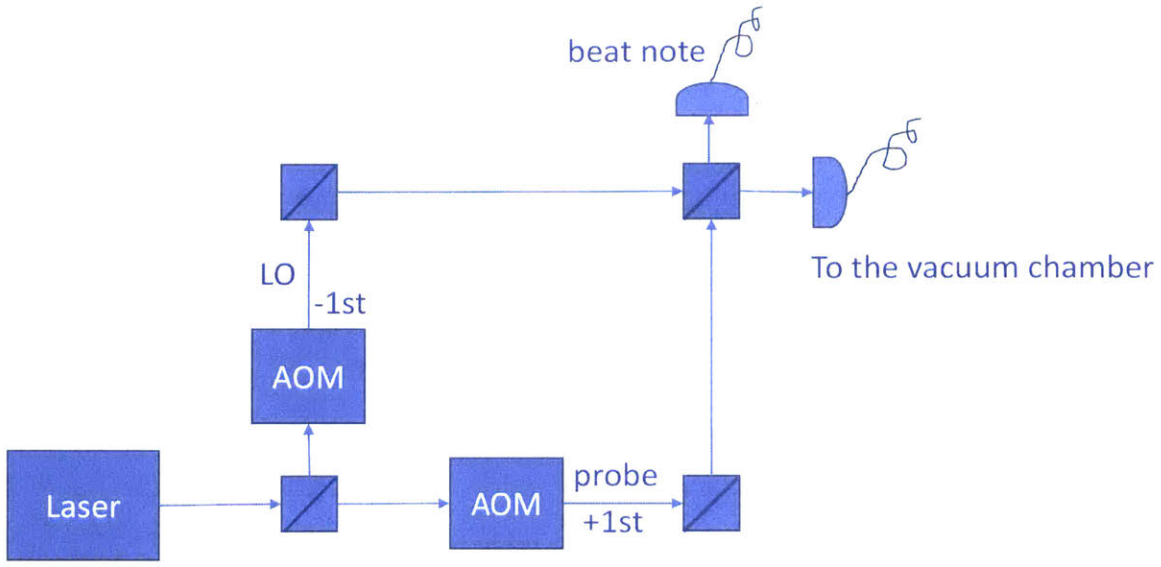

Figure 8-1: **The sketch of the probe and LO beam paths.** In the real setup, the couplers of the beat note and the beam to the vacuum chamber are very close to each other.

$|S\rangle \equiv |100S_{1/2}\rangle$ state by switching off the control field in the EIT configuration. A microwave pulse coherently converts the stored, collective $|S\rangle$ excitation to the Rydberg level $|P\rangle \equiv |99P_{3/2}\rangle$. Then, a second *signal* pulse coupled to the $|S\rangle$ state enters the medium. Since the control laser addresses only $|S\rangle$ (Fig. 8-2(b)), the polariton in $|P\rangle$ does not propagate, leading to a collision between the propagating S-state polariton and the stationary excitation in $|P\rangle$. The S-polariton ultimately leaves the cloud and is detected as a photon. Finally, the excitation stored in the $|P\rangle$ state is converted back to a propagating S-polariton (with another microwave pulse) and retrieved. The influence of polariton interactions is observed via the correlations of the transmitted signal and gate photons.

8.3 Collisions between a propagating photon and a stored photon

To observe the phase shift resulting from the interaction, we analyse the transmitted signal pulse conditioned on the detection of a retrieved gate photon. The conditioned

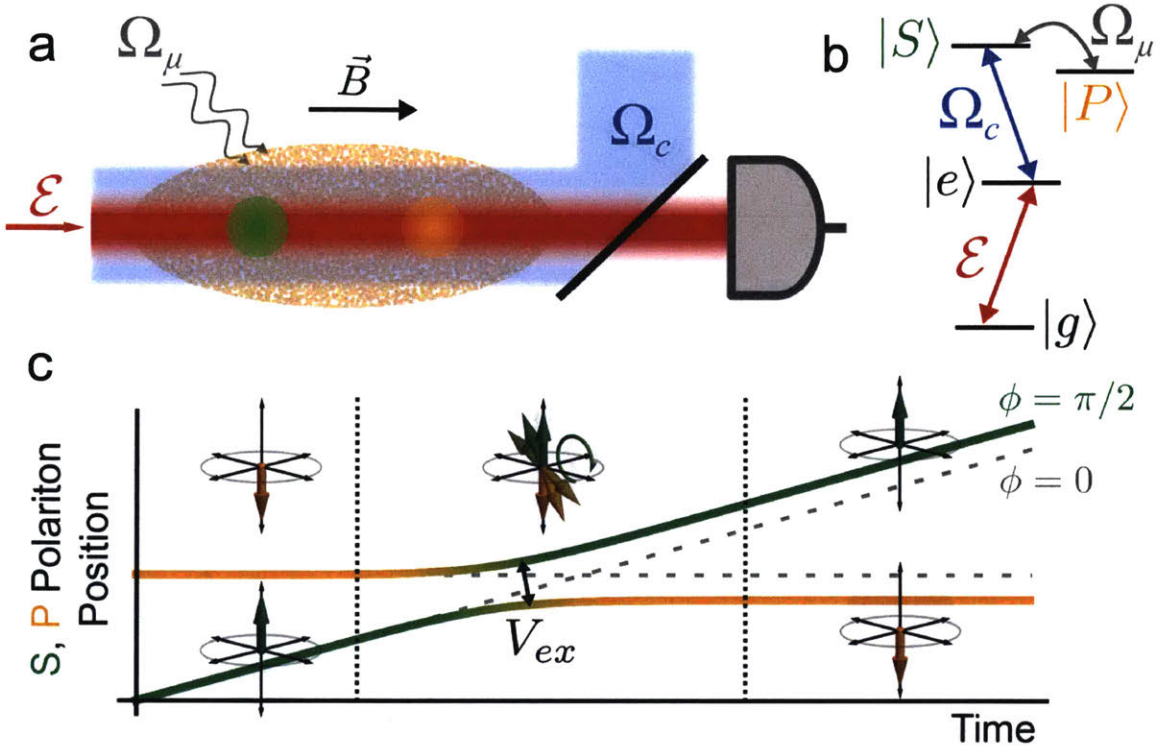

Figure 8-2: **Photon collisions mediated by long-range exchange interactions.** **(a)** Experimental setup. **(b)** Energy diagram. **(c)** A collision is realized between a single, stationary Rydberg excitation in $|P\rangle$ (orange line), and a single, propagating polariton coupled to $|S\rangle$ (green line). As they approach in the cloud, the dipole-dipole interaction V_{ex} causes them to switch places and acquire a phase shift of $\pi/2$. Without interactions, the polaritons pass through each other with no phase acquired (grey dashed lines). The Bloch spheres denote the state of each polariton during the interaction (upwards arrows denote $|S\rangle$; downwards arrows denote $|P\rangle$).

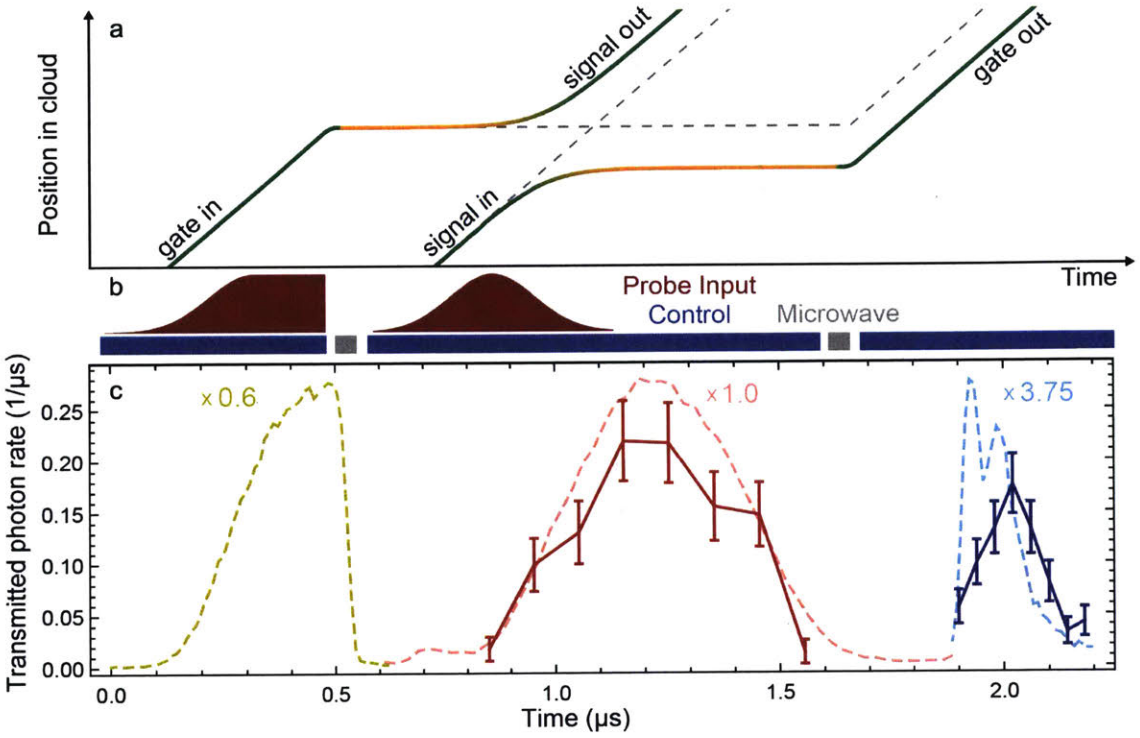

Figure 8-3: **Experimental sequence and pulse shapes.** **(a)**, **(b)** Illustration of experimental procedure. **(c)** Average transmitted intensity through the atomic cloud (dashed lines), showing the leaked gate pulse (yellow, scaled by a factor of 0.6 for display), the signal pulse (red), and the retrieved gate pulse (blue, scaled by a factor of 3.75). The average transmitted intensity is representative of the intensity in the absence of interactions, owing to the low incident photon number. The dark blue points show the retrieved gate intensity conditioned on the detection of a signal photon in the same experimental cycle, while the dark red points show the transmitted signal intensity conditioned on the detection of a retrieved gate photon. All of the features in the data are quantitatively described by a numerical simulation with independently measured parameters.

phase of the transmitted signal is $\phi_c = 0.48(3)\pi$ (Fig. 8-4(a)). Without conditioning, the signal phase $\phi = 0.03\pi$. This difference confirms that the phase arises from interaction with a single gate excitation. $\phi = 0$ is defined by a control experiment with $n_g^{in} = 0$. This phase is slightly different from the phase measured without any atoms present, and results from the effects of atomic dispersion on the far-detuned LO, as well as small phase shifts on the probe arising from a minority of atoms not prepared in $|F = 2, m_F = 2\rangle$.

At the same time, the conditional signal transmission is only reduced by a factor of 0.77(6) compared to its value without interactions, or rather, $\frac{\langle n_s n_g \rangle}{\langle n_g \rangle} \frac{1}{\langle \tilde{n}_s \rangle} = 0.77(6)$. Similarly, the conditional gate retrieval $\frac{\langle n_s n_g \rangle}{\langle n_s \rangle} \frac{1}{\langle \tilde{n}_g \rangle} = 0.82(7)$. Here, $\tilde{n}_s$ ($\tilde{n}_g$) denotes the number of detected signal (gate) photons in a control measurement (similar to the control experiment in Fig. 8-7, but with only one spatial mode) with $n_g^{in} = 0$ ($n_s^{in} = 0$), while n_s and n_g are the number of detected photons for average input photon numbers, $\langle n_s^{in} \rangle = 0.25$ and $\langle n_g^{in} \rangle = 0.15$. The high transmission, together with the uniformity of the $\pi/2$ phase shift across the pulse, establishes that polariton collisions under dipolar interactions are highly coherent.

We measure the transmission probability for an incident signal (gate) photon to be 0.56 (0.06) in control experiments where the gate (signal) photon is absent. The low gate retrieval is attributed to limited coherence time as well as insufficient optical depth. If we reduce the storage time to 100ns, then the storage and retrieval efficiency is increased to 0.4. We take into account that the input gate pulse is not fully compressed into the medium by subtracting the detected leaked pulse (before $0.6\mu s$ in Fig. 8-3(c)) scaled by the linear transmission. The coherence time is limited by Doppler broadening and collisions between the ground state atoms and the Rydberg excitations. For our temperature of $20\mu K$, the Doppler rms width is $2\pi \times 35kHz$, corresponding to a lifetime of $1.9\mu s$, comparable to our storage time $1.5\mu s$. The collisional dephasing is evidenced by our density dependent coherence time. It can be improved by switching to a different Rydberg state and a more homogeneous optical trap geometry [104, 105].

To demonstrate the robustness of the phase shift, we repeat the measurements in

Fig. 8-4 for a range of atomic densities, as summarized in Fig. 8-5. For each density, we measure the conditioned phase shift ϕ_c of the transmitted signal field, as well as the joint probability $T_c = \frac{\langle n_s n_g \rangle}{\langle \bar{n}_s \rangle \langle \bar{n}_g \rangle}$ of both signal and gate photons being transmitted, relative to their independent transmission probabilities. The phase shift saturates at $\phi_c = \pi/2$ at high densities, indicating that it is a robust property of the photon collision. The transmission probability has a minimum at intermediate densities and it improves in the high-density limit, in stark contrast to conventional resonant dipole blockade, where transmission is exponentially suppressed at high densities.

The emergence of the phase shift can be understood from a simple model incorporating propagation and interactions. Let $\psi(r, r')$ denote the two-body spatial wavefunction for polaritons at positions r and r' coupled to states $|S\rangle$ and $|P\rangle$, respectively. The evolution of the system (in the limit of large atomic density) is governed by the effective Schrödinger equation:

$$i\frac{\partial}{\partial t}\psi(r, r') = -iv_g\frac{\partial}{\partial r}\psi(r, r') + \frac{1}{\hbar}V_{ex}(r - r')\psi(r', r) \tag{8.1}$$

where v_g denotes the S-polariton group velocity, and $V_{ex}(r-r') = \frac{C_3}{|r-r'|^3}$ is the dipolar interaction between the states $|S\rangle$ and $|P\rangle$, whose action on the polaritons at r and r' is to swap their positions, coupling the state $\psi(r, r')$ to $\psi(r', r)$. Eq. 8.1 has a simple time-independent solution in the continuous-wave limit:

$$\psi(r, r') = \exp[-\frac{r_s^2}{2(r - r')^2}]\exp[-i\,\mathrm{sign}[(r - r')C_3]\frac{\pi}{4}] \tag{8.2}$$

Here, $r_s = \sqrt{\frac{C_3}{v_g}}$ is the *hopping radius*, which is the distance at which the approaching polaritons exchange their positions and start propagating away from each other. Correspondingly, there is very little probability of finding the polaritons at distances $|r - r'| < r_s$. The complex transmission coefficient:

$$t_c = \frac{\lim\limits_{(r-r')\to\infty}\psi(r, r')}{\lim\limits_{(r-r')\to-\infty}\psi(r, r')} \tag{8.3}$$

takes the value $e^{\pm i\pi/2}$, for $C_3 \lessgtr 0$.

Remarkably, this robust phase shift can be understood by considering the symmetries of the effective Hamiltonian H_{eff} governing Eq. 8.1. In the centre-of-mass frame, $\mathbb{P}H_{eff} = -H_{eff}\mathbb{P}$, under the transformation $\mathbb{P} : \psi(r, r') \longmapsto \text{sign}[r' - r]\psi^*(r, r')$. $\mathbb{P}$ is analogous to the particle-hole symmetry encountered in fermionic condensed matter systems, and constrains the structure of the eigenstates of H_{eff} such that t_c must be purely imaginary for low-energy scattering processes, ensuring a phase shift of $\pm\pi/2$ regardless of the precise parameters in Eq. 8.1.

The model in Eq. 8.1 does not include absorption from interaction-induced level shifts, which may occur when $V_{ex}(r - r')$ exceeds the linewidth of the EIT linewidth Ω_c^2/Γ. Absorption will occur when polaritons are within the blockade radius, $r_b = (2\Gamma C_3/\Omega_c^2)^{1/3}$. The blockade radius is related to the hopping radius by $r_s = \sqrt{OD_b/2}r_b$. Importantly, if $OD_b > 2$, then $r_s > r_b$, which allows the exchange interaction to take place before the polaritons are sufficiently close to experience absorption. Experimentally, the minimum transmission measured in Fig. 8-5(b) occurs at $OD_b \approx 2$, beyond which the transmission indeed steadily increases. This analysis validates the use of Eq. 8.1 in the high-density limit $OD_b \gg 1$. A more detailed calculation shows that the photon loss decreases asymptotically as $OD_b^{-3/2}$ while the phase difference from $\pi/2$ decreases as e^{-OD_b}. This scaling is more favourable than that corresponding to off-resonant Rydberg blockade. With off-resonant Rydberg blockade, interaction with a stored photon (or between two counter-propagating photons) results in a phase $\varphi \sim OD_B\frac{\Gamma}{\Delta}$, with a transmission $\sim e^{-OD_B(\frac{\Gamma}{\Delta})^2}$ [84]. For a given phase, the transmission scales as $e^{-\frac{\varphi^2}{OD_B}} \sim 1 - \frac{1}{OD_B}$, and therefore the loss scales as OD_B^{-1}.

Additionally, we perform similar experiments with the state $|P\rangle$ replaced by $|97S_{1/2}\rangle$ or $|99S_{1/2}\rangle$. In contrast to $|99P_{3/2}, m_F = 3/2\rangle$, $|97S_{1/2}\rangle$ interacts with $|S\rangle$ with (almost) pure blockade, while $|99S_{1/2}\rangle$ leads to competing blockade and exchange. The strengths of the interactions and the characteristic length scales are summarized in Table 8.1.

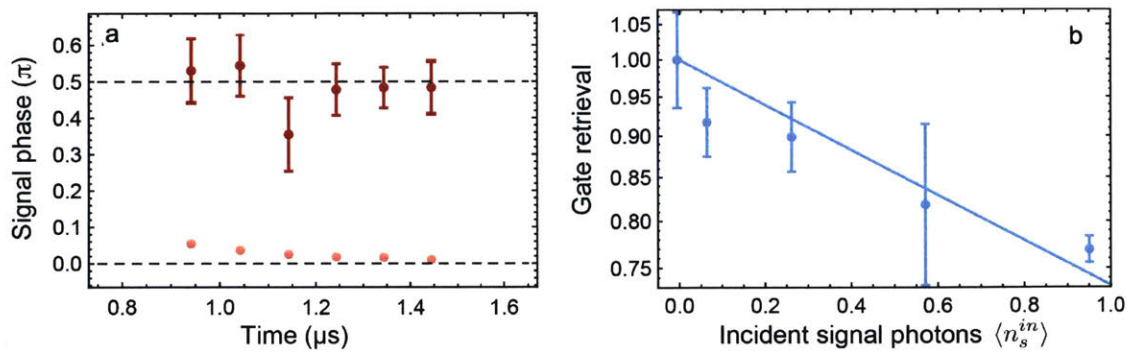

Figure 8-4: **Observation of coherent collisions between the photons under dipolar interactions.** **(a)** Phase of the transmitted signal field with (dark points) and without (light points) conditioning on the detection of a retrieved gate photon. **(b)** Normalized retrieval efficiency of the stored gate excitation as a function of average signal photon number $\langle n_s^{in} \rangle$. The data are fitted to an exponential decay of the form $exp[-\frac{\langle n_s^{in} \rangle}{n_d}]$, where $n_d^{-1} = 0.26(5)$ is the gate polariton destruction probability per incident signal photon. These measurements are taken with an optical depth OD=46.

Pair states	C_3/h $(GHz \cdot \mu m^3)$	χ_6/h $(THz \cdot \mu m^6)$	C_6/h $(THz \cdot \mu m^6)$	r_s (μm)	r_b (μm)
$\|100S_{1/2}, 1/2\rangle + \|99P_{3/2}, 3/2\rangle$	33.4			19	12
$\|100S_{1/2}, 1/2\rangle + \|99S_{1/2}, 1/2\rangle$		48.7	65.3	12	13
$\|100S_{1/2}, 1/2\rangle + \|97S_{1/2}, 1/2\rangle$		-0.6	-114	5	13

Table 8.1: **Characterizations of the interactions of the pair states used in this experiment.** The hopping radius r_s and blockade radius r_b are calculated with $\Omega_c = 16$MHz, the length of the medium $L = \sqrt{2\pi}\sigma_a = \sqrt{2\pi} \times 35\mu m$ and $OD = 40$. $C_6 > 0$ (< 0) indicates a repulsive (attractive) interaction between the Rydberg states. When the blockade and exchange interactions follow the same power law $r^{-\alpha}$, the hopping radius can generalized as $\frac{1}{v_g}\int_\infty^{r_s} |V_{ex}(z)|\, dz = 1/2 \Rightarrow r_s = (\frac{2\chi_\alpha}{(\alpha-1)v_g})^{\frac{1}{\alpha-1}}$. The blockade radius can be generalized as $r_b \equiv (2\Gamma(|\chi_\alpha| + |C_\alpha|)/\Omega_c^2)^{1/\alpha}$.

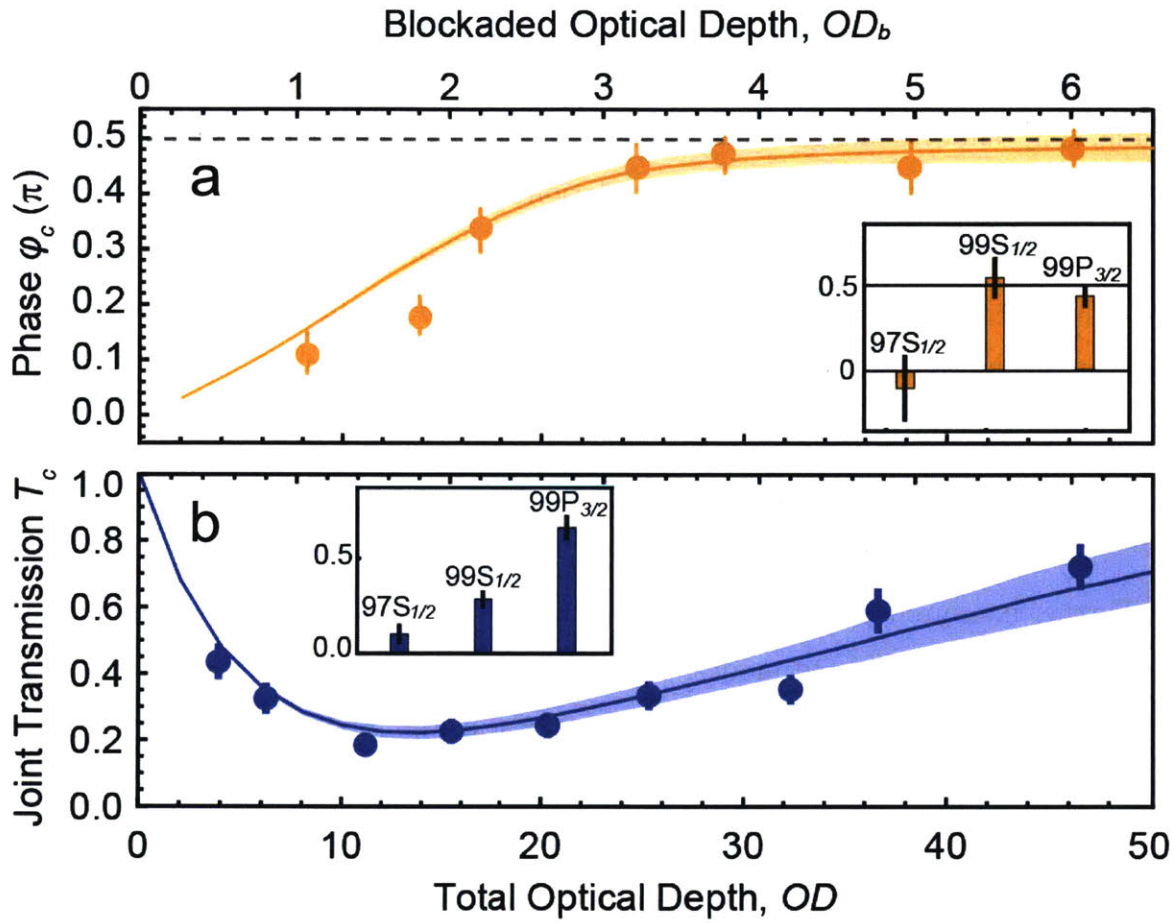

Figure 8-5: **Density dependence and robustness of the scattering phase.** **(a)** Conditioned phase shift ϕ_c over a range of atomic densities, quantified by the total optical depth OD. Also shown on the top axis is the estimated optical depth over one blockade radius, for a Rydberg excitation at the centre of the cloud. **(b)** Joint probability of the signal and gate photons being transmitted, relative to their independent transmission without interactions: $T_c = \frac{\langle n_s n_g \rangle}{\langle \tilde{n}_s \rangle \langle \tilde{n}_g \rangle}$. The lines show the result of a numerical simulation of the storage, interaction and retrieval stages of the experiment, including experimental non-idealities such as dephasing from Rydberg-ground-state collisions. The confidence bands reflect the contribution of random atomic positions to the numerical simulations. The density-dependent shifts [51] of the Rydberg states lead to random local two-photon detunings. The insets show the results of similar experiments at high optical depths (OD= 55), with the state $|P\rangle$ replaced by $|97S_{1/2}\rangle$ or $|99S_{1/2}\rangle$. These two states have weaker or absent dipole-dipole interactions with $|S\rangle$, respectively.

8.4 Collisions between photons in two spatial modes

We demonstrate that the long-range nature of the interaction allows photons to hop between separated transverse optical modes. We repeat the experimental sequence in Fig. 8-3, but with the gate and signal fields incident in distinct transverse spatial modes (Fig. 8-6(a)). Intensity cross-correlation measurements between the transmitted light in the two modes (Fig. 8-6(b)) reveal anti-correlations between signal and gate photons exiting in their incident modes ($g^{(2)}_{inc} = 0.18$) and positive correlations between signal and gate photons exiting in swapped modes ($g^{(2)}_{sw} = 5.8$). Together, these show that the interaction causes pairs of photons to hop between modes in the atomic cloud, such that the signal exits in the mode in which the gate was incident, and vice versa.

Further measurement is performed to estimate the probability of photons hopping between spatially separated modes. This involves alternating between the pulse sequence shown in (Fig. 8-6 and pink shaded area in Fig. 8-7) and another sequence where the signal pulse is sent after the gate pulse is retrieved (grey shaded area in Fig. 8-7). In the latter sequence, the signal and gate fields experience the same loss, but do not interact with each other as they are never present in the cloud at the same time. The difference between these measurements allows the influence of interactions to be isolated. Figure 8-8(a) shows the measured pulse shapes at each detector. The gate (signal) pulse is incident in mode A (B). The majority of the light in the "wrong" detector (e.g., signal light in detector A) results from a slight mixing of the modes at the detectors (approximately 10%), since the modes are not perfectly orthogonal. To see the role of interactions above this background, we look at photon pair events as shown in Fig. 8-8(b). Without interactions, approximately 1.7% of all transmitted pairs are in swapped modes. With interactions, 58% of pairs exit in swapped modes, although the overall transmission is much lower. In analogy to T_c defined in Fig. 8-5, we isolate the role of interactions over single-particle loss by computing the ratio of the number of pairs exiting in swapped modes (with interactions) to the total number of transmitted pairs in the absence of interactions. This yields 9%, which we take as

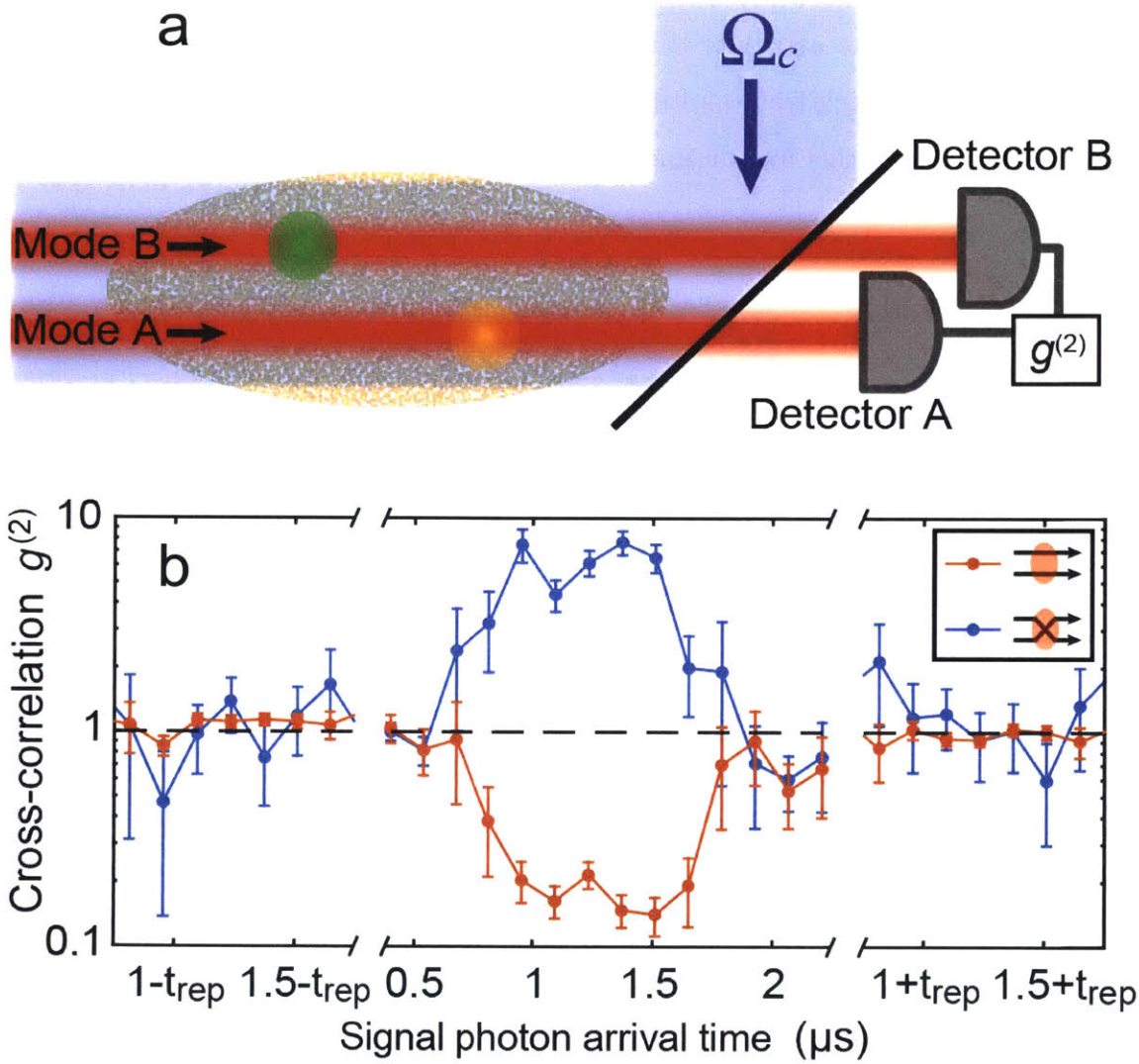

Figure 8-6: **Polariton exchange between separated transverse modes.** **(a)** The gate and signal pulses are now incident in distinct transverse spatial modes A and B, respectively, separated by $1.2w = 5.4\mu m$. The control beam addresses both modes. **(b)** The intensity cross-correlation between signal and gate photons exiting in their incident modes (red points, $g^{(2)}_{inc}$) and in swapped modes (blue points, $g^{(2)}_{sw}$) shows that polaritons switch modes in the cloud. $g^{(2)}_{inc}(t) = \frac{\langle n_s^B(t) n_g^A \rangle}{\langle n_s^B(t) \rangle \langle n_g^A \rangle}$, where $n_s^B(t)$ denotes the number of signal photons detected at time t in mode B, and n_g^A is the total number of gate photons detected in mode A. The definition for $g^{(2)}_{sw}(t)$ is the same, with the modes A and B reversed. The correlations are absent for photons separated by the repetition time of the pulse sequence t_{rep}. These measurements are taken with an optical depth OD=41.

an estimate of the probability for a photon pair to switch modes as a result of the interaction. This value is significantly lower than T_c reported in Fig. 8-5 for photons in the same mode. We attribute this to increased separation between the photons, as well as losses resulting from multiple signal and gate photons being present during the same pulse, since this measurement was performed with $\langle n_g^{in} \rangle \approx \langle n_s^{in} \rangle \approx 1$.

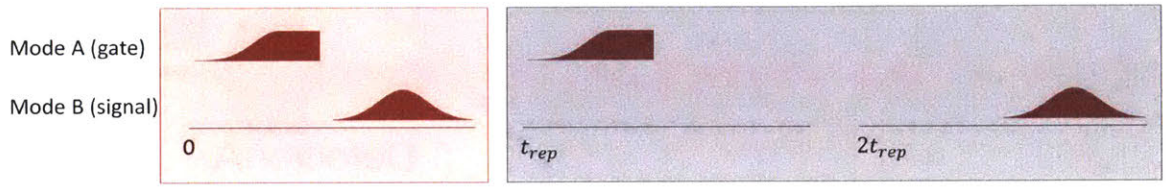

Figure 8-7: **The experimental sequence of the photon hopping probability measurement.** Here, only the probe pulses are shown. The control beam and the microwave sequences are the same as in Fig. 8-3(b), and are omitted. The control experiment representing the scenario without the interaction is shaded in grey.

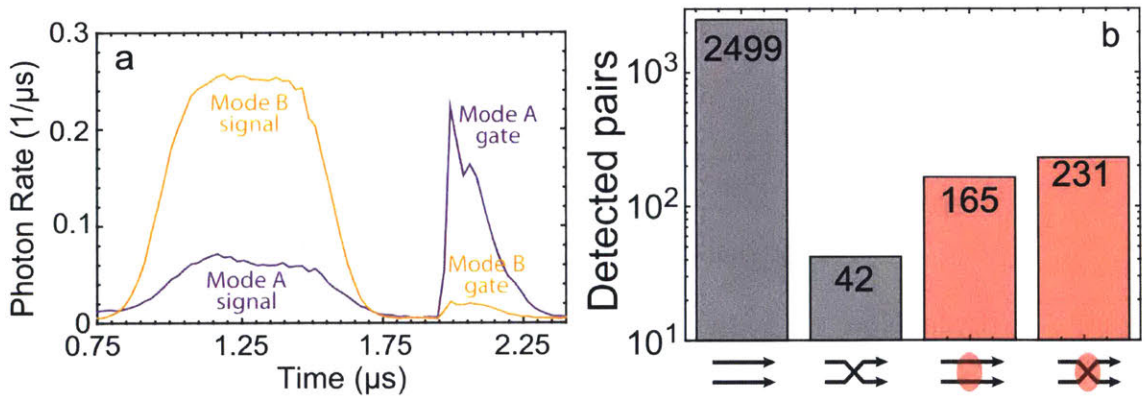

Figure 8-8: **Pulse shapes and detected pairs. (a)** Pulse shapes measured by the detectors with the interaction (pink shaded area in Fig. 8-7 and Fig. 8-6). The full data record is averaged to produce these curves. **(b)** Photon pair detection events. The parallel (crossed) arrows denote the number of signal and gate pairs detected in their incident (swapped) modes. The left two bars show the result of the alternate pulse sequence without interactions, while the right two bars show the result of the pulse sequence in (a), where interactions are expected to be present. From left to right, the y-axis values are 2499, 42, 165, and 231.

8.5 Summary and outlook

To conclude, we conduct series of experiments where a propagating photon collides with a stored photon. The exchange interaction that has rarely been explored previously manifests itself as high transmission of the propagating photon in the dissipative regime, high retrieval efficiency compared with similar experiments based on blockade interaction [22], and above all a robust conditional $\pi/2$ phase shift. We demonstrate the competing effects of the exchange and blockade interaction by repeating the experiments with different Rydberg states. In case of dominant blockade, the propagating photon exhibits no measurable phase shift, and the joint transmission is greatly reduced. Further, the long range nature of the interaction is verified by a similar experiment with the propagating photon and the stored photon in two different spatial modes.

Our results open up new possibilities for realizing robust quantum gates and many-body phenomena with strongly interacting photons. A modest extension of this work should allow for a controlled π phase shift quantum gate between two photons, by using microwave control to pass the polaritons through each other a second time before they exit the cloud. The demonstrated interaction between polaritons is also a powerful tool for studying the quantum many-body dynamics of photons. In particular, the symmetries that result in the robust phase shifts observed in this work are identical to those that result in Majorana fermions in one-dimensional wires, which are expected to feature similarly robust phase shifts under braiding operations. Although the present two-particle scattering process has important distinctions, in that the low-energy mode is not protected by an energy gap, the latter could potentially be engineered (for example, via polariton interactions). Likewise, extensions along the lines of recent proposals [106, 107] could be explored to realize topological photonic systems.

Chapter 9

Summary and Outlook

We demonstrate strong nonlinear interactions between propagating photons both in the dissipative and dispersive regimes. In the latter regime, we observe two- and three-photon bound states by measuring the correlation functions and conditional phase of the outgoing photons. Besides, the van der Waals level shifting interaction that have been widely explored in recent years, we also study the exchange interactions between a propagating and a stored photon. A robust $\pi/2$ phase shift is observed under the exchange interaction dictated by a symmetry of the Hamiltonian.

Strongly interacting photons generally find application in quantum information [108]. Optical photons are promising flying qubits and important parts of hybrid systems [109, 110] in the effort of scaling up. And quantum nonlinearity is an indispensable part of deterministic photonic quantum logic. In particular, our work on the symmetry-protected collisions with exchange interactions sheds light on realizing topologically encoded qubits–a crucial recent development in quantum computation. In topological quantum computing, the information is stored in a non-local manner, and is therefore intrinsically robust against interactions with the environment and details of operations. Topological quantum computation takes advantage of a quasi-particle called non-Abelian anyon, which arises in a system with degenerate ground states that are separated from the excited part of the energy spectrum. Exchanging two identical non-Abelian anyons results in a unitary rotation of the wavefunction into a different ground state, instead of simply picking up a phase as for fermions,

bosons and Abelian anyons. A set of the spacetime trajectories of the anyons that can smoothly deform to each other without cutting is called a "braid". The universal gates are implemented by braiding (see Fig. 9-1 for examples of braiding). Strong indications of the existence of a simplest non-Abelian anyon called the Majorana zero mode or Majorana bound state [111, 112] have been observed but braiding has yet to be achieved.

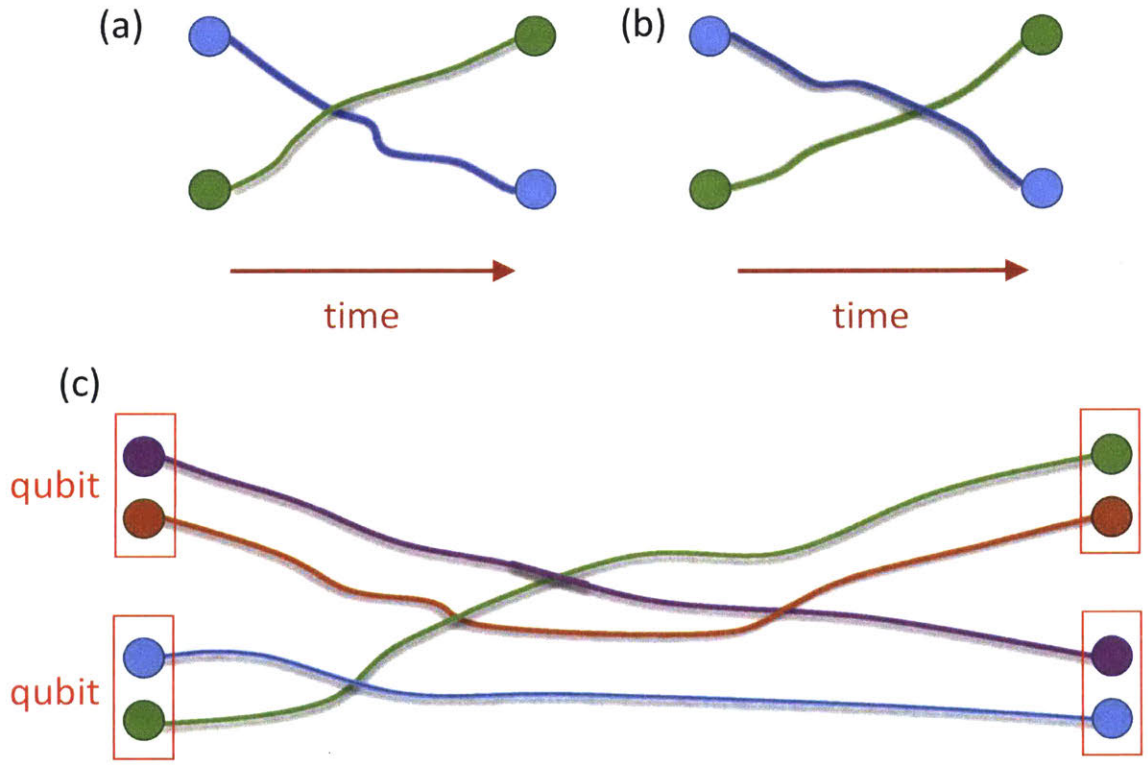

Figure 9-1: **Examples of braiding.** Anyons exist in lower dimensions where rotating clockwise and counter-clockwise are not topologically equivalent. In other words, a trajectory, also called worldline, being above or below another forms different braids, as in (a) and (b). (c) shows an example of manipulation of the MZM pair qubits. In the end, the states of the qubits are measured, and the outcome only depends on the topology (braid), not the exact trajectory. Therefore, topological quantum computation is immune to small perturbations.

In addition, the experimental success in realizing quantum nonlinearity has sparked a lot of interest into many-body problems of photonic matter–strongly interacting massive photons [113]. This represents a remarkable new venue for quantum nonlinear optics. It can be used to simulate, for example, strongly interacting condensed

matter systems. However, it has a number of unique aspects when compared with condensed matter systems or other quantum simulators such as ultracold atoms in optical lattices: They are intrinsically driven and open. Light must be injected and can leak out. They are generally not coupled to a thermal bath. The correlations, phase transitions and the non-equilibrium quantum dynamics of strongly interacting photons have yet to be studied.

Appendix A

Useful circuits

A.1 Avalanche photodectors

We use Si avalanche photodiodes from Hamamatsu (S3884).

A.1.1 DC coupled avalanche photodector

The circuit of the DC coupled avlanche photodector features two stages: (1) the current signal is tranformed into the voltage signal; (2) the voltage signal is amplified. R1, R2 and R3 can be changed to optimize the gain and bandwidth as needed. For the set of values shown in Fig. A-1, the measured bandwidth is 20MHz (Fig. A-2).

A.1.2 AC coupled avalanche photodector

To increase the bandwidth of the APDs we use commercial RF-amplifiers instead of our self-built amplification boards. The APDs still need to biased with a high DC voltage (~130V), which can be done in various ways (Fig. A-3):

1. The simplest solution is to couple a positive bias voltage via a bias-Tee on the cathode side of the APD. This can be done with commercial bias-tees or a simple HV-compatible components. In this case, the same positive HV sources that we use for the amplified APDs can be used.

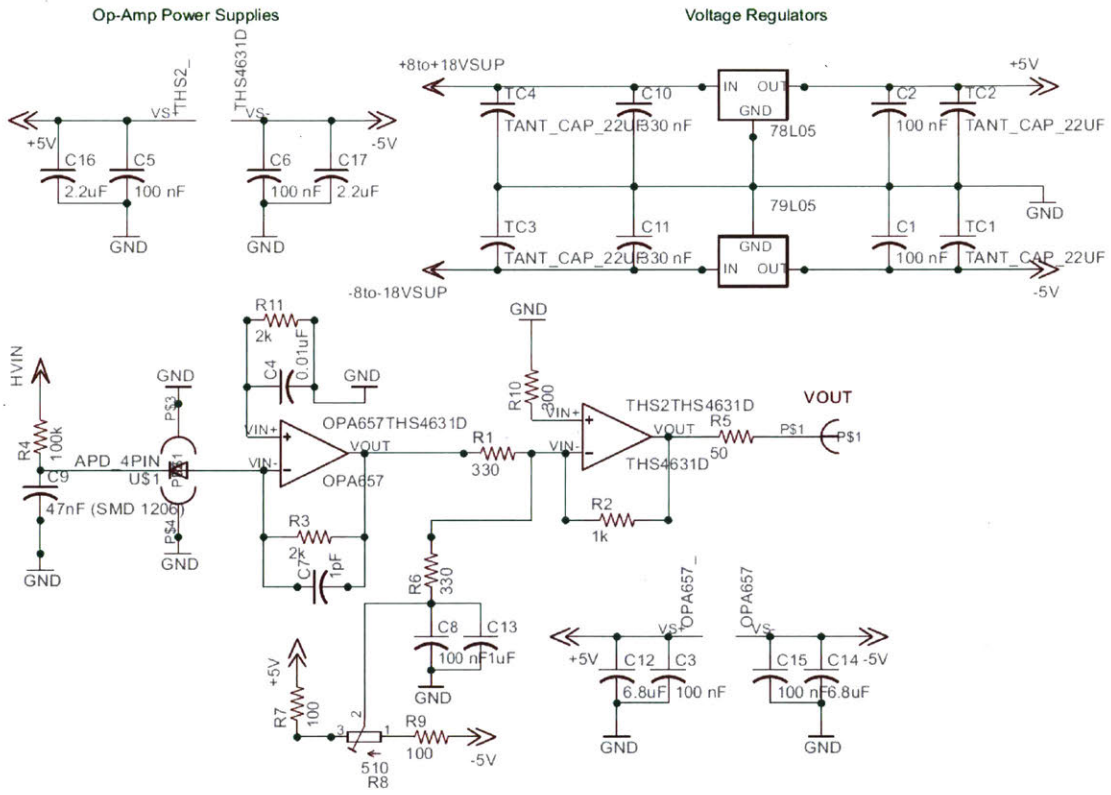

Figure A-1: **DC coupled Avalanche photodector.**

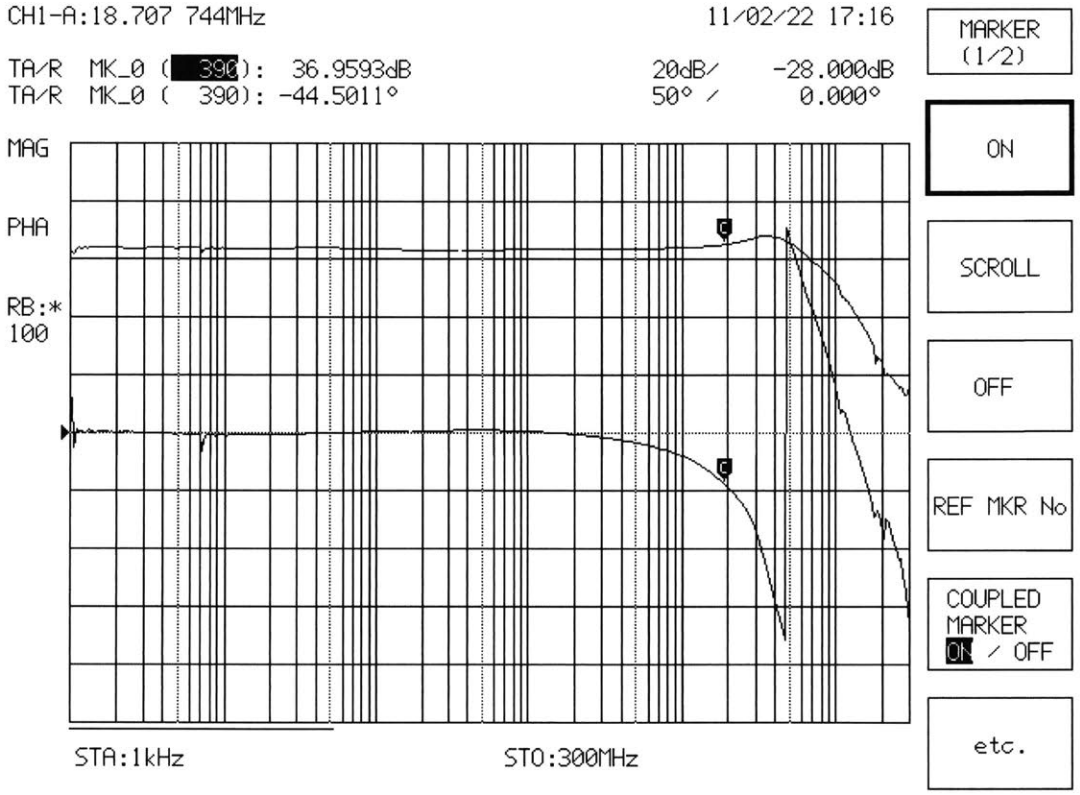

Figure A-2: **The tranfer function of the DC coupled Avalanche photodector.** The top line is the gain, the bottom phase.

2. Due to the way the APDs are made, the cathode side has a higher residual capacitance. To gain extra bandwidth, the AC output to the amplifier should be on the anode side. This can be done by simply turning the diode around and biasing with negative voltage on the anode side with the same bias-tee.

3. Instead of a bias tee, one can apply the DC bias on the cathode side and get the AC output from the anode side. Again, HV-capable resistor and capacitor must be used. On the output side, the capacitor should be chosen with the impedance of the amplifier in mind.

We currently use the scheme as shown in Fig. A-3(1) with a bias tee from Picosecond Pulse Labs (Model 5530B-104) and low noise amplifiers from Mini-Circuits (ZFL-500LN). The measured bandwidth is above 100MHz (Fig. A-4).

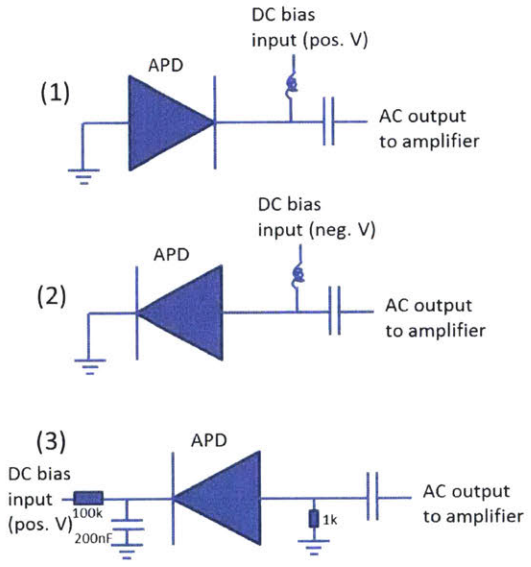

Figure A-3: **Various ways to bias APD.**

A.2 Bipolar bias coil controllers

The sketch of the bias coils is shown in Fig. A-5. Initially, all the coils have $\sim$ 100 turns and are 5ohm each (including wires). The resulting magnetic field is 2.1, 1.7 and 4.3 Gauss/A for x, y and z directions, respectively. Ideally, we would like to put

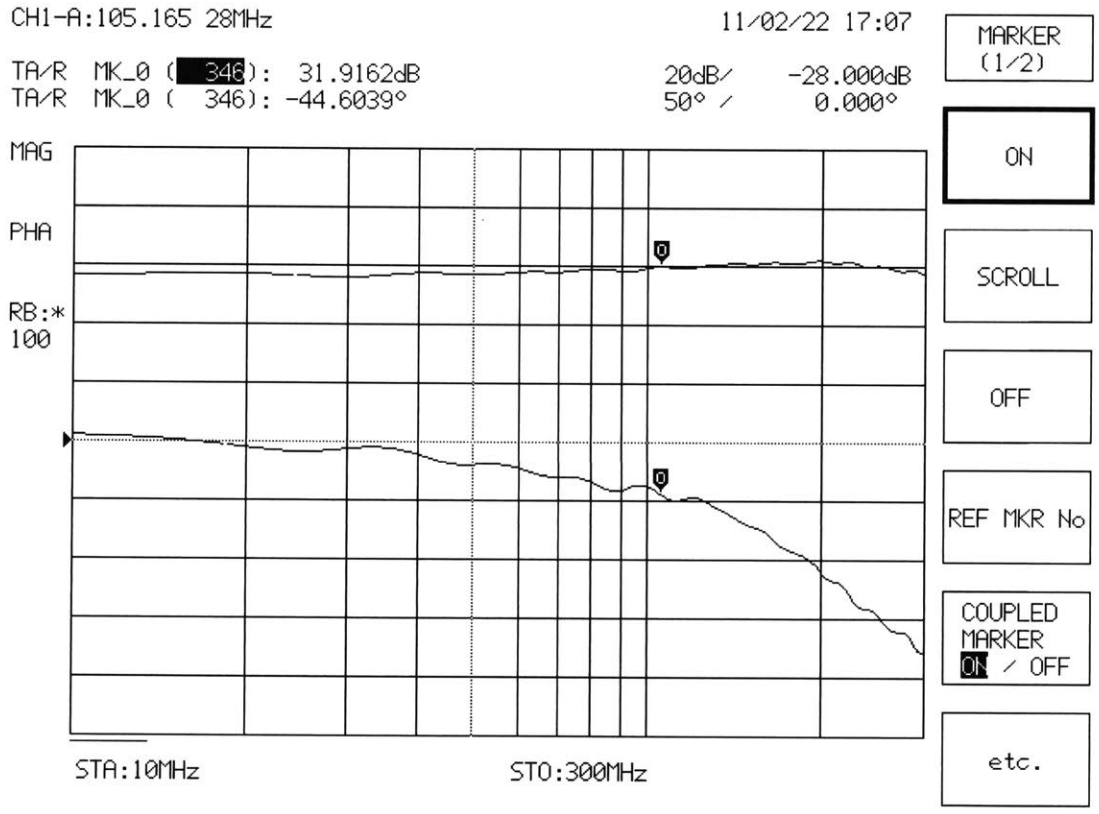

Figure A-4: **The transfer function of the AC coupled avalanche photodector including an amplifier from Mini-Circuits (ZFL-500LN).** The top line is the gain, the bottom phase.

the coil pair in series so that the same current runs through the pair. On the other hand, as the output voltage (Fig. A-6) is capped below 12V (maximum gate voltage 15V minus the gate-source threshold voltage of the MOSFETs 3V), the maximum current on a $\sim$ 10ohm load is $\sim$ 1A. This is not quite enough for us. Therefore, all the six coils are controlled independently. Before the experiment in Chap. 7, we re-wired the x bias coils with thicker wires, resulting in a $\sim$1ohm resistance. Additionally, a small coil with 50 turns is added. These changes allow us to apply a much larger magnetic field along the quantization axis.

On top of the current feedback, the circuit includes a positive voltage feedback. It takes care of the increasing resistance of the coil as the temperature increases. Last, big capacitors (X1-1,2,3 in Fig. A-6) are added to the power supply of the MOSFET. Without those capacitors, the MOSFETs could be damaged when the circuit is powered on/off.

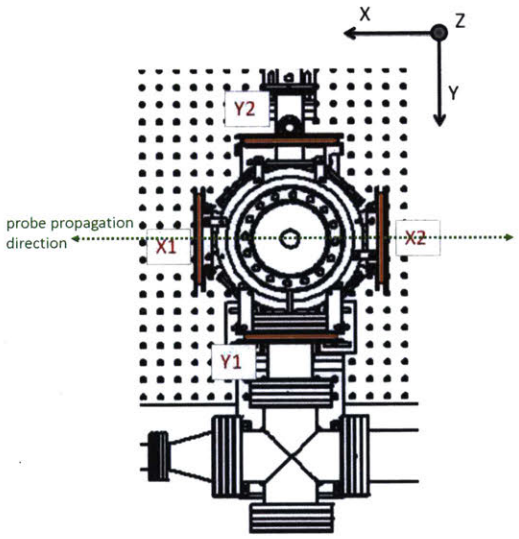

Figure A-5: **The sketch of the bias coils around the vacuum chamber.** There are two z coils, above and below the chamber, not drawn here. The coils are highlighted in orange.

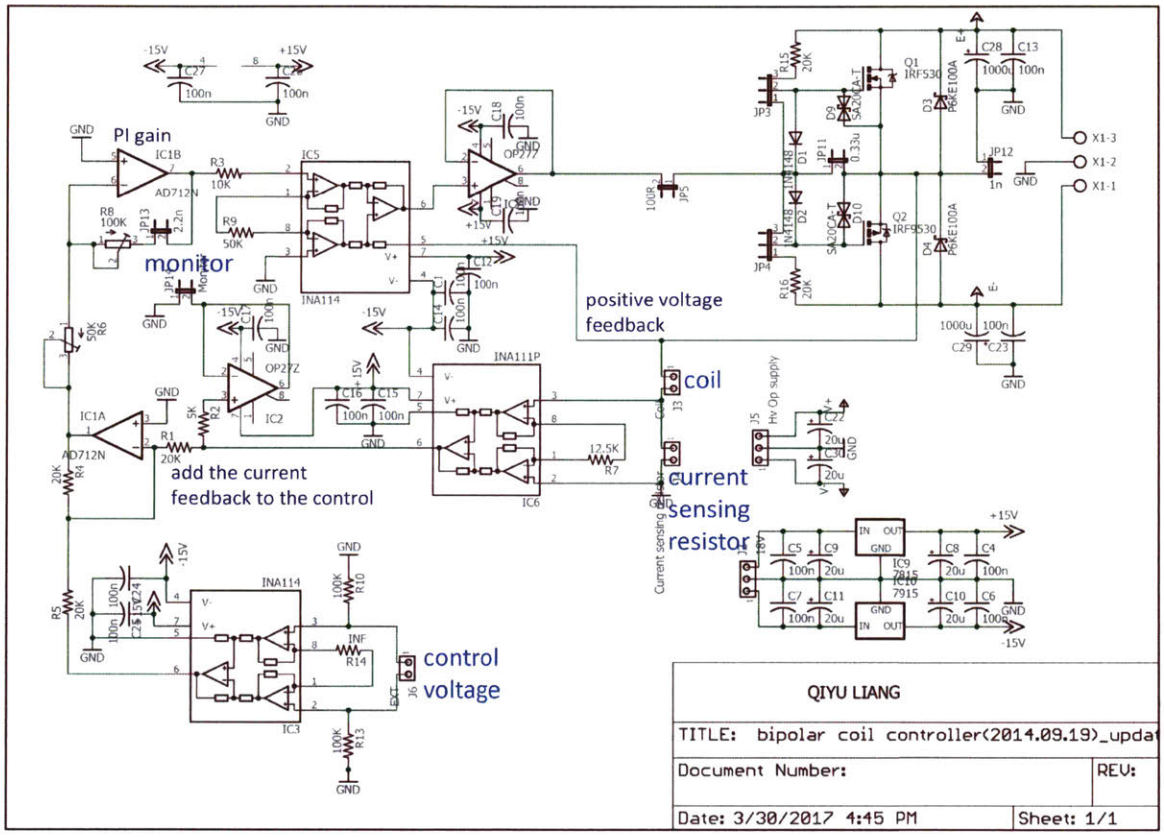

Figure A-6: **The schematic of the bipolar bias coil controllers.**

A.3 AOM drivers

AOMs are crucial in our experiments as they switch and adjust the intensity of all the optical beams. The schematic of the home-built drivers are shown in Fig A-7.

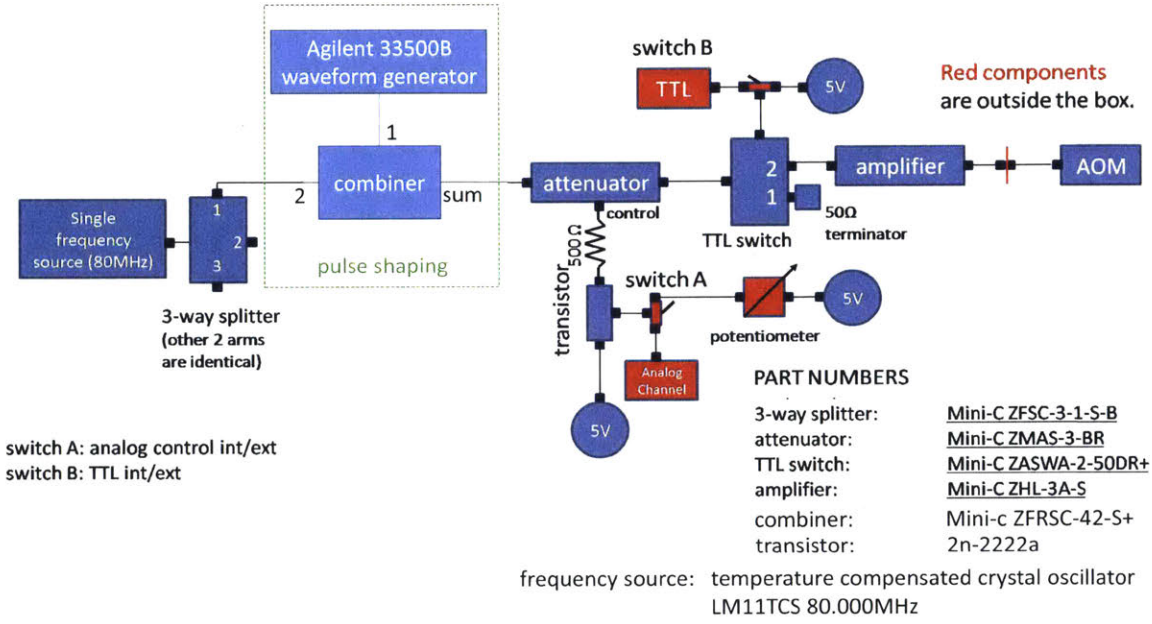

Figure A-7: **The schematic of the AOM drivers**. A transistor is added in the analog input arm to avoid the attenuator drawing too much current from the control voltage source (analog channel). The frequency source is replaced with a direct digital synthesizer (DDS) AD9958 whenever a different frequency other than 80MHz is needed. The maximum power output is 1W. When more power is required (such as driving the AOM in the dipole trap beams), more powerful amplifiers (ZHL-1-2W-S) are used. The parts in the green box are used for pulse shaping, particularly useful for the probe light.

A.4 Laser lockbox

Figure A-8 shows the schematic of our home-built laser servo controller. This type of lockbox is used to lock virtually all our lasers, as well as the transfer cavity, in the lab.

The schematics shown in Figs. A-9 and A-10 are used to lock the MOT cooling laser and the repumper laser, respectively.

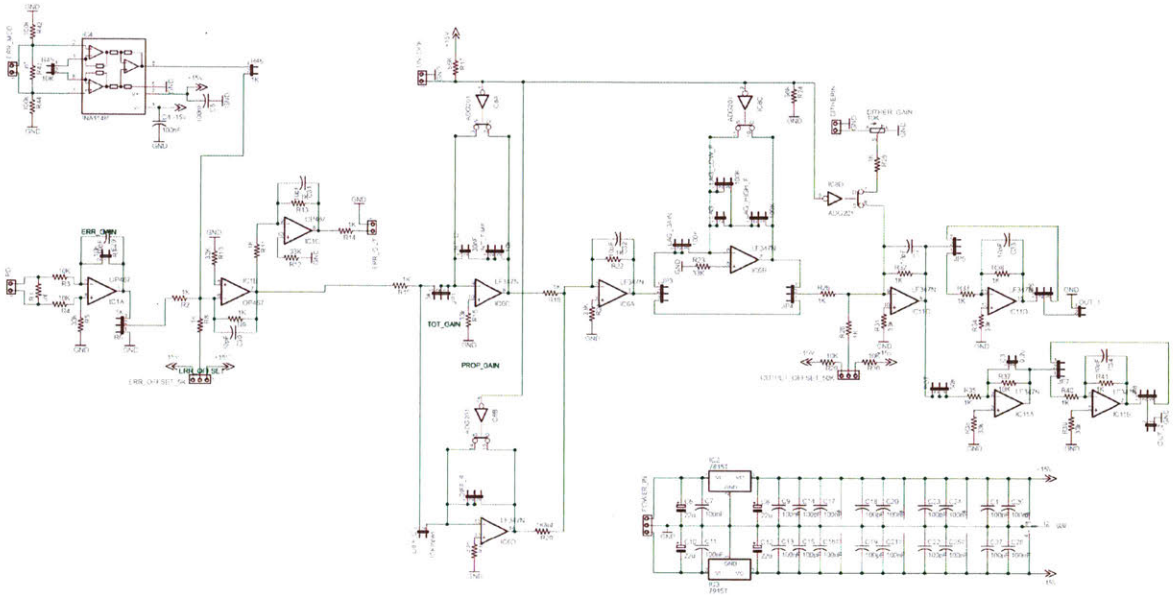

Figure A-8: **The schematic of laser servo controllers.**

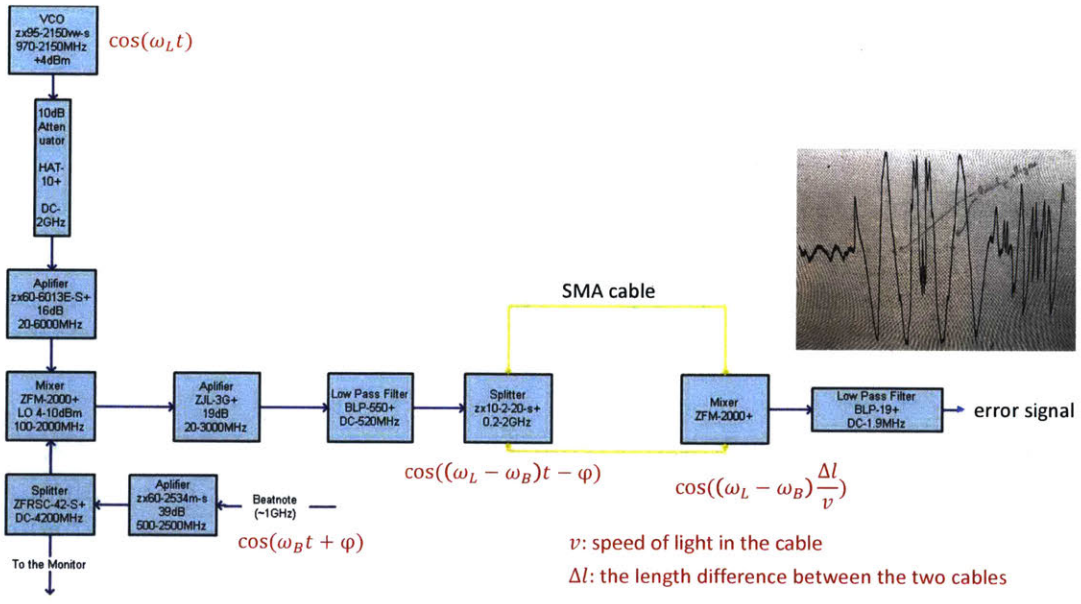

Figure A-9: **Error signal generation from the beat note.** The inset shows an example of the error signal. The two arrows point to possible locking points.

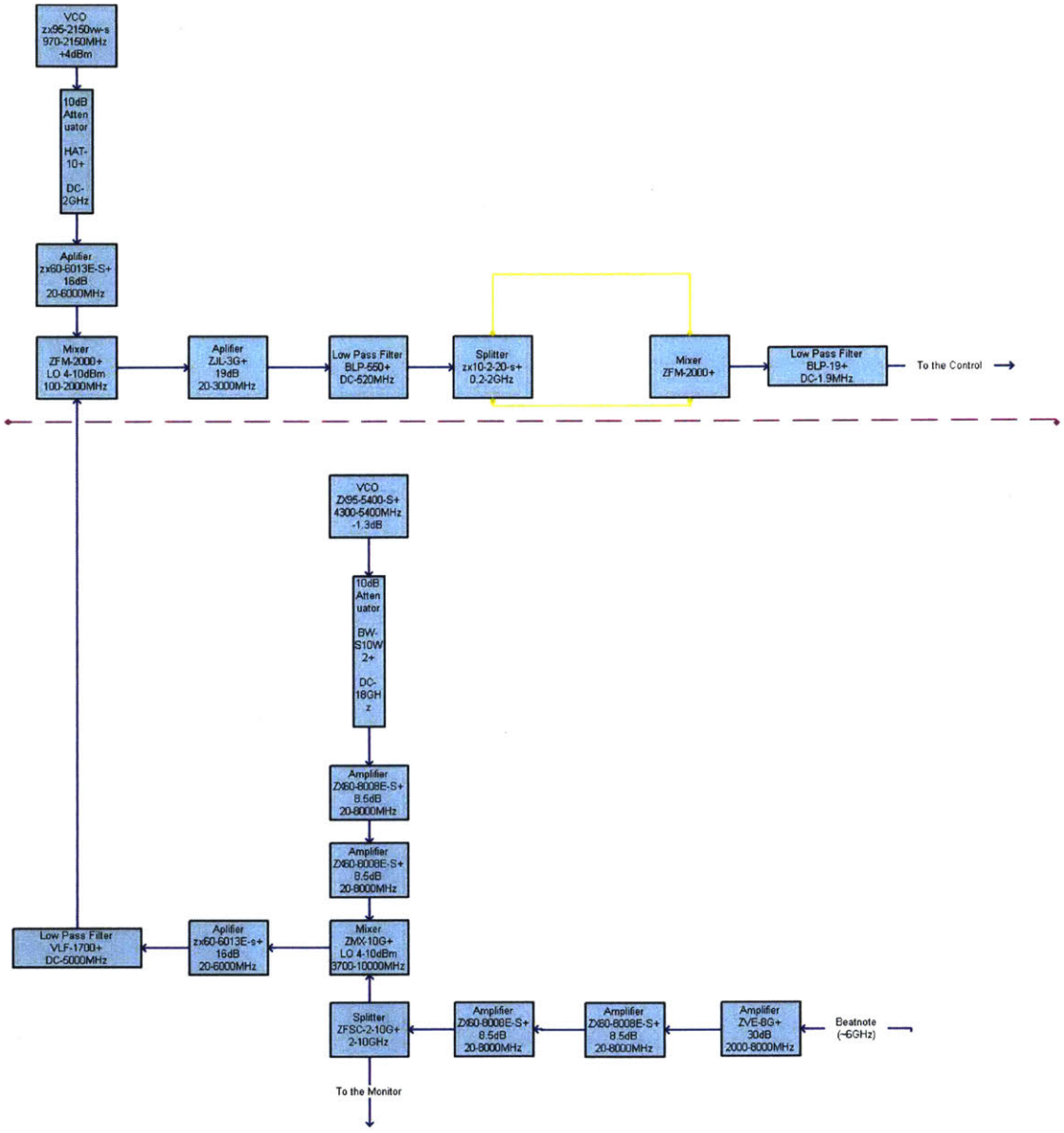

Figure A-10: **Error signal generation from the higher frequency beat note.** As the frequency of the beat note gets higher, it is increasingly hard to find a good VCO with a large tuning range. Hence, in order to lock the laser, we add additional VCO to mix down the frequency. The components above the pink dashed line are the same as in Fig. A-9. Therefore, by switching a couple of cables, the locking regime can be easily changed.

Appendix B

Rydberg pair interactions

The Rydberg pair interactions in this thesis are generated by a MATLAB program first written by Ofer Firstenberg and then further developed by Jeff D. Thompson. Alternatively, one can use the free software provided by the authors of the tutorial Ref. [114]. Here, I highlight the key steps about how the parameters are set and how the calculations are done.

The calculation is done with zero fields and zero angle ($\theta = 0$ in Fig. B-1) between the quantization axis and the internuclear separation vector $\vec{R}$. Assuming the two atomic states in the initial pair state are $|n_1 l_1 j_1 m_1\rangle$ and $|n_2 l_2 j_2 m_2\rangle$, where n is the principal quantum number, l is the orbital angular momentum quantum number, and j and m are the quantum numbers for total electron angular momentum and its component along the quantization axis, respectively. In order for an atomic state $|nljm\rangle$ to be included, it has to satisfy the following conditions:

1. $min(n_1, n_2) - 5 \leq n \leq max(n_1, n_2) + 5$, where min (max) denotes the smallest (largest) number among those in the following parenthesis.

2. $l \leq max(l_1, l_2) + 3$

Finally, the pair states whose energy is outside the $\pm$1GHz window centered around the initial pair state (at the double-atom dissociation limit) are excluded.

We then write the Hamiltonian in the basis formed by all the included pair states.

$$H = H_0 + H_{int} \tag{B.1}$$

where H_0 includes the energies of the pair states (at the double-atom dissociation limit) and shifts in external fields, and $H_{int} = \frac{\vec{P}_1 \cdot \vec{P}_2 - 3(\vec{n}\cdot\vec{P}_1)(\vec{n}\cdot\vec{P}_2)}{R^3}$ ($\vec{n}$ is a unit vector in the direction of $\vec{R}$) is the dipole-dipole coupling between the pair states. H_{int} is decomposed in the Cartesian coordinates as in Ref. [115]. The radial dipole matrix elements for $n_1 l_1 \rightarrow n_2 l_2 = l \pm 1$ transistions are calculated by analytical formulae adapted from refs. [116, 117]:

$$R^{n_2 l_2}_{n_1 l_1} = (-1)^{\Delta n} \frac{\nu_c^5}{(n_1^* n_2^*)^{3/2}} D_r(e_c, s) \tag{B.2}$$

$$\Delta n = (n_2 - n_1) - (l_2 - l_1) + 1 + m \tag{B.3}$$

$$m = [-\frac{(n_2^*)^{-2} - (n_1^*)^{-2}}{2} (\frac{(n_2^*)^{-2} + (n_1^*)^{-2}}{2})^{-3/2} - (n_2^* - n_1^*)] \tag{B.4}$$

where [] denotes the nearest integer and $n_i^* = n_i - \delta_{l_i}$ is the effective principal quantum number of the $i = 1, 2$ state (δ_{l_i} is the quantum defect).

$$\nu_c = (\frac{s}{-((n_2^*)^{-2} - (n_1^*)^{-2})/2})^{1/3} \tag{B.5}$$

$$s = m + n_2^* - n_1^* \tag{B.6}$$

$$\eta = \frac{l_1 + l_2 + 1}{2\nu_c} \tag{B.7}$$

$$e_c = \sqrt{1 - \eta^2} \tag{B.8}$$

$$D_r(e_c, s) = D_p(e_c, s) + \frac{1 - e_c}{\pi s} sin(\pi s) \tag{B.9}$$

$$D_p(e_c, s) = (-J_s'(-e_c s) + \frac{(l_2 - l_1)\eta}{\nu_c} (J_s(-e_c s) - \frac{sin(\pi s)}{\pi s}))/s \tag{B.10}$$

where J and J' denote the Bessel function and its derivative.

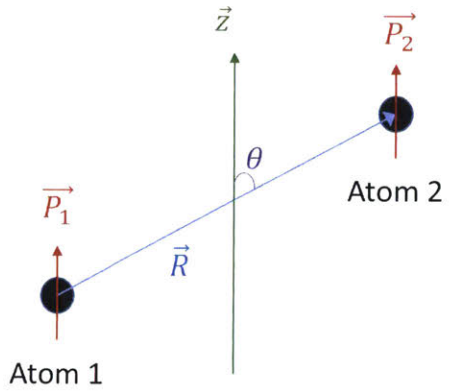

Figure B-1: **Illustration of two interacting Rydberg atoms.** $\vec{P}_1$ and $\vec{P}_2$ denote the individual electric dipole moments that are aligned with the quantization axis $\vec{z}$. R is the internulcear separation of the two atoms and it has a angle θ relative to the quantization axis.

The Hamiltonian H is diagonalized and the eigenvector that has the maximum overlap with the double-atom state we are interested in is plotted.

Appendix C

Data analysis for the conditional three-photon phase

The correlation functions and the conditional phases are calculated with a MATLAB program. The two analyses have a lot in common. Although I will focus on the conditional phase analysis, information of both analyses will be presented to help people who are interested in doing similar analysis or further developing the MATLAB program.

The raw data contains a list of photons. Each is tagged with the cycle number, the gate number, the detector number and the time of arrival relative to the beginning of the gate. "Cycle" refers to the experimental cycle that starts with loading the MOT and finishes with the EIT experiment. Within each cycle, the SPCM can be turned on and off many times, and each time is considered a "gate". Whenever, they are turned on, a TTL pulse is generated (the same as the ones caused by real photons) and its arrival time at the counter is considered as "time" zero for that "gate". The counter has four channels, and each SPCM is connected to its own channel. The channel ("detector") number is also registered for each photon.

First, I check the total photons per cycle as a function of the cycle number and remove erroneous data if necessary. Monitoring this in real time also helps us identify problems while taking data. For example, if the repumper laser gets unlocked at some point, there will be very few atoms and a lot more photons will be detected. In

that case, we will see a sudden increase in the total photons per cycle. We can then remove all the data after the jump, relock the laser and continue the measurement.

After the post-selection, the selected data are used to plot the pulse shape–photon number as a function of time relative to the beginning of the gates. This is where we extract the count rates and total counts within a given time window (for each channel). For the conditional phase measurements, channel 3 has both the probe and LO, while channel 1&2 only have the probe.

Next, I find the phase drift information from channel 3 data. The data is divided by $\sim 10ms$ segments. For example, if a measurement contains a total of 2 cycles, and each cycle has a total measurement duration 120ms (time elapse between the first and last probe pulses in the cycle including the time when the dipole trap is on and probe is off), then there are in total $\frac{120\times 2}{10} = 24$ segments for this data set. The duration of segments is adjusted for each data set to optimize the visibility. Within each segment, all photons from channel 3 are collected to draw a histogram as a function of the remainder of "time" divided by the oscillation period. The histogram is fitted with the function: $A + B\cos(2\pi f_0 t + \phi_0)$, where f_0 is the nominal oscillation frequency 79MHz and B is restricted to be positive. Some examples of ϕ_0 fitting are shown in Fig. C-1. The After wrapped into [$-\pi$,π], a list of ϕ_0 tagged with the cycle number and segment is saved.

With this list, I go through all the photons from channel 3 again. This time, each "time" is corrected by $\phi_0/(2\pi f_0)$ with ϕ_0 from the same segment. With this correction, photons from different segments can be plotted in the same histogram, because the drift is already taken care of. Now, we can group data by "time" with a bin size, say $0.25\mu s$. Within each bin, we can draw a histogram and fit and phase ϕ_0'. If the oscillation frequency is exact, then ϕ_0' is expected to be constantly zero. On the other hand, if the true oscillation frequency f is not exactly the nominal frequency f_0, then ϕ_0' will be linear with time and f can be extracted from the slope (Fig. C-2). Once f is determined, I use the new f to determine the phase drift and generate the new ϕ_0 list.

Then I generate the list of photon "pairs" for the conditional two-photon phase.

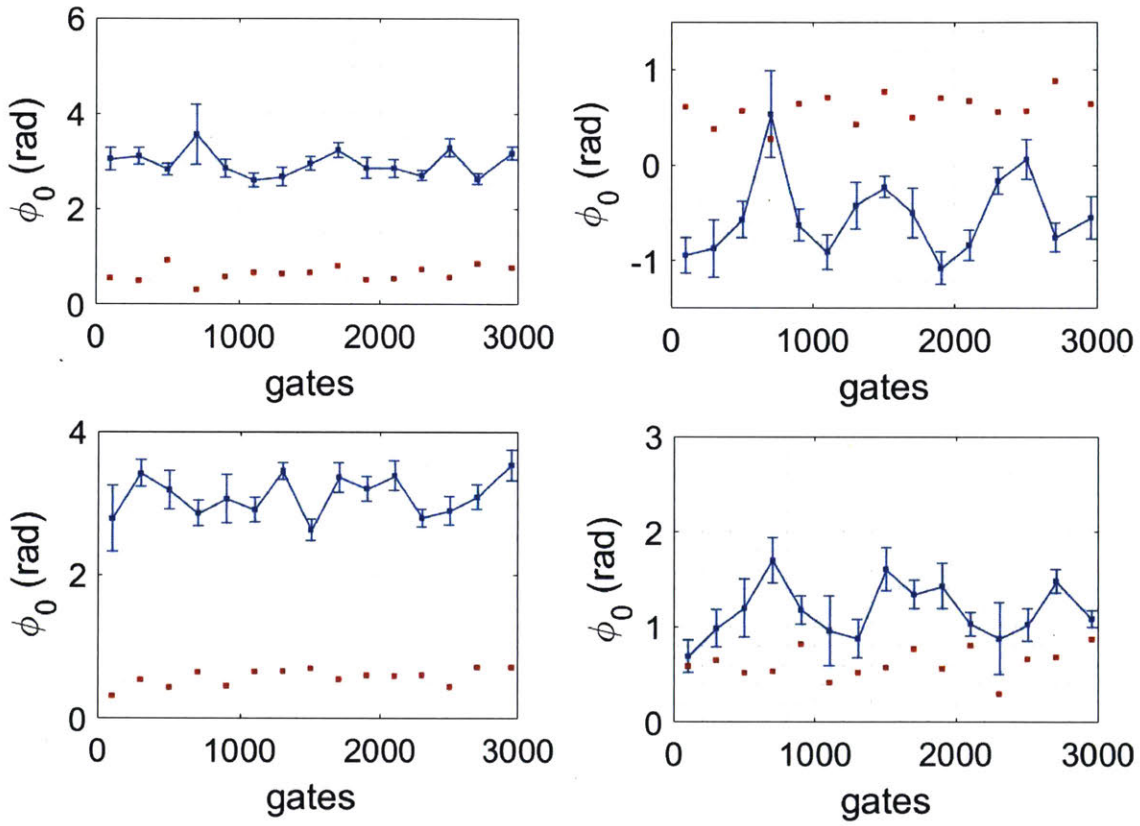

Figure C-1: **Examples of ϕ_0 fitting from cycle 1, 501, 1001 and 1501 in one data set (ϕ_0 in blue and visibility in red).**

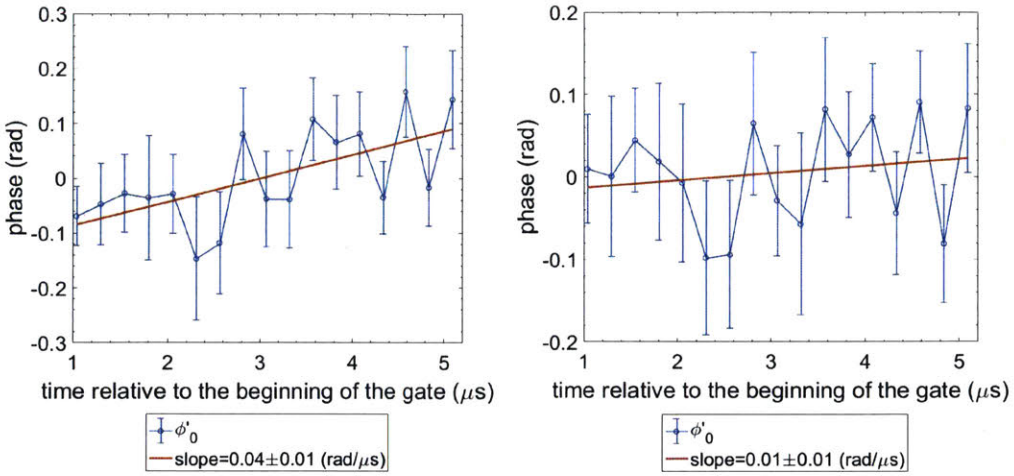

Figure C-2: **Examples of ϕ_0' fitting** (**Left**: with oscillation frequency 79MHz. **Right**: with oscillation frequency 79.012MHz). The blue data are the fitted ϕ_0' from the histograms and the red line is a linear fit. For this data set, the oscillation frequency is determined to be 79.012MHz by minimizing the slope. The fitted oscillation frequency is not the same for different data sets. All of them are larger than the nominal 79MHz and are different on the order of 10^{-3}MHz.

Within the same gate, a channel 3 photon can be paired with either channel 1 or channel 2 probe photons. In addition to the phase detection time (channel 3) and probe detection time (channel 1 or 2), each pair is also tagged with phase drift correction (interpolation of ϕ_0). An example of the interpolation is shown in Fig. C-3. I keep both the raw "time" and the phase correction because the relative time between photons are calculated with the raw time.

```
%% conditioned phase of 2 photons
time_diff=abs(pairs(:,1)-pairs(:,2));%relative time between
    the phase and probe detection
phi0=pairs(:,3);%phase correction
raw_time=pairs(:,2);%phase detection time
for ipair=1:length(time_diff)
    if time_diff(ipair)<g2_tau_axis(end)
        tau=ceil(time_diff(ipair)/g2_bin);%determine which
            bin this pair goes to
```

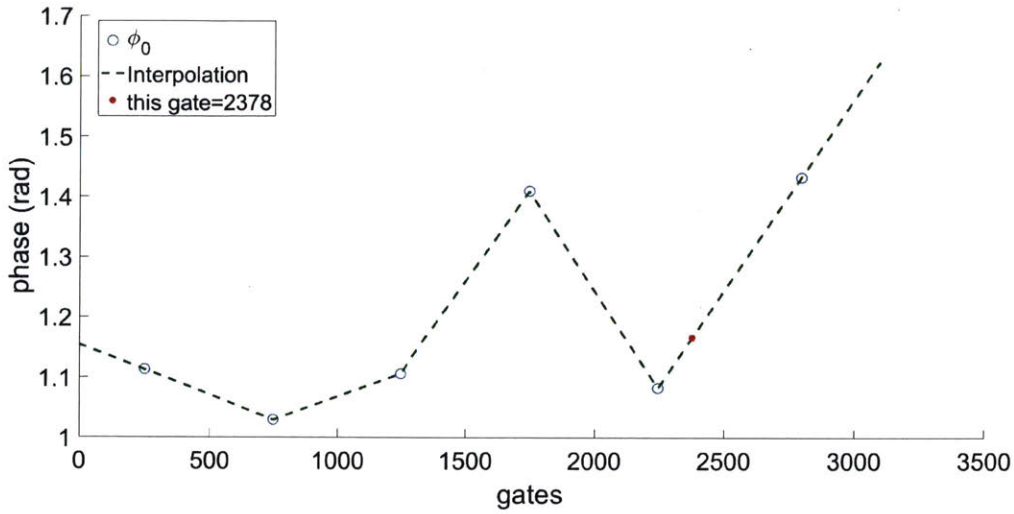

Figure C-3: **An example of the interpolation of ϕ_0.** For photon pairs in gate 2378 in this particular cycle, the phase correction is 1.166 rad.

```
8           if tau==0;tau=1;end
9           cond_photon_est{tau}(iph(tau))=mod(raw_time(ipair)+
                phi0(ipair)/(2*pi*osc_freq),osc_period);%calculate
                 the remainder with the phase correction for the
                histogram
10          iph(tau)=iph(tau)+1;
11      end
12  end
```

I loop through all the photon pairs. If the relative time falls within a certain bin tau, then that pair contributes to the cell array element cond_photon_est{tau}. Afterwards, for each bin, a histogram is created and a phase is fitted. That phase is labeled as $\phi^{(2)}(t_1, t_2) - \phi^{(1)}(t_1)$, where t_1 and t_2 are the probe and phase measurement time, respectively. Or if we drop the dependence of the absolute time, the phase is $\phi^{(2)}(\tau) - \phi^{(1)}$. The phase is referenced to its own average value when τ is large $\phi^{(2)}_{ref} \equiv \phi^{(2)}(\tau \to \infty) - \phi^{(1)} = (\phi^{(1)} + \phi^{(1)}) - \phi^{(1)} = \phi^{(1)}$. The second last step uses the fact that when the two photons are very far apart, they cannot be correlated and hence the two-photon phase cannot be anything other than the sum of the single-photon phase. The final result from the two-photon conditional phase analysis is

then $\phi^{(2)}(\tau) - \phi^{(1)} - \phi^{(2)}_{ref} = \phi^{(2)}(\tau) - 2\phi^{(1)}$. Physically, it tells us what the additional phase the photon pair acquires compared with two uncorrelated photons.

The three-photon conditional phase is determined similarly. Each photon triplet is tagged with two probe detection times, one phase measurement time and a phase drift correction. For each data set, two different triplet lists are generated–one with the two probe photons from two different detectors and the other with two probe photons regardless of which detector they come from. The first list is used to generate 2D three-photon phase plots, while the second list is for 1D plots after I confirm the result is statistically the same as from the first list, especially when all three photons are close by.

For each bin, the phase fitted from the histogram is labeled as $\phi^{(3)}(t_1, t_2, t_3) - \phi^{(2)}(t_1, t_2)$, where t_1 and t_2 are probe detection times, and t_3 is the phase measurement time. This phase is referenced to three uncorrelated photons–subtract the average value when all three photons are far from each other. $\phi^{(3)}(t_1, t_2, t_3) - \phi^{(2)}(t_1, t_2) - \phi^{(3)}_{ref} = \phi^{(3)}(t_1, t_2, t_3) - \phi^{(2)}(t_1, t_2) - ((\phi^{(1)}(t_1) + \phi^{(1)}(t_2) + \phi^{(1)}(t_3)) - (\phi^{(1)}(t_1) + \phi^{(1)}(t_2))) = \phi^{(3)}(t_1, t_2, t_3) - \phi^{(2)}(t_1, t_2) - \phi^{(1)}(t_3)$. I did not explicitly drop the absolute time dependence, because there are multiple ways to define the relative times and it could be confusing. However, none of the phases should depend on the absolute time. In most occasions, we are interested in the three-photon phase relative to three uncorrelated photons. Therefore, we would like to remove $\phi^{(2)}$ from the directly measured three-photon phase. The way to do this is to take the processed $\phi^{(2)}(\tau) - 2\phi^{(1)}$ from the same data set and add it to the three-photon phase $\phi^{(3)}(t_1, t_2, t_3) - \phi^{(2)}(t_1, t_2) - \phi^{(1)}(t_3) + (\phi^{(2)}(\tau) - 2\phi^{(1)}) = \phi^{(3)}(t_1, t_2, t_3) - (\phi^{(1)}(t_1) + \phi^{(1)}(t_2) + \phi^{(1)}(t_3))$, for $|t_1 - t_2| = \tau$ within the bin size. Again, the dependence on the absolute time is put back for consistency in the notations. The phases only depend on the relative times.

One last comment on the pairs and triplets is that all possible combinations are included. For example, if within a gate, probe is detected at t_1 and t_2, and the phase measurements happen at t_3 and t_3'. Then the pairs are $\{t_1, t_3\}$, $\{t_2, t_3\}$, $\{t_1, t_3'\}$ and $\{t_2, t_3'\}$. The triplets are $\{t_1, t_2, t_3\}$ and $\{t_1, t_2, t_3'\}$. With low detection efficiency, excluding photons will not be able to remove the "contamination" from higher photon

number events.

The correlation functions are calculated from similar lists without the hassle of dealing with phase corrections. $g^{(2)}(t_1, t_2) = \frac{\langle n_i(t_1)\rangle\langle n_j(t_2)\rangle}{\langle n_i(t_1)n_j(t_2)\rangle}$, where $i \neq j$ are all possible combinations of the detectors. Three $g^{(2)}$ curves are obtained with three detectors. There is no observable difference between the three since we carefully optimize the fiber coupling to the detectors before each measurement. $g^{(3)}(t_1, t_2, t_3) = \frac{\langle n_1(t_1)\rangle\langle n_2(t_2)\rangle\langle n_3(t_3)\rangle}{\langle n_1(t_1)n_2(t_2)n_3(t_3)\rangle}$, where 1,2,3 refers to the three detectors.

Bibliography

[1] Agrawal, G. & Liao, P. F. *Nonlinear Fiber Optics: Formerly Quantum Electronics.* Optics and Photonics (Elsevier Science, 2013).

[2] Kimble, H. J. The quantum internet. *Nature* **453**, 1023 (2008).

[3] Reiserer, A. & Rempe, G. Cavity-based quantum networks with single atoms and optical photons. *Rev. Mod. Phys.* **87**, 1379 (2015).

[4] Giovannetti, V., Lloyd, S. & Maccone, L. Advances in quantum metrology. *Nature photonics* **5**, 222 (2011).

[5] Tey, M. K. *et al.* Strong interaction between light and a single trapped atom without the need for a cavity. *Nat Phys* **4**, 924 (2008).

[6] Darquié, B. *et al.* Controlled single-photon emission from a single trapped two-level atom. *Science* **309**, 454 (2005).

[7] Tiecke, T. *et al.* Nanophotonic quantum phase switch with a single atom. *Nature* **508**, 241 (2014).

[8] Volz, J., Scheucher, M., Junge, C. & Rauschenbeutel, A. Nonlinear π phase shift for single fibre-guided photons interacting with a single resonator-enhanced atom. *Nature Photonics* **8**, 965 (2014).

[9] Shomroni, I. *et al.* All-optical routing of single photons by a one-atom switch controlled by a single photon. *Science* **345**, 903 (2014).

[10] Hamsen, C., Tolazzi, K. N., Wilk, T. & Rempe, G. Two-photon blockade in an atom-driven cavity qed system. *Phys. Rev. Lett.* **118**, 133604 (2017).

[11] Angelakis, D. G., Santos, M. F. & Bose, S. Photon-blockade-induced mott transitions and x y spin models in coupled cavity arrays. *Physical Review A* **76**, 031805 (2007).

[12] Cho, J., Angelakis, D. G. & Bose, S. Fractional quantum hall state in coupled cavities. *Physical review letters* **101**, 246809 (2008).

[13] Shapiro, J. H. Single-photon kerr nonlinearities do not help quantum computation. *Physical Review A* **73**, 062305 (2006).

[14] Chen, W. *et al.* All-optical switch and transistor gated by one stored photon. *Science* **341**, 768 (2013).

[15] Beck, K. M., Hosseini, M., Duan, Y. & Vuletić, V. Large conditional single-photon cross-phase modulation. *Proceedings of the National Academy of Sciences* 201524117 (2016).

[16] Dudin, Y. O. & Kuzmich, A. Strongly interacting rydberg excitations of a cold atomic gas. *Science* **336**, 887 (2012).

[17] Maxwell, D. *et al.* Storage and control of optical photons using rydberg polaritons. *Phys. Rev. Lett.* **110**, 103001 (2013).

[18] Peyronel, T. *et al.* Quantum nonlinear optics with single photons enabled by strongly interacting atoms. *Nature* **488**, 57 (2012).

[19] Firstenberg, O. *et al.* Attractive photons in a quantum nonlinear medium. *Nature* **502**, 71 (2013).

[20] Tiarks, D., Baur, S., Schneider, K., Dürr, S. & Rempe, G. Single-photon transistor using a förster resonance. *Physical review letters* **113**, 053602 (2014).

[21] Gorniaczyk, H., Tresp, C., Schmidt, J., Fedder, H. & Hofferberth, S. Single-photon transistor mediated by interstate rydberg interactions. *Phys. Rev. Lett.* **113**, 053601 (2014).

[22] Gorniaczyk, H. *et al.* Enhancement of Rydberg-mediated single-photon nonlinearities by electrically tuned Förster resonances. *Nature Communications* **7**, 12480 (2016).

[23] Thompson, J. D. *et al.* Symmetry-protected collisions between strongly interacting photons. *Nature* **542**, 206 (2017).

[24] Lai, Y. & Haus, H. A. Quantum theory of solitons in optical fibers. i. time-dependent hartree approximation. *Phys. Rev. A* **40**, 844–853 (1989).

[25] Lai, Y. & Haus, H. Quantum theory of solitons in optical fibers. ii. exact solution. *Physical Review A* **40**, 854 (1989).

[26] Drummond, P. D., Shelby, R. M., Friberg, S. R. & Yamamoto, Y. Quantum solitons in optical fibres. *Nature* **365**, 307 (1993).

[27] Hwang, J. *et al.* A single-molecule optical transistor. *Nature* **460**, 76 (2009).

[28] Sipahigil, A. *et al.* An integrated diamond nanophotonics platform for quantum-optical networks. *Science* **354**, 847 (2016).

[29] Fushman, I. *et al.* Controlled phase shifts with a single quantum dot. *science* **320**, 769 (2008).

[30] Devoret, M. H. & Schoelkopf, R. J. Superconducting circuits for quantum information: an outlook. *Science* **339**, 1169 (2013).

[31] Loudon, R. *The Quantum Theory of Light* (OUP Oxford, 2000).

[32] Brown, R. H., Twiss, R. Q. *et al.* Correlation between photons in two coherent beams of light. *Nature* **177**, 27 (1956).

[33] Brown, R. H. & Twiss, R. A test of a new type of stellar interferometer on sirius. *Nature* **178**, 1046 (1956).

[34] Saffman, M., Walker, T. G. & Mølmer, K. Quantum information with rydberg atoms. *Reviews of Modern Physics* **82**, 2313 (2010).

[35] Firstenberg, O., Adams, C. S. & Hofferberth, S. Nonlinear quantum optics mediated by rydberg interactions. *Journal of Physics B: Atomic, Molecular and Optical Physics* **49**, 152003 (2016).

[36] Beterov, I., Ryabtsev, I., Tretyakov, D. & Entin, V. Quasiclassical calculations of blackbody-radiation-induced depopulation rates and effective lifetimes of rydberg n s, n p, and n d alkali-metal atoms with n 80. *Physical Review A* **79**, 052504 (2009).

[37] Farley, J. W. & Wing, W. H. Accurate calculation of dynamic stark shifts and depopulation rates of rydberg energy levels induced by blackbody radiation. hydrogen, helium, and alkali-metal atoms. *Physical Review A* **23**, 2397 (1981).

[38] Goldschmidt, E. A. *et al.* Anomalous broadening in driven dissipative rydberg systems. *Phys. Rev. Lett.* **116**, 113001 (2016).

[39] Greene, C. H., Dickinson, A. & Sadeghpour, H. Creation of polar and nonpolar ultra-long-range rydberg molecules. *Physical Review Letters* **85**, 2458 (2000).

[40] Bendkowsky, V. *et al.* Observation of ultralong-range rydberg molecules. *Nature* **458**, 1005 (2009).

[41] Booth, D., Rittenhouse, S., Yang, J., Sadeghpour, H. & Shaffer, J. Production of trilobite rydberg molecule dimers with kilo-debye permanent electric dipole moments. *Science* **348**, 99 (2015).

[42] Niederprüm, T. *et al.* Observation of pendular butterfly rydberg molecules. *Nature communications* **7**, 12820 (2016).

[43] Gaj, A. *et al.* From molecular spectra to a density shift in dense rydberg gases. *Nature communications* **5**, 4546 (2014).

[44] Baur, S., Tiarks, D., Rempe, G. & Dürr, S. Single-photon switch based on rydberg blockade. *Phys. Rev. Lett.* **112**, 073901 (2014).

[45] Niederprüm, T., Thomas, O., Manthey, T., Weber, T. M. & Ott, H. Giant cross section for molecular ion formation in ultracold rydberg gases. *Phys. Rev. Lett.* **115**, 013003 (2015).

[46] Ravets, S. *et al.* Coherent dipole-dipole coupling between two single Rydberg atoms at an electrically-tuned Forster resonance. *Nat Phys* **10**, 914 (2014).

[47] Bohlouli-Zanjani, P., Petrus, J. A. & Martin, J. D. D. Enhancement of rydberg atom interactions using ac stark shifts. *Phys. Rev. Lett.* **98**, 203005 (2007).

[48] Fleischhauer, M., Imamoglu, A. & Marangos, J. P. Electromagnetically induced transparency: Optics in coherent media. *Reviews of modern physics* **77**, 633 (2005).

[49] Zimmer, F. E., Otterbach, J., Unanyan, R. G., Shore, B. W. & Fleischhauer, M. Dark-state polaritons for multicomponent and stationary light fields. *Phys. Rev. A* **77**, 063823 (2008).

[50] Otterbach, J., Moos, M., Muth, D. & Fleischhauer, M. Wigner crystallization of single photons in cold rydberg ensembles. *Physical review letters* **111**, 113001 (2013).

[51] Hau, L. V., Harris, S. E., Dutton, Z. & Behroozi, C. H. Light speed reduction to 17 metres per second in an ultracold atomic gas. *Nature* **397**, 594 (1999).

[52] Wang, L. J., Kuzmich, A. & Dogariu, A. Gain-assisted superluminal light propagation. *Nature* **406**, 277 (2000).

[53] Lukin, M. D. *et al.* Dipole blockade and quantum information processing in mesoscopic atomic ensembles. *Phys. Rev. Lett.* **87**, 037901 (2001).

[54] Tong, D. *et al.* Local blockade of rydberg excitation in an ultracold gas. *Phys. Rev. Lett.* **93**, 063001 (2004).

[55] Singer, K., Reetz-Lamour, M., Amthor, T., Marcassa, L. G. & Weidemüller, M. Suppression of excitation and spectral broadening induced by interactions in a cold gas of rydberg atoms. *Phys. Rev. Lett.* **93**, 163001 (2004).

[56] Liebisch, T. C., Reinhard, A., Berman, P. & Raithel, G. Atom counting statistics in ensembles of interacting rydberg atoms. *Physical review letters* **95**, 253002 (2005).

[57] Friedler, I., Petrosyan, D., Fleischhauer, M. & Kurizki, G. Long-range interactions and entanglement of slow single-photon pulses. *Phys. Rev. A* **72**, 043803 (2005).

[58] Pritchard, J. D. *et al.* Cooperative atom-light interaction in a blockaded rydberg ensemble. *Phys. Rev. Lett.* **105**, 193603 (2010).

[59] Rempe, G., Lalezari, R., Thompson, R. & Kimble, H. Measurement of ultralow losses in an optical interferometer. *Optics letters* **17**, 363 (1992).

[60] Mazurenko, A. *Optical imaging of Rydberg atoms.* Bachelor's thesis, Massachusetts Institute of Technology (2012).

[61] Black, E. D. An introduction to pound–drever–hall laser frequency stabilization. *American Journal of Physics* **69**, 79 (2001).

[62] Dalibard, J. & Cohen-Tannoudji, C. Laser cooling below the doppler limit by polarization gradients: simple theoretical models. *J. Opt. Soc. Am. B* **6**, 2023 (1989).

[63] Peyronel, T. T. M. M. *Quantum nonlinear optics using cold atomic ensembles.* Ph.D. thesis, Massachusetts Institute of Technology (2013).

[64] Kerman, A. J. *Raman sideband cooling and cold atomic collisions in optical lattices.* Ph.D. thesis, stanford university (2002).

[65] Kerman, A. J., Vuletić, V., Chin, C. & Chu, S. Beyond optical molasses: 3d raman sideband cooling of atomic cesium to high phase-space density. *Physical review letters* **84**, 439 (2000).

[66] Michler, P. *et al.* A quantum dot single-photon turnstile device. *Science* **290**, 2282 (2000).

[67] Dousse, A. *et al.* Ultrabright source of entangled photon pairs. *Nature* **466**, 217 (2010).

[68] Högele, A., Galland, C., Winger, M. & Imamoğlu, A. Photon antibunching in the photoluminescence spectra of a single carbon nanotube. *Phys. Rev. Lett.* **100**, 217401 (2008).

[69] Bozyigit, D. *et al.* Antibunching of microwave-frequency photons observed in correlation measurements using linear detectors. *Nature Physics* **7**, 154 (2011).

[70] Kurtsiefer, C., Mayer, S., Zarda, P. & Weinfurter, H. Stable solid-state source of single photons. *Phys. Rev. Lett.* **85**, 290 (2000).

[71] Diedrich, F. & Walther, H. Nonclassical radiation of a single stored ion. *Phys. Rev. Lett.* **58**, 203 (1987).

[72] Zeuthen, E., Gullans, M. J., Maghrebi, M. F. & Gorshkov, A. V. Correlated photon dynamics in dissipative rydberg media. *arXiv preprint arXiv:1608.06068* (2016).

[73] Derevianko, A., Kómár, P., Topcu, T., Kroeze, R. M. & Lukin, M. D. Effects of molecular resonances on rydberg blockade. *Phys. Rev. A* **92**, 063419 (2015).

[74] Adamson, R. B. A., Shalm, L. K., Mitchell, M. W. & Steinberg, A. M. Multiparticle state tomography: Hidden differences. *Phys. Rev. Lett.* **98**, 043601 (2007).

[75] James, D. F., Kwiat, P. G., Munro, W. J. & White, A. G. Measurement of qubits. *Physical Review A* **64**, 052312 (2001).

[76] Tiarks, D., Schmidt, S., Rempe, G. & Dürr, S. Optical π phase shift created with a single-photon pulse. *Science Advances* **2** (2016).

[77] Bienias, P. & Büchler, H. P. Quantum theory of kerr nonlinearity with rydberg slow light polaritons. *New Journal of Physics* **18**, 123026 (2016).

[78] Bienias, P. *et al.* Scattering resonances and bound states for strongly interacting rydberg polaritons. *Physical Review A* **90**, 053804 (2014).

[79] Gorshkov, A. V., Otterbach, J., Fleischhauer, M., Pohl, T. & Lukin, M. D. Photon-photon interactions via rydberg blockade. *Phys. Rev. Lett.* **107**, 133602 (2011).

[80] Deutsch, I. H., Chiao, R. Y. & Garrison, J. C. Diphotons in a nonlinear fabry-pérot resonator: Bound states of interacting photons in an optical "quantum wire". *Phys. Rev. Lett.* **69**, 3627 (1992).

[81] Shen, J.-T. & Fan, S. Strongly correlated two-photon transport in a one-dimensional waveguide coupled to a two-level system. *Physical review letters* **98**, 153003 (2007).

[82] Drummond, P. & He, H. Optical mesons. *Physical Review A* **56**, R1107 (1997).

[83] Cheng, Z. & Kurizki, G. Optical "multiexcitons": Quantum gap solitons in nonlinear bragg reflectors. *Phys. Rev. Lett.* **75**, 3430 (1995).

[84] Deutsch, I. H., Chiao, R. Y. & Garrison, J. C. Two-photon bound states: The diphoton bullet in dispersive self-focusing media. *Phys. Rev. A* **47**, 3330 (1993).

[85] Chang, D. *et al.* Crystallization of strongly interacting photons in a nonlinear optical fibre. *Nature Physics* **4**, 884 (2008).

[86] Maghrebi, M. F. *et al.* Fractional quantum hall states of rydberg polaritons. *Phys. Rev. A* **91**, 033838 (2015).

[87] Lai, Y. & Lee, R.-K. Entangled quantum nonlinear schrödinger solitons. *Phys. Rev. Lett.* **103**, 013902 (2009).

[88] Beth, T. & Leuchs, G. *Quantum Information Processing* (Wiley, 2006).

[89] Rundquist, A. *et al.* Nonclassical higher-order photon correlations with a quantum dot strongly coupled to a photonic-crystal nanocavity. *Physical Review A* **90**, 023846 (2014).

[90] Stevens, M. J., Glancy, S., Nam, S. W. & Mirin, R. P. Third-order antibunching from an imperfect single-photon source. *Optics express* **22**, 3244 (2014).

[91] Aßmann, M., Veit, F., Bayer, M., van der Poel, M. & Hvam, J. M. Higher-order photon bunching in a semiconductor microcavity. *Science* **325**, 297 (2009).

[92] Stevens, M. J. *et al.* High-order temporal coherences of chaotic and laser light. *Optics express* **18**, 1430 (2010).

[93] Zhou, Y., Simon, J., Liu, J. & Shih, Y. Third-order correlation function and ghost imaging of chaotic thermal light in the photon counting regime. *Phys. Rev. A* **81**, 043831 (2010).

[94] Ma, L. *et al.* Temporal correlation of photons following frequency up-conversion. *Optics express* **19**, 10501 (2011).

[95] Wiersig, J. *et al.* Direct observation of correlations between individual photon emission events of a microcavity laser. *Nature* **460**, 245 (2009).

[96] Resch, K. J., Walther, P. & Zeilinger, A. Full characterization of a three-photon greenberger-horne-zeilinger state using quantum state tomography. *Physical review letters* **94**, 070402 (2005).

[97] Shalm, L., Adamson, R. & Steinberg, A. Squeezing and over-squeezing of triphotons. *Nature* **457**, 67 (2009).

[98] Tashima, T. *et al.* Local transformation of two einstein-podolsky-rosen photon pairs into a three-photon w state. *Physical review letters* **102**, 130502 (2009).

[99] Agne, S. *et al.* Observation of genuine three-photon interference. *Phys. Rev. Lett.* **118**, 153602 (2017).

[100] Menssen, A. J. *et al.* Distinguishability and many-particle interference. *Phys. Rev. Lett.* **118**, 153603 (2017).

[101] Gullans, M. J. *et al.* Effective field theory for rydberg polaritons. *Phys. Rev. Lett.* **117**, 113601 (2016).

[102] Lompe, T. *et al.* Radio-frequency association of efimov trimers. *Science* **330**, 940 (2010).

[103] Nakajima, S., Horikoshi, M., Mukaiyama, T., Naidon, P. & Ueda, M. Measurement of an efimov trimer binding energy in a three-component mixture of ^{6}Li. *Phys. Rev. Lett.* **106**, 143201 (2011).

[104] Jachymski, K., Bienias, P. & Büchler, H. P. Three-body interaction of rydberg slow-light polaritons. *Physical Review Letters* **117**, 053601 (2016).

[105] Bienias, P. *et al.* Scattering resonances and bound states for strongly interacting Rydberg polaritons. *Phys. Rev. A* **90**, 53804 (2014).

[106] Gaunt, A. L., Schmidutz, T. F., Gotlibovych, I., Smith, R. P. & Hadzibabic, Z. Bose-einstein condensation of atoms in a uniform potential. *Phys. Rev. Lett.* **110**, 200406 (2013).

[107] Mukherjee, B. *et al.* Homogeneous atomic fermi gases. *Phys. Rev. Lett.* **118**, 123401 (2017).

[108] Maghrebi, M. F. *et al.* Fractional quantum hall states of rydberg polaritons. *Physical Review A* **91**, 033838 (2015).

[109] Sommer, A., Büchler, H. P. & Simon, J. Quantum crystals and laughlin droplets of cavity rydberg polaritons. *arXiv preprint arXiv:1506.00341* (2015).

[110] Nielsen, M. A. & Chuang, I. L. *Quantum Computation and Quantum Information.* Cambridge Series on Information and the Natural Sciences (Cambridge University Press, 2000).

[111] Monroe, C. *et al.* Large-scale modular quantum-computer architecture with atomic memory and photonic interconnects. *Phys. Rev. A* **89**, 022317 (2014).

[112] Monroe, C. & Kim, J. Scaling the ion trap quantum processor. *Science* **339**, 1164–1169 (2013).

[113] Sun, H.-H. *et al.* Majorana zero mode detected with spin selective andreev reflection in the vortex of a topological superconductor. *Phys. Rev. Lett.* **116**, 257003 (2016).

[114] Nadj-Perge, S. *et al.* Observation of majorana fermions in ferromagnetic atomic chains on a superconductor. *Science* **346**, 602 (2014).

[115] Chang, D. E., Vuletić, V. & Lukin, M. D. Quantum nonlinear optics [mdash] photon by photon. *Nature Photonics* **8**, 685 (2014).

[116] Weber, S. *et al.* Tutorial: Calculation of rydberg interaction potentials. *arXiv preprint arXiv:1612.08053* (2016).

[117] Reinhard, A., Liebisch, T. C., Knuffman, B. & Raithel, G. Level shifts of rubidium rydberg states due to binary interactions. *Phys. Rev. A* **75**, 032712 (2007).

[118] Kaulakys, B. Consistent analytical approach for the quasi-classical radial dipole matrix elements. *Journal of Physics B: Atomic, Molecular and Optical Physics* **28**, 4963 (1995).

[119] Kamta, G. L., Engo, S. N., Njock, M. K. & Oumarou, B. Consistent description of klein-gordon dipole matrix elements. *Journal of Physics B: Atomic, Molecular and Optical Physics* **31**, 963 (1998).